Preparation and Photocatalytic Activity of Ag/ZnO Powders

Khanitta Intarasuwan

A Thesis Submitted in Partial Fulfillment of the Requirements for the Degree of

Master of Science in Chemistry

Prince of Songkla University

2013

Thesis Title Preparation and photocatalytic activity of Ag/ ZnO powders
Author Miss Khanitta Intarasuwan
Major Program Chemistry

Major Advisor

…….…….....
(Asst.Prof.Dr.Pongsaton Amornpitoksuk)

Co-advisor

…….....
(Asst.Prof.Dr.Sumetha Suwanboon)

Examining Committee

….……..…Chairperson
(Dr.Tanakorn Ratana)

…….…….....
(Asst.Prof.Dr.Pongsaton Amornpitoksuk)

…….....
(Asst.Prof.Dr.Sumetha Suwanboon)

…….....
(Dr.Uraiwan Sirimahachai)

The Graduate School, Prince of Songkla University, has approved this thesis as partial fulfillment of the requirements for the Master of Science Degree in Chemical Studies.

…….....
(Assoc. Prof. Dr. Teerapol Srichana)
Dean of Graduate School

This is to certify that the work here submitted is the result of the candidate's own investigations. Due acknowledgement has been made of any assistance received.

…….Signature

(Asst. Prof. Dr. Pongsaton Amornpitoksuk)

Major Advisor

…….Signature

(Khanitta Intarasuwan)

Candidate

I hereby certify that this work has not been accepted in substance for any degree, and is not being currently submitted in candidature for any degree.

…… Signature

(Khanitta Intarasuwan)

Candidate

.

ชื่อวิทยานิพนธ์ การเตรียมและสมบัติการเร่งปฏิกิริยาเชิงแสงของผงAg/ZnO
ผู้เขียน นางสาว ขนิษฐา อินทรสุวรรณ์
สาขาวิชา เคมี
ปีการศึกษา 2555

บทคัดย่อ

งานวิจัยนี้ศึกษาผลการเพิ่มประสิทธิภาพการเร่งเชิงแสงของผงซิงค์ออกไซด์โดยการเปลี่ยนแปลงสัณฐานและการเติมโลหะเงิน การเปลี่ยนแปลงสัณฐานของซิงค์ออกไซด์ทำโดยการเปลี่ยนแปลงอัตราเร็วในการผสมสารละลายซิงค์ไอออนกับไฮดรอกไซด์ไอออน เมื่อซิงค์ไอออนทำปฏิกิริยากับไฮดรอกไซด์ไอออนเกิดเป็นซิงค์ไฮดรอกไซด์ซึ่งเป็นตะกอนปฐมภูมิ หลังจากนั้นซิงค์ไฮดรอกไซด์เปลี่ยนเป็นซิงค์ออกไซด์ในสารละลายเบสที่ร้อน ขนาดของซิงค์ออกไซด์รูปคล้ายหอยแม่นมีขนาดลดลงเมื่ออัตราเร็วในการผสมสารตั้งต้นลดลง ซิงค์ออกไซด์ที่มีรูปร่างคล้ายหอยแม่นขนาดใหญ่มีหน้าหกเหลี่ยมในระนาบ (0001) มากทำให้มีความสามารถในการสลายสีย้อมเมทิลีนบูลดีที่สุด

ปริมาณเงินและลำดับของการเติมไอออนเงินเป็นตัวแปรอีกชนิดหนึ่งที่ศึกษาในงานวิจัยนี้ โดยวิธีที่ 1 เป็นการผสมซิงค์ไอออนและไอออนเงินเข้าด้วยกันก่อนการเติมไฮดรอกไซด์ไอออน ในขณะที่วิธีที่ 2 เป็นการเติมไอออนเงินลงในสารแขวนลอยที่เกิดจากการทำปฏิกิริยาของซิงค์ไอออนกับไฮดรอกไซด์ไอออน เมื่อปริมาณเงินน้อยกว่า 9 เปอร์เซ็นต์โดยโมล Ag/ZnO ที่เตรียมจากวิธีที่ 2 ให้ประสิทธิภาพที่ดีกว่า Ag/ZnO ที่เติมจากวิธีที่ 1 แต่เมื่อปริมาณเงินมากกว่าหรือเท่ากับ 9 เปอร์เซ็นต์โดยโมล Ag/ZnO ที่เตรียมด้วยวิธีที่ 2 แสดงประสิทธิภาพที่ดีกว่า Ag/ZnO ที่เตรียมด้วยวิธีที่ 1 จากผลการทดลองพบว่าซิงค์ออกไซด์ที่เติมเงิน 9 เปอร์เซ็นต์โดยโมลที่เตรียมจากวิธีที่ 1 ให้ประสิทธิภาพดีที่สุด นอกจากนี้แล้วตัวเร่งเชิงแสงดังกล่าวสามารถสลายสีย้อมเมทิลีนบูล โรดามีนบี และรีเอ็กทีฟออร์เรน 16 โดยให้ประสิทธิภาพในการสลายสีย้อมทั้งหมดมากกว่า 90 % ภายใต้แสงแบล็กไลท์เมื่อฉายแสงเป็นเวลา 3 ชั่วโมง

Thesis Title Preparation and photocatalytic activity of Ag/ZnO powders

Author Miss Khanitta Intarasuwan

Major Program Chemistry

Academic Year 2012

ABSTRACT

In this work, the enhancing effects on photocatalytic efficiencies for ZnO powders were investigated by a morphological change and an addition of Ag metal. The morphological change of ZnO was studied by a variation of mixing rate between Zn^{2+} and OH^- solutions. When the Zn^{2+} reacts with OH^-, $Zn(OH)_2$ was the first precipitant that was subsequently transformed to ZnO in the alkaline medium during heating. The size of the urchin-like shape of the ZnO powder decreased with a decrease of the mixing rate. The large urchin-like shape also had a large diameter of hexagonal facet (0001) and showed the highest photocatalytic degradative activity on methylene blue.

The additional parameters studied in this work are Ag contents and order of Ag^+ addition. There are 2 methods for Ag^+ added order; Method 1, Ag^+ and Zn^{2+} were mixed together before OH^- addition and Method 2, Ag^+ was added in the suspension which formed from the reaction between Zn^{2+} and OH^-. In results, the amount of Ag less than 9 mol%, Ag/ZnO prepared from Method 2 showed the higher efficiency than those prepared from Method 1. When the Ag loading is greater than or equal to 9 mol%, the efficiencies of Ag/ZnO prepared from Method 1 were better than those prepared from Method 2. From the experimental results, ZnO with 9 mol% Ag prepared from Method 1 is the optimum condition. This also decolorizes the methylene blue, rhodamine B and reactive orange-16 dyes solutions and all efficiencies are more than 90 % under blacklight irradiation for 3 h.

CONTENTS

Page

CONTENTS (CONTINUED)

LIST OF TABLES

LIST OF FIGURES

LIST OF FIGURES (CONTINUED)

LIST OF FIGURES (CONTINUED)

LIST OF FIGURES (CONTINUED)

LIST OF FIGURES (CONTINUED)

CHAPTER 1

INTRODUCTION

1. Rational and problem statement

Water contamination is caused by various sources such as industrial effluents, chemical spills, domestic consumes and agricultural runoff. These effluents released into the rivers are highly contaminated and pose a potential environmental pollution (Qamar, *et al.,* 2005). Wastewater generated by the dye production industry and many other industries which use dyes and pigments is characteristically high in both color and organic content. Textile dyes and other industrials constitute one of the largest groups of organic compound that represent an increasing environmental danger. About 15% of the total world production of the synthetic textile dyes is lost during the dyeing process and is released in the textile effluents. The discharge of highly colored waste is not only aesthetically displeasing, but it also impedes light penetration, thus upsetting biological processes within a stream. In addition, many dyes are toxic to some organisms and may cause direct destruction of aquatic communities and human body. The toxicity of dye wastewater with aquatic life and human body is shown in Figure 1.

Figure 1. The toxicity of dye waste water with aquatic life and human body

The synthetic dyestuffs expelled into our rivers are complex chemical formulations containing some things that are very toxic to us, such as heavy metals (like lead, mercury, chromium, zinc, cobalt and copper), benzene and

formaldehyde. Many certifications, such as the new Global Organic Textile Standard (GOTS), restrict the kinds of chemicals allowed in certified products. For example, GOTS restricts amine releasing AZO dyes and disperse dyes (must be < 30 mg/kg); chromium, cobalt, copper, nickel, mercury, lead, antimony, and arsenic are all restricted (Du *et al.,* 2010). Heavy metal-containing dyes which are used extensively in the textile industry are toxic, potentially carcinogenic and have caused serious environmental pollution, since the complex aromatic structures of the organic dyes are resistant to light, biological activity and other degradative environmental conditions (Robinson *et al.,* 2001; Golka *et al.,* 2004; Zhao *et al.,* 2006). Some dye wastewater, containing various refractory organic pollutants from residual dye, is often discharged into the water environment without appropriate treatments. In order to remove refractory organic pollutants effectively from this kind of wastewater, the optimal treatment process with high quality effluent and low operating cost must be selected, and moreover appropriate operating conditions of the wastewater treatment process are required (Wang *et al.,* 2007).

With the increased demand for textile products, the textile industry and its wastewaters have been increasing proportionally, making it one of the main sources of severe pollution problems worldwide. In particular, the release of colored effluents into the environment is undesirable, not only because of their color, but also because many dyes from wastewater and their breakdown products are toxic and/or mutagenic to life (Stylidi *et al.,* 2003). Without adequate treatment these dyes are stable and can remain in the environment for an extended period of time. For instance, the half-life of hydrolysed Reactive blue 19 (RB19) is about 46 years at pH 7 and 25 °C (Hao *et al.,* 2000). In addition to the environmental problem, the textile industry consumes large amounts of potable water. In many countries where potable water is scarce, this large water consumption has become intolerable and wastewater recycling has been recommended in order to decrease the water requirements. Textile wastewaters are characterized by extreme fluctuations in many parameters such as chemical oxygen demand (COD), biochemical oxygen demand (BOD), pH, color and salinity. The wastewater composition will depend on the different organic-based compounds, chemicals and dyes used in the industrial dry and wet-processing steps

The most common textile-processing consists of desizing, scouring, bleaching, and dyeing processes. Sizing is the first preparation step, in which sizing agents such as starch, polyvinyl alcohol (PVA) and carboxymethyl cellulose are added to provide strength to the fibres and minimize breakage. Desizing is the employed next to remove sizing materials prior to weaving. Scouring then removes impurities from the fibers by using alkali solution (commonly sodium hydroxide) to breakdown natural oils, fats, waxes and surfactants, as well as to emulsify and suspend impurities in the scouring bath. Bleaching is the step used to remove unwanted color from the fibers by using chemicals such as sodium hypochlorite and hydrogen peroxide. Mercerizing is a continuous chemical process used to increase dye-ability, luster and fiber appearance. In this step a concentrated alkaline solution is applied and an acid solution washes the fibers before the dyeing step. Finally, Dyeing is the process of adding color to the fibers, which normally requires large volumes of water not only in the dye bath, but also during the rinsing step. Depending on the dyeing process, many chemicals like metals, salts, surfactants, organic processing assistants, sulphide and formaldehyde, may be added to improve dye adsorption onto the fibers (Kulkarni *et al.,* 1985).

Color has been included in the water quality standards for the discharge of industrial effluents in Thailand under the Environmental Quality (Industrial Effluents). It is difficult for most textile factories to adequately treat their wastewater. There is concern about the large volumes of effluent discharged from textile processing, which consumes large amounts of water resulting in the dye effluent was higher than the Standard Quality.

The liquid effluent data after treatment of some man-made fiber, dyeing and finishing integrated and printing mills are tabulated in Table 1. A comparison of the textile effluent and the standard for discharge of textile wastewater into receiving waters in Thailand shows that the liquid effluent after treatment in Thai textile sector is within the acceptable range of the effluent discharge standards.

Table 1. Range of liquid effluent after treatment in Thai textile industry

Type of mills	BOD		COD	
	mg/L	kg/ton	mg/L	kg/ton
Man-made fiber	18.2	0.5	32.8-67	0.18-0.9
Dyeing and finishing	6.6-33	0.05-3.85	84-152.7	0.34-5
Integrated textile	13	1.6	74	8
Printing	20-60	0.16-0.5	None	None
Thai standard	6.6-60	None	120-400	None

Dyeing and finishing, and printing mills have higher values of BOD, COD and TSS level compared to other type of mills. The BOD level in dyeing and finishing mills varies significantly. The variation of BOD and COD level in Thai textile mills is within the acceptable range of the effluent discharge to receiving waters in Thailand (Ministry of Science). The maximum value of BOD level in the printing mill is the same as that of the Thai standard. A standard for effluents from textile industry is shown in Table 2.

Table 2. Standards for effluents from textile industry (The Environmental Quality)

Parameter	mg/L (except for pH)
pH	5.5-9.0
Suspended solids	100
BOD	150
COD	250
Oil and grease	10
Total chromium (Cr)	2
Total Sulphide (S)	2
Phenolic compound (as C_6H_5OH)	1
Total residual chlorine	1

Note: Where the treated effluent is discharged into municipal sewer leading to terminal treatment plant, the BOD may be relaxed to 100 mg/L and COD to 400 mg/L.

The quantity of effluent (L/kg of product) shall not exceed 100, 250 and 80 in composite cotton textile industry, composite woolen textile industry and textile processing industry, respectively.

2. Dyes

A dye can generally be described as a colored substance that has an affinity to the substrate to which it is being applied. The dye is generally applied in an aquous solution, and may require a mordant to improve the fastness of the dye on the fiber. Both dyes and pigments appear to be colored because they absorb some wavelengths of light preferentially. In contrast with a dye, a pigment generally is insoluble, and has no affinity for the substrate. Some dyes can be precipitated with an inert salt to produce a lake pigment, and based on the salt used they could be aluminum lake, calcium lake or barium lake pigments.

Coloration is a key factor in the commercial success of textile products, particularly those with high fashion content, especially garments, furnishings and upholstery. Excluding fluorescent brighteners, the dye consumption per capita is approximately 150 g per year, serving an average consumption of textile fiber of about 1.45 million per year per inhabitant. Despite, the high economic importance of the textile industry in the world, this is responsible for over 7×10^5 metric tons of about 10,000 different types of dyes on pigment produced each year. During dye use among the several industries responsible for pollution of the aquatic ecosystems, the textile dyeing and printing industries are major players, around a half of a ton of these dyestuffs are lost per day to the environment. Approximately 200 liters of water are required, for every kilogram of finished cotton fabric. The reactions necessary to fix these dyes to the fibers are not very efficient. Therefore, residual dyes, several types of chemicals and salts are dumped into the water and are discharged in the water system. At least 15 % of those not used dyes might enter the environment through effluents from wastewater treatment plants (Carneiro *et al.,* 2004).

The first human-made (synthetic) organic dye was discovered by William Henry Perkin in 1856. Many thousands of synthetic dyes have since been prepared. Synthetic dyes quickly replaced the traditional natural dyes. They cost less, they offered a vast range of new colors, and they imparted better properties upon the dyed materials. Dyes are now classified according to how they are used in the dyeing process (Garfield, 2000).

(a) Acid dyes

Acid dyes are water-soluble anionic dyes that are applied to fibers such as silk, wool, nylon and modified acrylic fibers using neutral to acid dye baths. Attachment to the fiber is attributed, at least partly, to salt formation between anionic groups in the dyes and cationic groups in the fiber. Acid dyes are not substantive to cellulosic fibers. Most synthetic food colors fall in this category.

(b) Basic dyes

Basic dyes are water-soluble cationic dyes that are mainly applied to acrylic fibers, but find some use for wool and silk. Usually acetic acid is added to the dye bath to help the uptake of the dye onto the fiber. Basic dyes are also used in the coloration of paper.

(c) Direct dyes

Direct or substantive dyeing is normally carried out in a neutral or slightly alkaline dye bath, at or near boiling point, with the addition of either sodium chloride (NaCl) or sodium sulfate (Na_2SO_4). Direct dyes are used on cotton, paper, leather, wool, silk and nylon. They are also used as pH indicators and as biological stains.

(d) Mordant dyes

Mordant dyes require a mordant, which improves the fastness of the dye against water, light and perspiration. The choice of mordant is very important as different mordants can change the final color significantly. Most natural dyes are mordant dyes and there is, therefore, a large literature base describing dyeing techniques. The most important mordant dyes are the synthetic mordant dyes, or chrome dyes, used for wool; these comprise some 30% of dyes used for wool, and are especially useful for

black and navy shades. The mordant, potassium dichromate, is applied as an after-treatment. It is important to note that many mordants, particularly those in the heavy metal category, can be hazardous to health and extreame care must be taken in using them.

(e) Vat dyes

Vat dyes are essentially insoluble in water and incapable of dyeing fibres directly. However, reduction in alkaline liquor produces the water soluble alkali metal salt of the dye, which, in this leuco form, has an affinity for the textile fibre. Subsequent oxidation reforms the original insoluble dye. The color of denim is due to indigo, the original vat dye. Covalent bonds that attach reactive dye to natural fiber.

(f) Reactive dyes

Reactive dyes utilize a chromophore attached to a substituent that is capable of directly reacting with the fibre substrate. The covalent bonds that attach reactive dye to natural fibre make them among the most permanent of dyes. “Cold” reactive dyes, such as Procion MX, Cibacron F, and Drimarene K, are very easy to use because the dye can be applied at room temperature. Reactive dyes are by far the best choice for dyeing cotton.

(g) Dispers dyes

Disperse dyes were originally developed for the dyeing of cellulose acetate, and are substantially water insoluble. The dyes are finely ground in the presence of a dispersing agent and then sold as a paste, or spray-dried and sold as a powder. Their main use is to dye polyester but they can also be used to dye nylon, cellulose triacetate, and acrylic fibers. In some cases, a dyeing temperature of 130 °C cellulose triacetate, and a pressurized dye bath is used. The very fine particle size gives a large surface area that acids dissolution to allow uptake by the fibers. The dyeing rate can be significantly influenced by the choice of dispersing agent used during the grinding.

(h) Azo dyeing

Azo dyeing is a technique in which an insoluble azoic dye is produced directly onto or within the fibre. This is achieved by treating a fiber with both diazoic and coupling compents. With suitable adjustment of dyebath conditions the two components react to produce the required insoluble azo dye. This technique of dyeing is unique, in that the final color is controlled by the choice of the diazoic and coupling components.

(i) Sulfur dyes

Sulfur dyes are the most commonly used dyes manufactured for cotton in terms of volume. They are cheap, generally have good wash-fastness and are easy to apply. The dyes are absorbed by cotton from bath containing sodium sulfide or sodium hydrosulfite and are made insoluble within the fibre by oxidation.

In the present work, it was attempted to establish the degradation of a dye present in colored aqueous. Methylene blue (Basic dye), Rhodamine B (Basic dye), and Reactive Orange 16 (Azo dye), were used as model compounds. These dyes were chosen due to its high chemical and biological resistance to degradation by conventional procedures, which are attributed to chromophore group. The structures of three dyes were shown in Figure 2.

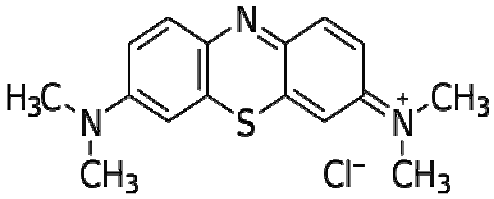

(a) Methylene blue

(Mills, *et al.,* 1999)

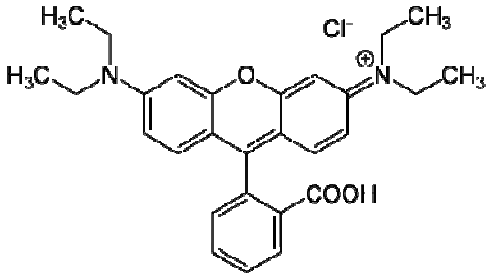

(b) Rhodamine B

(Byrappa, *et al.,* 2006)

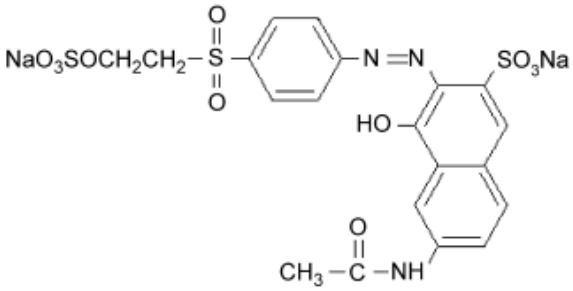

(c) Reactive Orange 16

(Sung Wook, *et al.,* 2005)

Figure 2. Structure of (a), Methylene blue (b), Rhodamine B and (c) Reactive Orange 16

Hence, removal of dyes from such wastewaters is a major environmental problem complete dye removal is necessary because dyes will be visible even at low concentrations. Therefore it is important to develop effective wastewater remediation technologies for these compounds (Houas *et al.,* 2001; Konstantinou and Abanis, 2004; Senthikumarr *et al.,* 2005).

Color is usually the first contaminant to be recognized in wastewater, which generated by using synthetic dyes in the industrials. Considering both discharged volumes and effluent composition, the wastewater generated by the textile industry is rated as one of the most polluting among all industry sectors. With the great variety of fibers, dyes process aids and finishing product in use. The textile industry generated wastewater of great chemical complexity, diversity and volume (Bizani, *et al.,* 2006). Synthetic dyes are extensively used in the textile industries because of their simple dyeing procedure and good stability during washing process. Over 10,000 dyes with an annual production over 7×10^5 metricton world wide are lost in the industrial effluents during manufacturing and processing operations. Synthetic dyes, classified by their chromophores, have different and stable chemical structures to meet various coloring requirements (Toor, *et al.,* 2006). When, the release of this colored wastewater in the eco-system is a dramatic source of aesthetic pollution. Being released into the environment, these dyes not only impart colors to water sources but also damage living organisms by stopping the reoxygenation capacity of water, blocking sunlight, and therefore disturbing the natural growth activity of aquatic life (Wang, 2008 and Song and Bo Bai, 2010. Therefore, the removal of colored wastewater is a necessary before being released into the environment (Senthikumaar, *et al.,* 2005).

Traditional techniques used for color removal are filtration, activated carbon (charcoal), and coagulation. Each method has few advantages and disadvantages. For example, the use of charcoal is technically easy but has high waste disposal cost. Coagulation using alums, ferric salts or limes is a low cost process, but all these methods have a major disadvantage of simply transferring the pollutant from one phase to another phase rather than destroying them and sometime the by-products

may be more toxic than the dye itself. Biological treatment is a proven method and cost effective. However, it has been reported that majority of dyes are adsorbed on the sludge and very long degraded times, due to the biorecalcitrant nature of these dyes molecules. This leads to a search for highly effective method to degrade the dye into environmentally compatible products (Toor, *et al.,* 2006).

In recent years, attention has been focused on heterogeneous photocatalysis for the treatment for the treatment of recalcitrant chemical present in the wastewater. Among these heterogeneous photocatalysis in the present of irradiated semiconductors, ZnO has been successfully used to decolorize and mineralize many organic pollutants including several dyes and their intermediates present in aqueous systems using both artificial light and under sunlight using solar technology (Muruganandham, *et al.,* 2005). ZnO is the most widely used photocatalyst because of its good activity, chemical stability, wide and direct band gap, commercial availability, environmentally friendly feature and inexpensiveness. It is generally used as a photocatalyst for environmental applications such as air purification, water disinfection, hazardous waste remediation and water purification (Nagaveni, *et al.,* 2004).

3. Background of zinc oxide (ZnO)

As far as nanomaterial is concerned, ZnO is one of the candidate which has been attracting attention due to its numerous interested properties. Zinc oxide is a chemical compound with the formula ZnO. It is produced by two main different processes. In the direct or American method, zinc ores (or residues) are heated in air with coke or anthracite, and the resulting zinc vapour is subjected to controlled oxidation. In the indirect or French method, the zinc vapour to be oxidized is obtained by boiling zinc (http://en.wikipedia.org/wiki/zinc-oxide).

ZnO is nearly insoluble in acids and bases. It characterizes as white powder commonly known as zinc white. It occurs in nature as the mineral zincite. Crystalline ZnO exhibits the piezoelectric effect and ZnO performs a thermochrome characteristic by changing from white to yellow when heating, and vice versa. The ZnO has been

widely studied since 1935. ZnO is a well-known semiconductor with a wide direct band gap (3.37 eV) and large exciton binding energy of about 60 meV at room temperature (http://en.wikipedia.org/wiki/zinc-oxide).

Table 3. Properties of zinc oxide.

Properties	
Molecular formula	ZnO
Molar mass (g/mol)	81.408
Density (g/cm^3)	5.606
Melting Point ($^\circ C$)	1975
Boiling Point ($^\circ C$)	2360
Refractive Index	2.0041

3.1. Applications of ZnO powder

ZnO powder has been commonly used for over a hundred years in a wide range of applications, for example,

(a) Medical applications

A mixture of ZnO and 0.5% Fe_2O_3 (calamine) is used in calamine lotion and a mixture of ZnO and eugenol (zinc oxide eugenol) has restorative and prosthodontic applications in dentistry (http://en.wikipedia.org/wiki/zinc-oxide). Moreover, the ZnO nanopowders can use as antimicrobial agent (Mungkornasawakul, *et al.,* 2005).

(b) Food additive

ZnO is added to many breakfast cereals acting as a source of zinc that is a necessary nutrient for ZnO based medicament for preventing and treating diarrhea in farm animals (http://www.freepatentsonline.com/EP1593381.html).

(c) Pigment

Over the past century, the paint industry (in its constant development of improved products) has utilized various aspects of those properties to high degree. Manufacturers discovered that they could produce the coatings of brushing consistency and good suspension properties by incorporation of ZnO into their pastes.

Zinc white is used as a pigment in paints. In general, zinc white is more opaque than lithopone, but it is less opaque than titanium dioxide. It is also used in coating for paper. Chinese white is a special grade of zinc white used in artists' pigments, because it can absorb both UVA and UVB rays of ultraviolet light. Interestingly, the current state-of-the-art thermal control coatings (TCCs) system utilizes ZnO pigment to maintain solar reflectance over a long exposure time (http://cat.inist.fr/?aModele=afficheN&cpsidt =15369294).

(d) Cosmetic applications

ZnO is applied in cosmatics to protect the UV radiation for human (Samontha, et al). ZnO can be used in ointments, creams, and lotions to protect against sunburn and other damages to the skin caused by ultraviolet light. It is the broadest spectrum UVA and UVB absorber that is approved for use as a sunscreen by the Food and Drug Administration (FDA), and is completely photostable and it is also a main ingredient of mineral make up (http://www.goldbamboo.com/topic-t4989-a1-6Zinc_Oxide.html).

(e) Rubber manufacture

ZnO proved the most effective activator to speed up the rate of cure with the new accelerators. It provides reinforcement in natural rubber, and in some synthetic elastomers such as polysulfides and chloroprenes. The degree of reinforcement depends upon a combination of the particle size, the finest size being the most effective. ZnO is the chemical reactivity that utilized to activate the organic accelerator. The unreacted portion of ZnO remains available as a basic reserve to neutralize the sulfur-bearing acidic decomposition products formed during vulcanization. Adequate levels of ZnO contribute markedly to chemical reinforcement, scorch control, resistance to heat-aging and compression fatigue. Additional ZnO also provides heat conduction to more rapidly dissipate the heat and thereby provides lower operating temperatures. In addition, it imparts heat stabilization by reacting with acidic decomposition products (http://navbharat.co.in/clients.htm).

(f) Plastic applications

Zinc compounds can provide a variety of properties in the plastic field. Heat resistance and mechanical strength are imparted to acrylic composites by ZnO. Addition of ZnO to epoxy resins cured with aliphatic polyamines imparts higher tensile strength and water resistance. ZnO is also useful in the preparation of nylon polymers and in increasing their resistance and reacts with unsaturated polyesters to form higher viscosity and a thixotropic body. ZnO increases the transparency of poly (chlorofluoro ethylene) molding resin. Polyolefin's are improved in color, tensile strength, and vulcanization properties by addition of ZnO. Applications in development for zinc oxide-stabilized polypropylene and high-density polyethylene include safety helmets, stadium seating, insulation, pallets, bags, fiber and filament, agricultural and recreational equipment
(http://navbharat.co.in/clients.htm).

(g) Electronic applications

The most common applications of ZnO are in laser diodes and light emitting diodes (LEDs) since it has an exciton and biexciton energies of 60 meV and 15 meV, respectively. Additional it is inexpensive. Most ZnO has an *n*-type character even in the absence of intentional doping. The native defects such as oxygen vacancies or zinc interstitials are often assumed to be the origin of this, but the subject remains controversial. The *n*-type doped films are often used in thin film technology, where ZnO serves as a transparent conducting oxide (TCO). The *n*-type doping is possible by introduction of group III elements such as Al, Ga or In. These group III elements can generate the donor state near the conduction band and they can generate the excess electrons at the bottom of conduction band. On the contrary, it is difficult to dope ZnO as *p*-type semiconductor due to the high activation energy of acceptor, low solubility of acceptor dopants and self-compensating process on acceptor doping caused by intrinsic defects. Recently, the strategy of *p*-type ZnO semiconductor is an active area of research. Thin-film solar cells, liquid crystal display (LCD) and flat panel displays are typical applications of *p*-type ZnO semiconductor material. Appropriately doped ZnO may be transparent and conductive, and they can therefore be used as a transparent conducting oxide in some important devices in place of

indium doped tin oxide (ITO) material. Beside, conducting ZnO material is a good infrared reflectors and can be used as energy efficent windows that require high reflective index and high transmittance in the visible range. (http://www.eurekalert/pab.releases/2007.01/uoc--clfo10207.html)
(http://en.wikipedia.org/wiki/zinc-oxide)

(h) Sensor applications

ZnO can use for pyroelectric sensors. It possesses the advantages of being integrable with on-chip circuitry, un-cooled detecting, room-temperature operation, fast and wide spectral response with high sensitivity and low cost (Hsiao *et al*., 2008). ZnO material can be used in sensing and/or monitoring different types of gases both toxic and harmful gases as chlorine (Cl_2) due to it low cost, high sensitivity, excellent selectivity quick response behavior, sulfur hexafluoride, butane ethanol and gasoline (Majumder *et al*., 2003; Xu *et al.,* 2000; Xinshu *et al*., 2004)

3.2. Crystallographic data of ZnO

ZnO exists in three forms depending on pressure. At ambient pressure, ZnO is in the stable hexagonal wurtzite (ZnO_W) form and some ZnO is in the metastable cubic zinc-blend (ZnO_{ZB}) form. At moderate and high pressure (8-10 GPa), ZnO is in the rock-salt (ZnO_{RS}) form. The difference between the critical pressure for the ZnO_{ZB} to ZnO_{RS} and ZnO_W to ZnO_{RS} transition is very small and so the energy difference between ZnO_W and ZnO_{RS} is also very small. Thus, the ZnO_W to ZnO_{RS} transition can occur due to the topotactic transformation based on the network of oxygen and zinc (Qteish, 2000; Serrano *et al*., 2004)

At ambient pressure and temperature, ZnO crystallizes in the wurtzite (*B4* type) structure whose underlying Bravais lattice in hexagonal (space group $P6_3\,mc = C^4_{6v}$). The structure of ZnO is illustrated in Figure 3 Under ambient condition, its lattice parameters are a = 3.2489 (1) Å and c = 5.2053 (4) Å. Both kinds of atoms are located in Wyckoff position:

$$2(b) = \frac{1}{3}\frac{2}{3}v,\ \frac{2}{3}\frac{1}{3}\ v + \frac{1}{2}$$

and the arrangements are in the positions:

$$\text{Zn: } 000,\ \frac{1}{3}\frac{2}{3}\frac{1}{2}$$

$$\text{O: } 00u,\ \frac{1}{3}\frac{2}{3}u+\frac{1}{2}$$

In an ideal wurtzite crystal, the axial ratio $c/a = (8/3)^{1/2}$ and $u = 3/8$. Experimentally, the real values of u and c/a of wurtzite ZnO were, however, determined in the range of $u = 0.3817$ to 0.3856 and $c/a = 1.593$ to 1.6035.

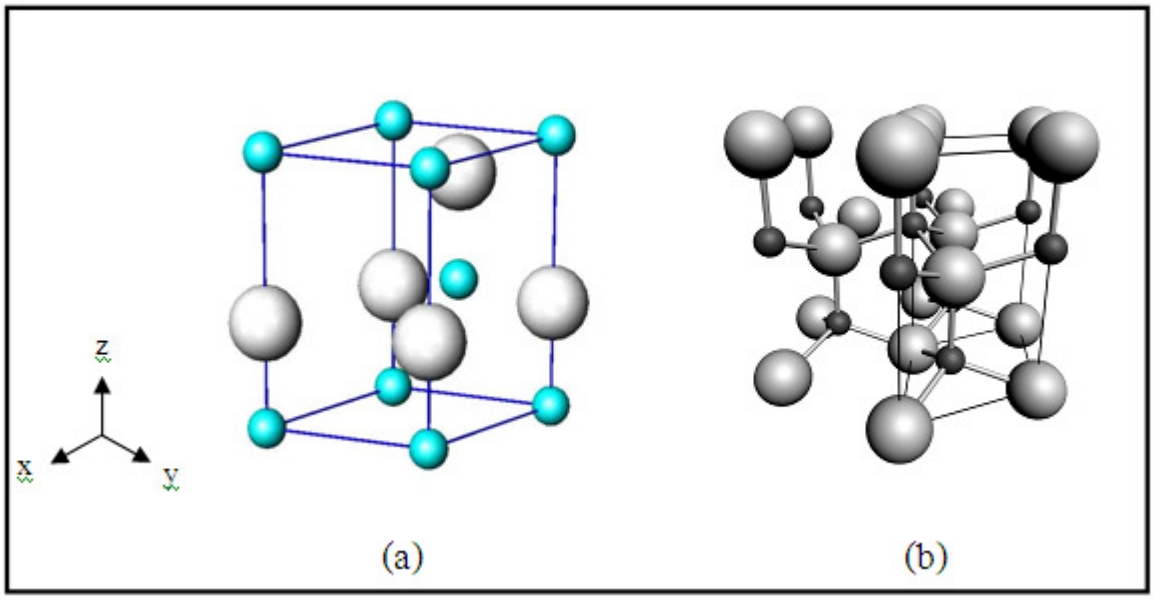

Figure 3. A drawing shows; (a) unit cell of ZnO and (b) tetrahedral coordination in ZnO. Big and small spheres represent oxygen and zinc atoms, respectively.
Source: http://www.geocities.jp/ohba_lab_ob_page/Structure/ZnO_Wurtzite.jpg
Source: Jagadish and Pearton (2006)

ZnO wurtzite structure is characterized by tetrahedral coordination of ion of one kind (e.g. Zn^{2+}) by the ions of another kind (e.g. O^{2-}) as composed of ZnO_4, or OZn_4, tetrahedral (Figure 4.2.1 b). They are stacked in a hexagonal close-packed array with the tetrahedral edges of alternate layers rotated through 180° around the *c*-axis. The tetrahedral coordination of this compound is also a common indicator of sp^3 covalent bonding (the Zn *d*-electrons hybidrize with the O *p*-electrons). However, the bonding

between the Zn atoms and O atoms are highly ionic, due to the large difference in their electronegative values (1.65 for Zn and 3.44 for O) thus ZnO lies on the borderline between being classed as a covalent and ionic compound.

4. Photocatalytic process

In recent years, many researchers have been focused on heterogeneous photocatalysis for the treatment of recalcitrant chemical present in the wastewater. Among these heterogeneous photocatalysis in the presence of irradiated semiconductors (TiO_2, WO_3, SnO_2, ZnO, CdS, and others), ZnO has been successfully used to decolorize and mineralize many organic pollutants including several dyes and their intermediates present in aqueous systems using both artificial light and under sunlight using solar technology (Muruganandham, *et al.,* 2005). ZnO is the most widely used photocatalyst because of its good activity, chemical stability, commercial availability and inexpensiveness. It is generally used as a photocatalyst for environmental applications such as air purification, water disinfection, hazardous waste remediation and water purification (Nagaveni, *et al.,* 2004). The efficiency of advanced oxidation processes for degradation of recalcitrant compounds has been extensively documented. Photochemical processes are used to degrade toxic organic compounds to CO_2 and H_2O without the use of additional chemical oxidants, because the degradation is assisted by high concentrations of hydroxyl radicals ($OH^{\bullet}$) generated in the process. In this case, the photoexcitation of ZnO particles promotes an electron from the valence band to the conduction band, generating an electron (e_{CB}^-)/hole (h_{VB}^+) pair. Both reductive and oxidative processes can occur at or near the surface of the photoexcited ZnO particle. In general, oxygen is used to scavenge the conduction band electron, producing a superoxide anion radical ($O_2^{\bullet -}$), effectively preventing electron (e_{CB}^-)/hole (h_{VB}^+) recombination, and prolonging the lifetime of the hole. The photogenerated hole has the potential to oxidize several substrates by electron transfer. In aqueous solutions, oxidation of water to hydroxyl radical ($OH^{\bullet}$) by the photogenerated hole appears to be the predominant pathway. Hydroxyl radicals ($OH^{\bullet}$) and, to a lesser extent, superoxide anion can act as oxidants, ultimately leading to the mineralization of organic compounds (Moraes, *et al.,* 2000)

The mineralization of most of the organic pollutants could be degraded following the usually proposed mechanism (Eqs.1-9); for the heterogeneous photocatalytic oxidation processes as shown in Figure 4.

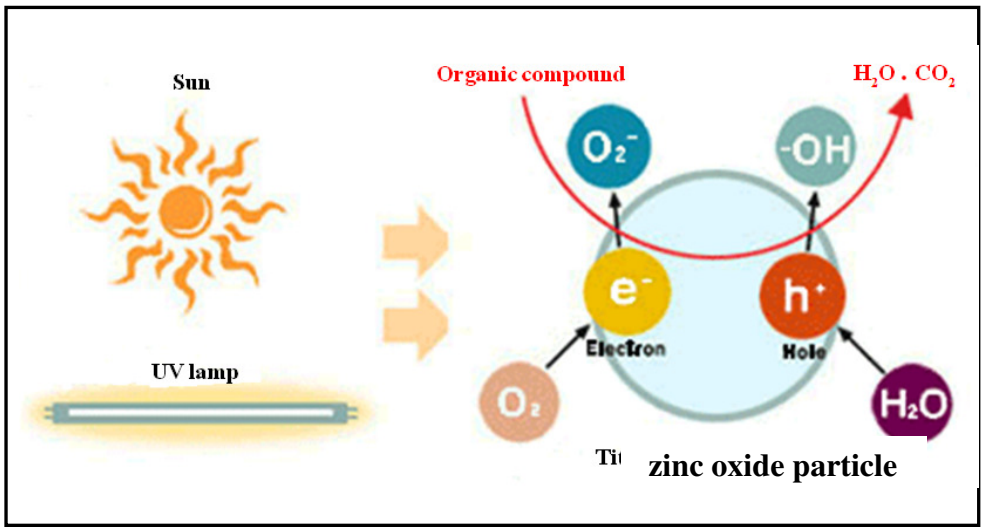

Figure 4. The heterogeneous photocatalytic oxidation processes of zinc oxide photocatalyst
Source: (http://dev.nsta.org).

1. Absorption of efficient photons ($h\nu > E_g = 3.37$ eV) by zinc oxide

$$ZnO + h\nu \longrightarrow e_{CB}^- + h_{VB}^+ \quad (1.1)$$

2. Oxygen ionosorption (first step of oxygen reduction; oxygen's oxidation state changes from 0 to -1/2)

$$(O_2)_{ads} + e_{CB}^- \longrightarrow O_2^{\bullet -} \quad (1.2)$$

3. Neutralization of OH^- groups by photoholes which produces $OH^\bullet$ radicals

$$(H_2O \leftrightarrow H^+ + OH^-)_{ads} + h_{VB}^+ \longrightarrow H^+ + OH^\bullet \quad (1.3)$$

4. Neutralization of $O_2^{\bullet-}$ by protons

$$O_2^{\bullet-} + H^+ \longrightarrow HO_2^{\bullet} \quad 1.4$$

5. Transient hydrogen peroxide formation and dismutation of oxygen

$$2\ HO_2^{\bullet} \longrightarrow H_2O_2 + O_2 \quad 1.5$$

6. Decomposition of H_2O_2 and second reduction of oxygen

$$H_2O_2 + e^- \longrightarrow OH^{\bullet} + OH^- \quad 1.6$$

7. Oxidation of the organic reactant via successive attacks by $OH^{\bullet}$ radicals

$$R + OH^{\bullet} \longrightarrow R^{\bullet} + H_2O \quad 1.7$$

8. Direct oxidation by reaction with holes

$$R + h^+ \longrightarrow R^{+\bullet} \longrightarrow \text{Degradation products} \quad 1.8$$

As an example of the last process, holes can react directly with carboxylic acid generating CO_2:

$$RCOO^- + h^+ \longrightarrow R^{\bullet} + CO_2 \quad 1.9$$

The photocatalytic mechanism of ZnO has been well established and is summarized in Scheme 1. The reaction begins with ZnO particles being excited with UV light resulting in the formation of electron-hole pair, Eq.1.10. The electron in the conduction band, e_{cb}^-, and the hole in the valence band, h_{vb}^+, may recombine and nullify further reactions. The e_{cb}^- – h_{vb}^+ pair, if they survive from recombination process, will eventually diffuse to the bulk surface and react with other molecules nearby. The e_{cb}^- can react with molecular O_2 adsorbed at the bulk surface and after few more steps will lead to the formation of $OH^{\bullet}$ radical, Eqs.1.11-1.14, plays a major role in photocatalytic reaction. The h_{vb}^+ can react with H_2O at the bulk surface leading to formation of $OH^{\bullet}$ radical as well, Eq.1.15. The very reactive $OH^{\bullet}$ radical can go on

by attacking the dye molecules to completely mineralize them, Eq.1.16. In addition, the h_{vb}^+ itself can also attack and mineralize dye molecules, Eq.1.17 (Houas, *et al*., 2001; Anpo, *et al*., 2003).

$$ZnO + hv \longrightarrow e_{cb}^- + h_{vb}^+ \quad 1.10$$

$$O_{2ads} + e_{cb}^- \longrightarrow O_2^{\bullet -} \quad 1.11$$

$$O_2^{\bullet -} + H^+ \longrightarrow {}^{\bullet}OOH \quad 1.12$$

$$2\,{}^{\bullet}OOH \longrightarrow H_2O_2 + O_2 \quad 1.13$$

$$H_2O_2 + e_{cb}^- \longrightarrow OH^{\bullet} + OH^- \quad 1.14$$

$$H_2O_{ads} + h_{vb}^+ \longrightarrow H^+ + OH^{\bullet} \quad 1.15$$

$$Dye + OH^{\bullet} \longrightarrow \text{Degradation products} \quad 1.16$$

$$Dye + h_{vb}^+ \longrightarrow \text{Degradation products} \quad 1.17$$

Scheme1. Mechanism of ZnO photocatalyst.

5. Precipitation method

In recent years, it has been found that ZnO powders can be synthesized by various routes such as vapor phase deposition, sonochemical precipitation, sol –gel and precipitation methods. Diverse fabrication techniques, such as thermal evaporation, molecular beam epitaxy, vapor phase transport, chemical vapor deposition (CVD), metal organic, aqueous solution deposition, and electrochemical deposition, have been attempted to grow the materials with partial success due to small repeatability at large-scale. Hence, it is conceived that preparation of ZnO powders via chemical routes without involving catalyst or templates provides promising option for the large-scale production of well dispersed materials. Among wet chemical methods, precipitation has many advantages over the other methods, for example, it is unsophisticated and a low cost method. Thus, the development of low cost and simple synthesis routes to produce ZnO powders may lead to improvements in material properties for specified applications.

Bai, *et al.,* (1995) prepared the spherical ZnO powders for varistor by an aqueous precipitation method. The varistor samples made from the ZnO powders using butylamine and urea as precipitant show excellent surge response characteristics. The ZnO powders precipitated by butylamine had smaller and more homogeneous size than those precipitated by urea.

Rodriguez, *et al.,* (2001) investigated the many parameters to control the growth mechanism of ZnO nanostructure. ZnO nanoparticles with different morphologies have been obtained by controlling different parameters of the precipitation process such as solution concentration, pH and washing medium. The reactions leading to the formation of zinc metastable complexes were followed by potentiometric and conductimetric titrations. During the ethanol washing step the intermediate zinc complexes have been modified by weathering and solution processes which drived both the phase transformation reactions and the particles recrystallization.

Zhang, *et al.,* (2003) prepared ZnO particles by precipitation transformation method and explained its inherent formation mechanisms. The ZnO particles were prepared by implementing the precipitation transformation method from $Zn_5(CO_3)_2(OH)_6$ in an aqueous solution at a low temperature (room temperature to 70 °C). The phase transformation process was detected by using a pH-meter and an X-ray diffraction (XRD). With an increase of temperature concentration and quantity of NaOH solution, the ZnO phase became easier to form, otherwise, the ε-$Zn(OH)_2$ phase would need to be formed. With the decrease of the concentration of Zn^{2+} solution, $Zn_5(OH)_6(CO_3)_2$ phase is more easy to transform to ε-$Zn(OH)_2$ and the ZnO cannot be obtained. The pure ZnO phase was obtained from 1 mol/L Zn^{2+} solution, and the nearly pure ε-$Zn(OH)_2$ phase was obtained from 0.02 mol/L Zn^{2+} solution.

Han, *et al.,* (2006) prepared the homogeneous ZnO nanoparticles via precipitation-pyrolysis with $Zn_5(CO_3)_2(OH)_6$ as precursor. From the results, it can be explained that the growth behaviors of epitaxy along the *c*-axis are responsible for the morphology of ZnO changing from sphere to rod-like shape, to reticulation. And then to compared with other synthesis approaches, precipitation-pyrolysis method can get fairly good product with a relatively low cost.

Wang, *et al.,* (2010) prepared ZnO nanoparticles using the direct precipitation method in a membrane dispersion microstructured reactor. The effects of calcination temperatures for the precursors, calcination time, feed concentrations, and feed flow rates on the crystal sizes of ZnO nanoparticles were investigated. ZnO nanoparticles were prepared using $ZnSO_4$ and NH_4HCO_3 aqueous solutions as feedstocks in a membrane dispersion micro-structured reactor exhibiting efficient mixing. The mechanisms to transformed ZnO as shown

$$5ZnSO_4(aq) + 10NH_4HCO_3(aq) \rightarrow Zn_5(CO_3)_2(OH)_6(s) + 5(NH_4)_2SO_4(aq) + 8CO_2(g) + 2H_2O(l)$$

$$Zn_5(CO_3)_2(OH)_6\,(s) \quad \rightarrow \quad 5ZnO(s) + 2CO_2(g) + 3H_2O(g)$$

Medina, *et al.,* (2012) prepared the ZnO nanoparticles with hexagonal shape by using chemical precipitation. The condition was a molar ratio of $Zn(H_3C_2O_2)_2{\cdot}2H_2O$:NaOH of 1:1. XRD demonstrated that all hexagonal particles formed are of wurtzite crystal structure with preferable [0001] growth direction. The experimental results indicate that chemical precipitation method provides a simple way for synthesis that can be applied to other materials.

Lanje, *et al.,* (2012) used zinc nitrate as a precursor and starch as a stabilizing agent, to synthesize ZnO by precipitation method as shown in Figure 5. The increase of a.c. conductivity of ZnO with the temperature comes from the mobility of charge carriers which is responsible for hopping and electronic polarization in ZnO nanoparticles.

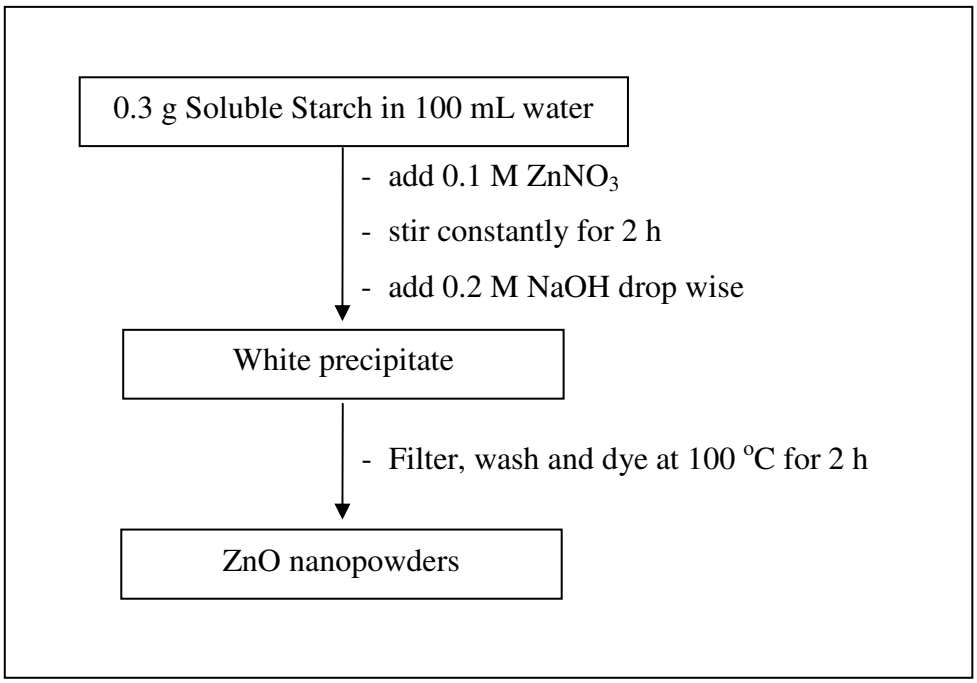

Figure 5. Flow chart for the preparation of ZnO nanoparticles

Raoufi, *et al.,* (2012) synthesized and studied the microstructural properties of ZnO nanoparticles prepared by precipitation method. ZnO precursor was prepared by precipitation method from zinc nitrate and ammonium carbonate in aqueous solutions after that this precursor was annealed at different temperature to obtain ZnO nanoparticles as shown in Figure 6. The XRD results indicated that the synthesized ZnO nanoparticles had the pure wurtzite structure. It is found that with increasing the annealing temperature, the crystalinity and particle size increases as well as the lattice parameters approaches to those of the XRD standard.

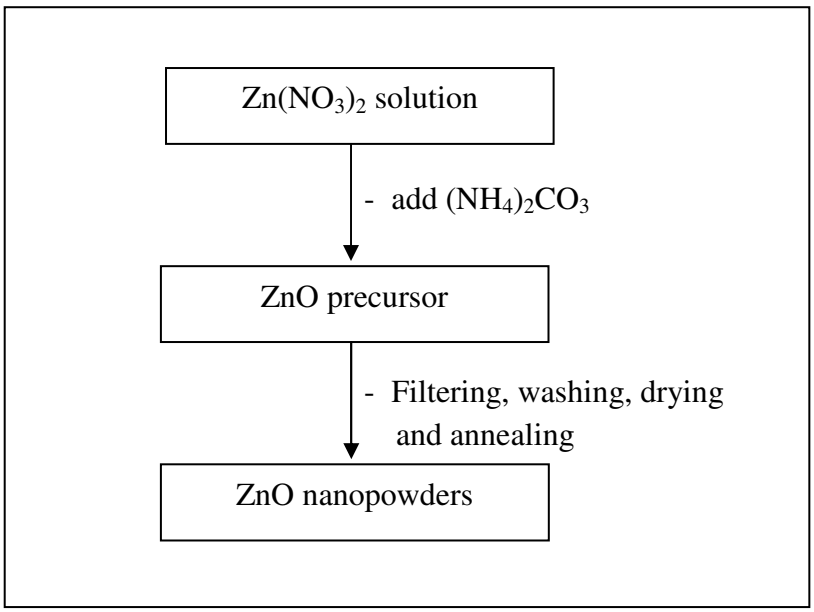

Figure 6. Flow chart for the preparation of ZnO nanoparticles by precipitation method

6. Heterostructure of metal/ZnO

Photoexcitation of semiconductor oxide photocatalyst by UV light results in the generation of electron–hole pairs which enable the production of hydroxyl radicals in water. A major limitation of achieving high photocatalytic efficiency in the semiconductor photocatalyst is the rapid recombination of photo-induced charge carriers. The charge separation efficiency can be improved by using semiconductor composite or depositing metal nanoparticles on the semiconductor. Deposition of noble metals on semiconductor photocatalysts can enhance their photocatalytic activities. Those noble metals for doping ZnO powders such as manganese (Mn), platinum (Pt), gold (Au), palladium (Pd), copper (Cu), silver (Ag) and so forth.

Tuning the performance and activity of nanocrystalline ZnO by doping with Ag is of current interest. ZnO behaves as an n-type semiconductor and Ag doping is found to be effective for the fabrication of p-type ZnO. In addition, Ag doping modifies the optical and electronic properties, which in turn influence the photocatalytic activity. The present work reveals larger bactericidal and photocatalytic activities of precipitation synthesized ZnO and Ag-doped ZnO because of the

precipitation method is simple method, controllability, reliability, low cost and low reaction temperature. The other methods to preparate of nanoparticulate Ag-ZnO such as sol-gel, chemical, photochemical, used hydrothermal, or solvothermal, microwave, flame spray pyrolysis, electrospinning and RF magnetron sputtering.

In particular, Ag doping in ZnO for the generation of p-type conductivity is an exciting area of research wherein silver acts as an electron acceptor in the material. Moreover, the photocatalytic activity of ZnO is improved by silver addition, which has been attributed to the doping induced surface properties, such as oxygen vacancies and crystal defects. However, first principle calculations on the doping limit of Ag in stoichiometric ZnO show that the formation energy of Ag in the favorable O-rich conditions is 0.85 eV, which corresponds to the solubility limit of about 10^{18} cm^{-3} at 700 ^{o}C (Ranjan *et al*., 2011).

The photoexited electrons and holes can also recombine to reduce photocatalytic activity of the semiconductor. To overcome this limitation, modification of semiconductors with noble metals is one of the most efficient ways. Ag/ZnO composite structure is now an exciting area in research for developing photocatalytic applications. Ag is known as electron sinks due to the Schottky barrier at the metal-semiconductor interface, then after step 1.1 as mentioned above (page 16), electron in CB can transfer to Ag deposit the mechanism as shown in Figure 7.

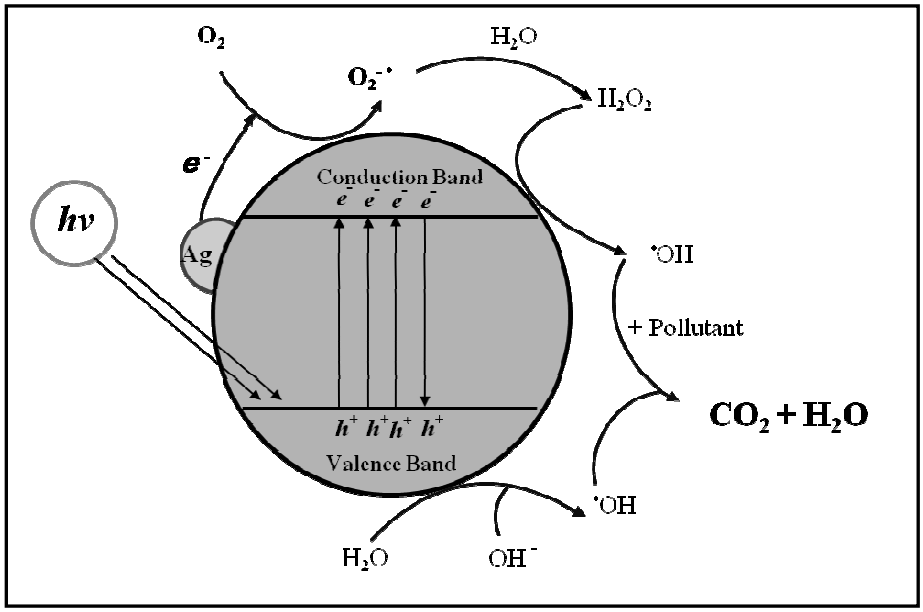

Figure 7. Mechanism of photocatalysis in Ag deposited ZnO under UV light irradiation.

Zhang, *et al.,* (2011) reported that the photocatalytic process of the Ag/ZnO composite is complex and controversial. As we know, the work function of ZnO (5.2 eV) is larger than that of Ag (4.26 eV), implying that the electrons will migrate from silver to the conduction band (CB) of ZnO to achieve the Fermi level equilibration when they get into contact. The process can be expressed as:

$$Ag \longrightarrow Ag^{+} + e^{-} \qquad 1.18$$

When the catalysts are illuminated by UV light with photon energy higher than the band gap of ZnO, electrons (e^{-}) in the valence band (VB) can be excited to the CB with simultaneous generation of the same amount of holes (h^{+}) left behind. The photocatalytic reaction can be thus expressed as follows: (equation 1.19-1.25)

$$ZnO + h\nu \longrightarrow h^+ + e^- \quad 1.19$$

$$h^+ + OH^- \longrightarrow {}^{\bullet}OH \quad 1.20$$

$$h^+ + H_2O \longrightarrow {}^{\bullet}OH + H^+ \quad 1.21$$

$$e^- + Ag^+ \longrightarrow Ag \quad 1.22$$

$$e^- + O_2 \longrightarrow {}^{\bullet}O_2^- \quad 1.23$$

$${}^{\bullet}O_2^- + H^+ \longrightarrow {}^{\bullet}O_2H \quad 1.24$$

$$2{}^{\bullet}O_2H \longrightarrow H_2O_2 + O_2 \quad 1.25$$

Lu, *et al.,* (2008) reported that the positive effect of Ag deposits is commonly due to the fact that Ag nanoparticles on the semiconductor surface behave like electron sinks, which provide sites for the accumulation of photogenerated electrons, and then improve the separation of photogenerated electrons and holes. This can be understood based on the proposed charged separation of Ag/ZnO under UV irradiation as shown in Figure 8. Because the bottom energy level of the CB of ZnO is higher than the new equilibrium Fermi energy level (E_f) of Ag/ZnO, the photoexcited electrons on the CB under UV irradiations can transfer from ZnO to Ag nanoparticles. It has been proposed that the charge separation is the outcome of a Schottky barrier formed at the metal-semiconductor interface. Therefore, Ag nanoparticles, acting as electron sinks, reduce the recombination of photoinduced electrons and holes, and prolong the lifetime of the electron pairs. Subsequently, the electrons can be captured by the adsorbed O_2, and the holes can be trapped by the surface hydroxyl, both resulting in the formation of hydroxyl radical species (${}^{\bullet}OH$). It is accepted that hydroxyl radical species show little selectivity for attacking dye molecules and are able to oxidize the pollutants due to their high oxidative capacity Thus, the possible mechanistic pathway of Ag/ZnO for degradation can be proposed as follows: (equation 1.29-1.31)

$$ZnO + h\nu(UV) \longrightarrow ZnO(e^-_{cb} + h^+_{vb}) \quad 1.26$$

$$Ag \longrightarrow Ag^+ + e^- \quad 1.27$$

$$e^- + O_2\,(ads) \longrightarrow {}^{\bullet}O^-_2 \longrightarrow {}^{\bullet}O_2H \xrightarrow{{}^{\bullet}O_2H} O_2 + H_2O_2 \xrightarrow{e^-} O_2 + {}^{\bullet}OH + OH^- \quad 1.28$$

$$Ag^+ + e^- \longrightarrow Ag \quad 1.29$$

$$h^+_{vb} + OH^- \longrightarrow {}^{\bullet}OH \quad 1.30$$

$${}^{\bullet}OH + dyes \longrightarrow Degradation\ Products \quad 1.31$$

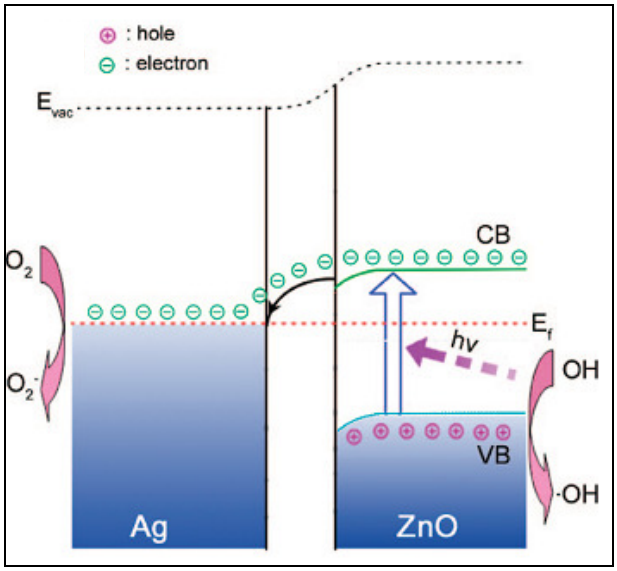

Figure 8. The proposed charge separation process and the photocatalytic mechanism of Ag/ZnO powders under UV irradiation

Source: Lu, *et al.,* (2008)

7. Review of Literatures

Tan, *et al.,* (2008) prepared Ag/ZnO photocatalyst by two-step method. Firstly, tetrapod-like ZnO (T-ZnO) was deposited by thermal evaporation after that Ag/T-ZnO also synthesized by RF magnetron sputtering method. The photocatalytic activity of the sample were investigated through degradation of methyl orange (MO) solution. The Ag/T-ZnO heterostructure exhibits better photocatalytic activity than that of the pure T-ZnO. The essential photocatalytic mechanism of this heterostructure have been discussed and the enhanced photocatalytic activity. The phtocatalytic reaction mechanism for this prepared photocatalyst was expressed by Eqs. 1.32–1.37. For proposed reaction process, Ag nanoparticles on the surface of T-ZnO act as a sink for the electrons (Eqs. (1.32) and (1.35)), promote the separation of photogenerated electron–hole pairs, and thus enhance the photocatalytic activity of Ag/T-ZnO photocatalysts.

$$Ag \rightarrow Ag^{+} + e^{-} \quad 1.32$$

$$e^{-} + O_2 \rightarrow O_2^{-} \quad 1.33$$

$$ZnO + h\nu \rightarrow e_{cb}^{-} + h_{vb}^{+} \quad 1.34$$

$$e_{cb}^{-} + Ag^{+} \rightarrow Ag \quad 1.35$$

$$h_{vb}^{+} + OH^{-} \rightarrow {}^{\bullet}OH \quad 1.36$$

$${}^{\bullet}OH\ (O_2^{-}) + MO \rightarrow \text{Photocatalytic products} \quad 1.37$$

Lu, *et al.,* (2008) investigated the effect of Ag contents on three-dimensional (3D) Ag/ZnO hollow microspheres through a facile one-pot hydrothermal method assisted by sodium alginate. The preparation of three-dimensional (3D) Ag/ZnO hollow microspheres is presented in Figure 9. Ag/ZnO prepared by this method was composed of metallic Ag and wurtzite ZnO that the 3D Ag/ZnO hollow microspheres were constructed from self-assembled 1D Ag/ZnO nanorods. The formation mechanism of the three-dimensional (3D) Ag/ZnO hollow microspheres is shown in Figure 10. This photocatalyst exhibits significantly enhanced photocatalytic efficiency through degradation of Orange G. Investigation of the relationship between

photoluminescence (PL) spectra and surface structure of the samples confirmed that the Ag deposits not only acted as electron sinks to enhance the separation of photoinduced electrons from holes, but also elevated the amount of the surface hydroxyl, leading to the formation of more hydroxyl radicals ($^{\bullet}OH$) and then the higher photodegradation efficiency.

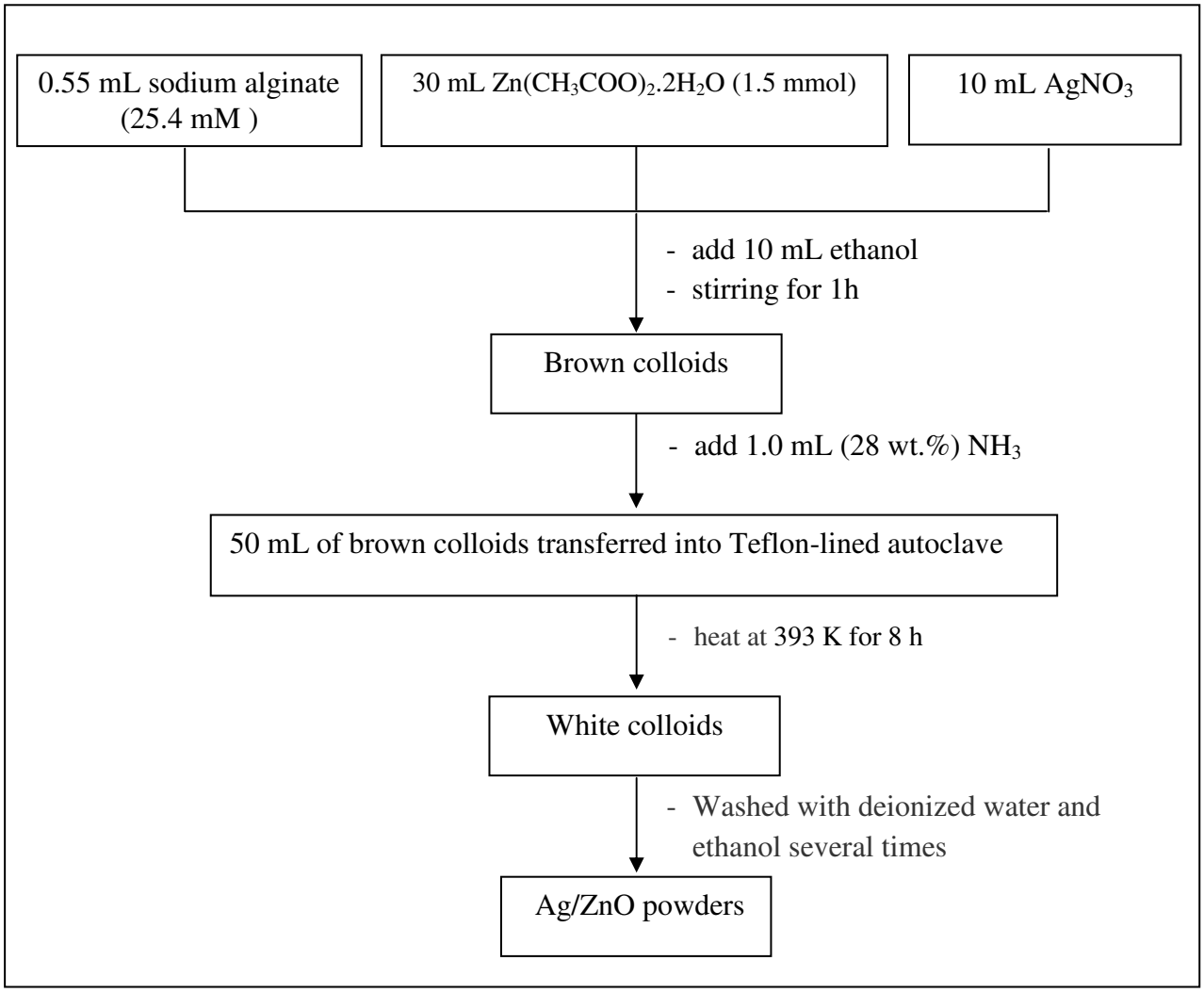

Figure 9. The flow chart shows the procedure for preparing Ag/ZnO hollow microspheres through hydrothermal method

Source: Lu, *et al.,* (2008)

$$Zn^{2+} + 4NH_3 \longrightarrow Zn(NH_3)_4^{2+} \quad 1.38$$

$$Ag^{+} + 2NH_3 \longrightarrow Ag(NH_3)_2^{+} \quad 1.39$$

$$NH_3 + H_2O \longrightarrow NH_4^{+} + OH^{-} \quad 1.40$$

$$Zn(NH_3)_4^{2+} + Ag(NH_3)_2^{+} + 8OH^{-} \longrightarrow Zn(OH)_4^{2-} +$$

$$2Ag(OH)_2^{-} + 8NH_3 \xrightarrow{\text{Co-dehydrolysis}} Ag_2O/ZnO \quad 1.41$$

$$Ag_2O/ZnO + \text{ethanol} \longrightarrow Ag/ZnO \quad 1.42$$

Figure 10.The formation mechanism of Ag/ZnO hollow microspheres through hydrothermal method

Song, *et al.,* (2010) used the facile low-temperature solution route to prepare radical-shaped ZnO microprisms and to deposit metallic silver on the surface of ZnO to form Ag/ZnO microstructures. The deposition of metal Ag nanospecies can be achieved successfully by simply aging the solution at 75 °C, and the radical-shaped microstructures of ZnO are well maintained. The Ag/ZnO microstructures exhibit much lower PL emission intensity and much higher photocatalytic activity through degradation of MO dye than those of radical-shaped ZnO microprisms.

Xie, *et al.,* (2009) prepared Ag/ZnO composite nanospheres with an average diameter of about 440 nm through a facile one-pot solvothermal reaction using a kind of biomolecular sodium alginate ($NaC_6H_7O_6$) as template. In a typical procedure, 1.8 mmol $Zn(C_2H_3O_2)_2 \cdot 2H_2O$, 0.2 mmol $AgNO_3$ and 100 mg $NaC_6H_7O_6$ were dissolved in 5 mL deionized water and 10 mL diethanolamine. The results showed that the as-made Ag/ZnO assembled nanospheres exhibited better photocatalytic performance than the pure ZnO nanoparticles and the formation mechanism of Ag/ZnO is shown in Figure 11.

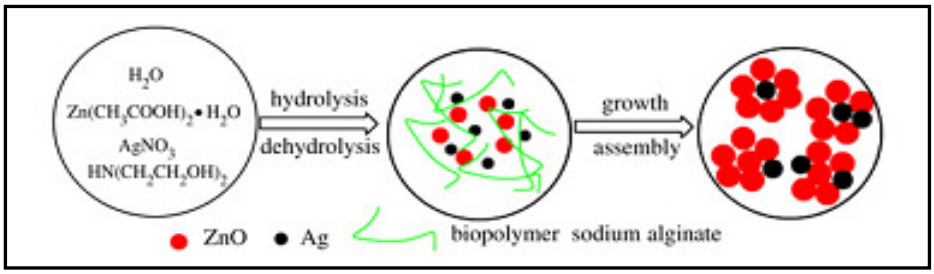

Figure 11.The schematic diagram of the formation mechanism of Ag/ZnO nanospheres.

Source: Xie, *et al.,* (2009)

Ren, *et al.,* (2010) prepared the silver-modified ZnO nanorods array and studied the effect of silver modification for photocatalytic efficiency of Ag/ZnO nanorods array. ZnO nanorods array were fabricated through a wet chemical route and a photo deposition method was taken to fabricate silver nanoparticulate on the ZnO nanorods as presented in Figure 12. The photocatalytic activity of these materials was studied by analyzing the degradation of methylene blue (MB) in aqueous solution under UV light. The photocatalytic performance indicated that Ag deposit acted as not only electron sinks to enhance the separation of photoexcited electrons from holes, but also charge carrier recombination centers, so the optimized amount of Ag deposit was investigated and it was found that the 0.37 at % Ag shows highest photocatalytic activity.

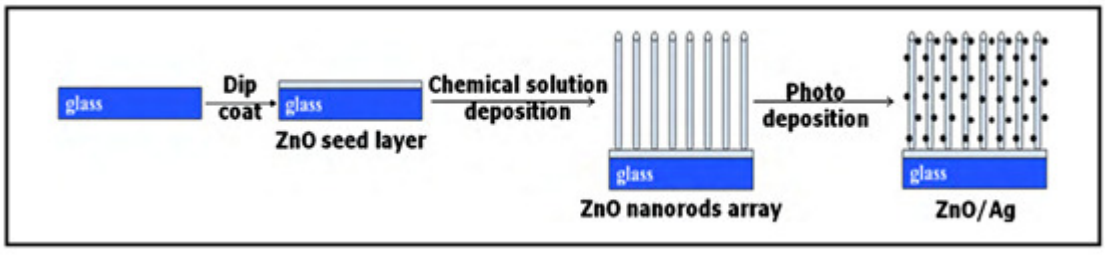

Figure 12.The schematic diagram of the formation mechanism of Ag/ZnO nanorods array through wet chemical route

Source: Ren, *et al.,* (2010)

Okorn, *et al.,* (2010) investigated the effects of synthesis conditions (i.e., metal concentration, precursor flowrate, and O_2 dispersion) during flame-spray pyrolysis (FSP) and annealing post-treatment on the characteristics and also studied the photocatalytic activities of ZnO nanoparticles. The average particle size of ZnO powder prepared by one-step FSP method were in the range of 8.8 - 47.0 nm and were found to be increased with increasing the enthalpy density, flame height, and high-temperature residence time during FSP synthesis. The larger particle size FSP-derived ZnO nanoparticles exhibited higher photocatalytic activities in the degradation of methylene blue (MB) dye. The degradation rate over FSP-ZnO-47.0 nm was 1.7 and 7.2 times higher than those of the commercially available photocatalysts Degussa P-25 and JRC-TiO_2, respectively. The better photocatalytic performance of the FSP-ZnO was correlated well with the improved crystalline quality of ZnO nanoparticles as revealed by the X-ray diffraction (XRD) and the photoluminescence (PL) results. This work also suggests a balance between high crystalline quality that enhanced photo-phenomena and the surface area available for substrate adsorption in order to obtain high photocatalytic activity of ZnO nanoparticles.

Wei, *et al.,* (2010) investigated the effect of Ag loading on ZnO photocatalyst preparing by reduction of Ag^+ on ZnO surface with ethanol as hole scavenger. The flow chart of prepared Ag/ZnO by this method was shown in Figure 13. Ag on ZnO not only enhances its photocatalytic activity but also improves its photostability. The metallic Ag in the Ag/ZnO photocatalysts does play a new role of O_2 chemisorption sites except for electron acceptor, by which chemisorbed molecular oxygen reacts with photogenerated electrons to form active oxygen species, and thus facilitates the trapping of photogenerated electrons and further improves the photocatalytic activity of the Ag/ZnO photocatalysts.

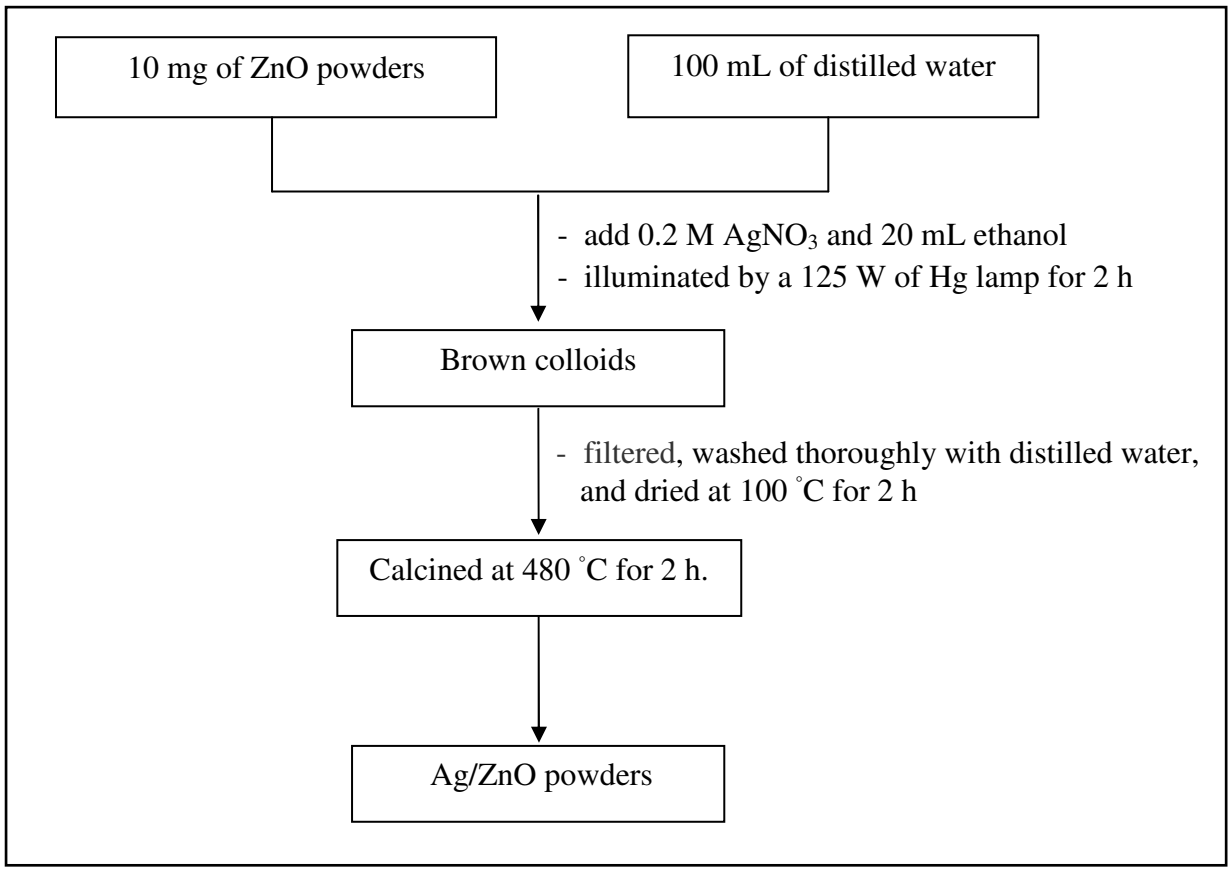

Figure 13. The flow chart shows the procedure for preparing Ag/ZnO through photocatalytic reduction method
Source: Wei, *et al.,* (2010)

Youlei, *et al.,* (2010) prepared the nanosheets-constructed ZnO spheres with novel three-dimensional (3D) fluffy structure by a facile one-step solvothermal method. Each fluffy ZnO sphere possesses a diameter of 2–3 μm, consisting of crossed nanosheets with an average thickness of ~20 nm. The prepared special hollow 3D structure makes larger surface area and more active sites exposed during the reaction, facilitating the transportation of reactants and products and increasing the reaction rate. The activity measurement for rhodamine B photodegradation shows that such fluffy ZnO spheres do possess much higher photocatalytic activity than other commonly reported nanostructured ZnO, such as nanoflowers, nanospiraldisks, nanodumbbells and nanorods. The results of photoluminescence spectra show that the fluffy spheres show much higher electron–hole segregation efficiency than other ZnO

materials. The growth mechanism for fluffy ZnO spheres is proposed as shown in Figure 14.

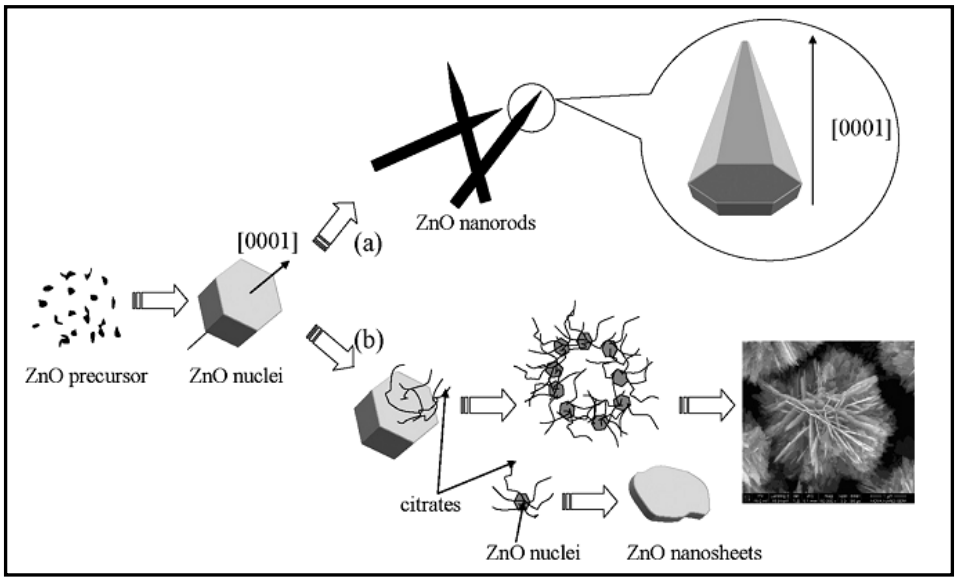

Figure 14. (a) ZnO grows along the [0001] crystal axis and (b) a potential mechanism for the formation of the fluffy ZnO sphere
Source: Youlei, *et al.,* (2010)

Karunakaran *et al.,* (2011) prepared nanocrystalline ZnO and Ag-ZnO (0.1 at%) by sol–gel method. Doping ZnO with Ag reduces the average crystal size, sharpens the band gap absorption and decreases the charge-transfer resistance. The bactericidal and photocatalytic activities of sol–gel synthesized ZnO were tested with inhibiting of *Escherichia coli* growth and degrading of cyanide ion. Furthermore, this photocatalyst also enhances photocatalytic degradation for methylene blue, methyl orange and rhodamine B dyes solutions.

Zhang, *et al.,* (2011) prepared the Ag nanoparticles stabilized ZnO nanosheets using a liquid–liquid two-phase method with (n-Dodecyl)trimethylammonium bromide (DTAB) as a phase transfer agent at the room temperature. The flow chart of this preparation method is shown in Figure 15. The silver nanoparticles which are conductors with the character of attracting energy can make the ZnO sheets stabilize under the higher energy electrons. The results demonstrate that the silver nanoparticles load on the surface of ZnO sheets and make the ZnO sheets stabilize.

The photocatalytic activities of the pure ZnO and Ag/ZnO nanosheets were evaluated by the degradation of methyl orange (MO) dye under UV irradiation.

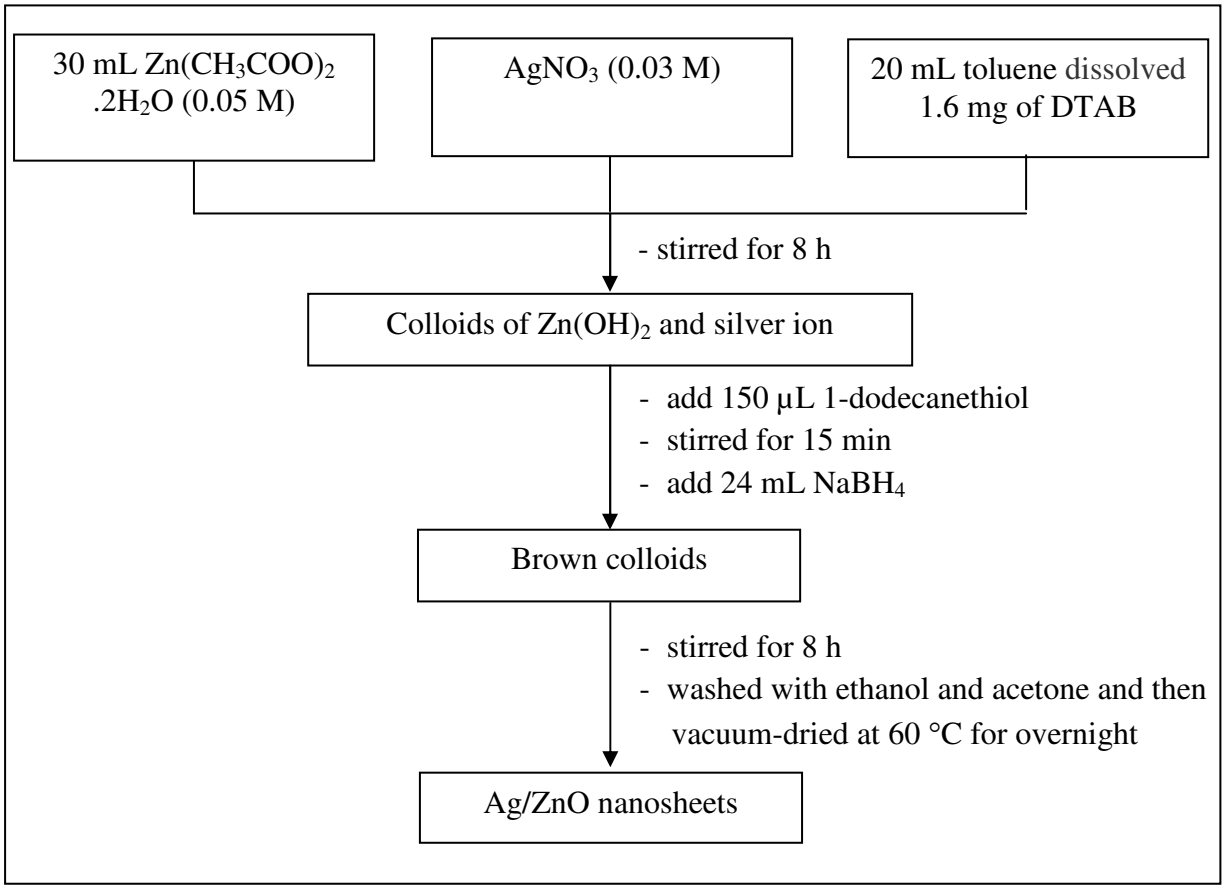

Figure 15. The flow chart for preparation of Ag/ZnO nanosheets by liquid–liquid two-phase method

Source: Zhang, *et al.,* (2011)

Fu, *et al.,* (2011) prepared the nanosized zinc oxide graphene oxide (ZnO-GO) by using GO dispersed in the ethanol as carrier, zinc acetate dihydrate and lithium hydroxide monohydrate as reactant. The nanosized hybrid material of ZnO-graphene (ZnO-G) is obtained by thermally treating ZnO-GO at different temperatures. The results reveal that both sides of the graphene sheets are coated with ZnO particles, and that the lattice constants and the band gap energy of ZnO have been changed compared with the pure nano-sized ZnO particles. The photocatalytic activity was tested with degradation of methylene blue (MB) and the results showed that ZnO-G prepared at 200 °C containing 2.5% graphene exhibits the highest activity which is

higher than 3 times comparing with pure ZnO. The optimum ZnO-G catalyst still retains the 80% of the initial activity still after it has been used 5 times repeatedly, and exhibits larger rate for MB degradation than pure ZnO in each recycled time.

JIA Zhi, *et al.,* (2011) prepared the porous silver-modified ZnO microrods photocatalysts through direct thermal decomposition of the Ag-doped zinctartrate precursor, which was prepared by homogeneous precipitation method at 80 °C for 2 h. The photocatalytic activity of the as-prepared porous Ag/ZnO microrods was tested with the photocatalytic degradation of methyl orange (MO). The results indicate that doping Ag greatly improves the photocatalytic efficiency of ZnO and 3% Ag-doped ZnO porous microrod photocatalyst exhibits the highest photocatalytic decolorization efficiency. It can degrad the MO more than 80 % in 120 min. Moreover, the 3% Ag-doped porous microrods also possess higher photocatalytic activity under the real sunlight irradiation.

Hung, *et al.,* (2011) immobilized photocatalyst by the growth of ZnO nanograss on the ZnO pore-array substrate. Nanograss decorated ZnO pore-array films exhibited improved performance on the photocatalytic degradation of methyl orange (MO) in aqueous solution under UV illumination. The enhanced photocatalytic activity of the nanostructured pore-array photocatalyst can be attributed to increase active surface area, improve diffusion of dye molecules among the nanostructured catalyst, and enhance light absorption through the light-trapping effect.

Whang, *et al.,* (2011) prepared the Ag doped ZnO nanoparticles through the laser-induction method. The method of preparation is shown in Figure 16. The Ag contents in Ag/ZnO attained by varying the added $AgNO_3$ concentrations. The photocatalytic activity of this photocatalyst was investigated by photocatalytic degradation of methylene blue (MB) solution under visible light illumination. The results showed that it has a maximum effectiveness of 92% degradation after 8 h illumination.

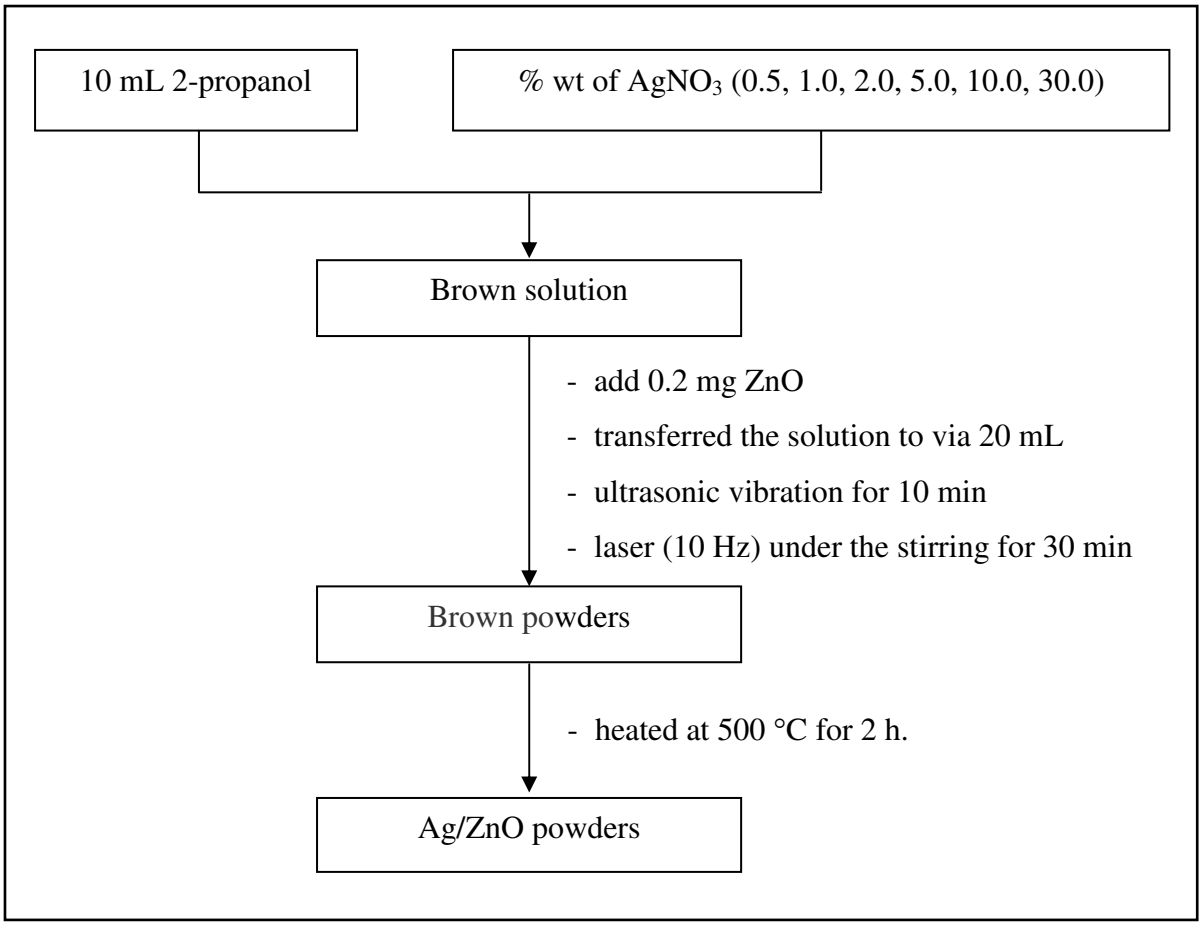

Figure 16.The flow chart for preparation of Ag/ZnO by laser-induction method
Source:Whang, *et al.,* (2011)

Wang, *et al.,* (2011) reported the successfully photodeposition method to synthesize Ag/tetrapod-like ZnO whisker (T-ZnOw) nanoparticles. The flow chart for preparation of Ag/ T-ZnOw is shown in Figure 17. All prepared Ag/T-ZnOw nanocompounds showed a photocatalyst property and their activities with increasing of polyethylene glycol (PEG) contents. PEG can reduce Ag^{+} into Ag under UV irradiation, which can be subsequently deposited on the surface of T-ZnOw as nanoparticles. And then the photocatalytic activities of the samples were determined by measuring the photodegradation of methyl orange (MO) solution. Ag/ T-ZnOw show the photoefficiency higher than T-ZnOw.

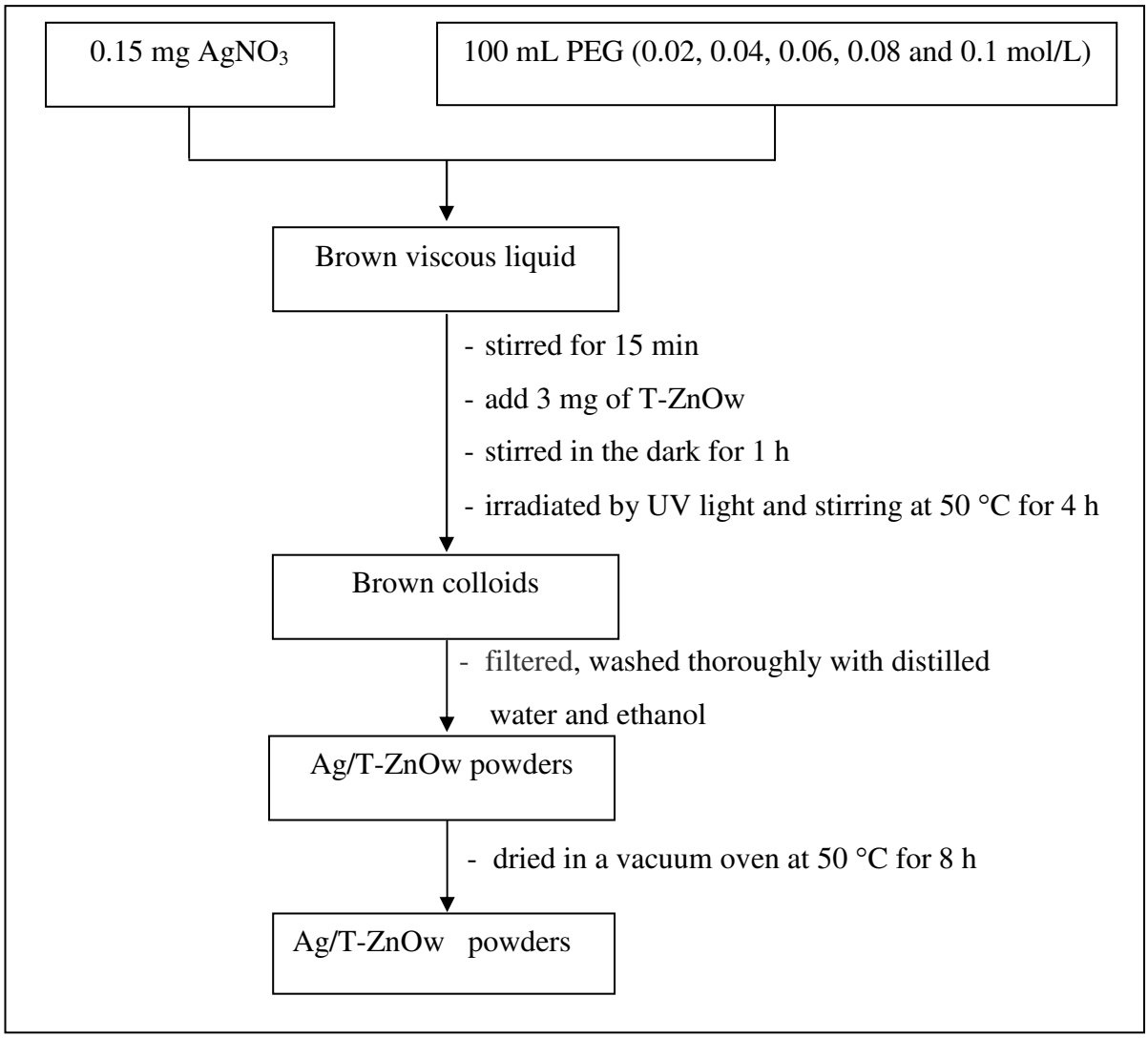

Figure 17.The flow chart for preparation of Ag/tetrapod-like ZnO whisker (T-ZnOw) through photodeposition method
Source: Wang, *et al.,* (2011)

Li, *et al.,* (2011) prepared the large number of zinc oxide (ZnO) nano-needles by thermal oxidation of pure zinc. The synthesized ZnO nano-needles were close-packed hexagonal structure, which showed needle-like morphology. Their average diameter is about 40 nm, lengths up to 5 μm. The surfaces of ZnO nano-needles were coated with a layer of Ag by pulse electro-deposition technique. The photoluminescence spectrums of uncoated ZnO nano-needles showed two fluorescence peaks at 388 nm and 470.8 nm with the relative intensity of 143.4 and 93.61, respectively. However, the Ag coated ZnO nano-needles have a pair of strong

peaks at 387.4 nm and 405.2 nm, the relative intensity of 1366 and 1305, respectively, This indicate that the Ag-coated ZnO nano-needles can increase the absorption of UV light.

Yang, *et al.,* (2011) synthesized Ag/ZnO heterostructures through a UV irradiation as shown in Figure 18. The effect of Ag loading on photocatalytic performance was studied by changing the Ag contents between 3.0 and 15.0 at.%. The formation of Ag/ZnO heterostructures depends on photogenerated electrons produced by ZnO under UV irradiation to reduce high valence silver. The photocatalytic activity of the Ag/ZnO heterostructures is evaluated by photodegradation of methylene blue (MB) under UV illumination. For Ag loading of 5.0 at.%, it is shown the best photocatalyst activity higher than the pure ZnO synthesized in the same condition. The photocorrosion process can be roughly expressed as follows:

$$ZnO + 2h^{+} \longrightarrow Zn^{2+} + 1/2O_2 \qquad 1.43$$

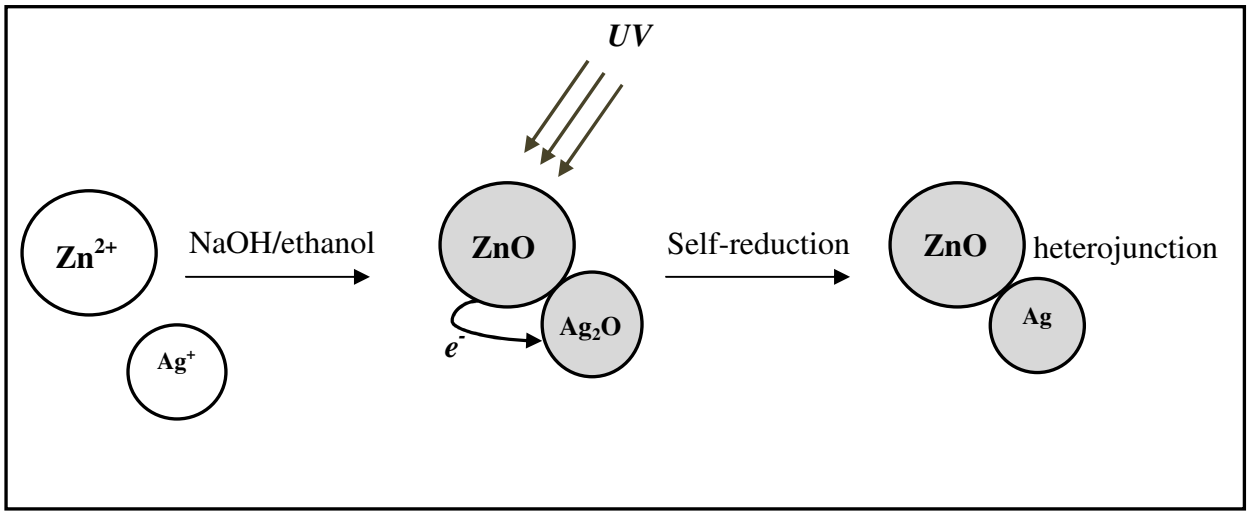

Figure 18. The schematic diagram of the formation mechanism of Ag/ZnO through by UV irradiation method

Source:Yang, *et al.,* (2011)

8. Research objective

1. To prepare ZnO powders from different flow rates of mixing precursor solution by precipitation method
2. To prepare Ag/ZnO powders at different Ag contents by precipitation method
3. To characterize some physical properties of ZnO and Ag/ZnO powders
4. To investigate the photocatalytic activity of ZnO and Ag/ZnO powders

CHAPTER 2

EXPERIMENTAL METHOD

1. Chemicals and Reagents

Chemicals and reagents used in this work were purchased from various suppliers as shown in Table 4 and they were used as received.

Table 4. List of chemicals and reagents

Chemicals and reagents	Suppliers
Zinc acetate dihydrate ($Zn(C_2H_3O_2)_2$, AR grade	Sigma-Aldrich, Germany.
Sodium hydroxide (NaOH), AR grade	Merck, Germany.
Silver nitrate ($AgNO_3$), AR grade	Merck, Germany.
Methylene blue ($C_{16}H_{18}N_3ClS.2H_2O$), AR grade	UNILAB, Australia
Reactive Orange 16 ($C_{20}H_{19}N_3O_{11}S_3.2Na$, AR grade	Sigma-Aldrich, Germany.
Rhodamine B ($C_{28}H_{31}ClN_2O_3$) , AR grade	Sigma-Aldrich, Germany.

2. Instruments and Equipments

1. X-ray diffractometer, XRD, PHILIPS X'Pert MPD, Netherlands
2. Scanning electron microscope, SEM, Quanta 400, FEI
3. UV-Visible Diffuse reflectance spectroscopy (DRS), UV- 2450,Shimadzu Japan
4. UV- Visible Spectrometer, Lambda 45, PerkinElmer, United stated
5. Oven, Memmert oven. UNB 400
6. Analytical balance, Mettler Toledo. PL403 Precision Balance
7. Centrifuge; EBA 20, Hettich, Germany
8. Magnetic stirrer, Jenway 1000, JENWAY,UK
9. Wooden compartment (40cm × 70cm × 40cm) with three tubes of 18 watts blacklight, Sylvania

3. Methods

This work can be divided into 2 parts; (1) preparation and characterization of pure ZnO and Ag/ZnO by precipitation method, and (2) studies of photocatalytic property with various parameters under UV source (blacklight 18 watts). The products were then characterized by various techniques such as X-ray powder diffractometry (XRD), scanning electron microscope (SEM) and diffused reflectance UV-VIS spectrophotometry.

3.1 Preparation of pure ZnO and Ag/ZnO powders

3.1.1 Synthesis of pure ZnO

ZnO powders were synthesized through a precipitation method. Zinc acetate dihydrate, $Zn(C_2H_3O_2)_2.2H_2O$, 0.01 M (2.1950 g) was dissolved in 150 mL of distilled water and then 150 mL of 0.1 M NaOH (4.000 g) solution was added with various mixing rates of 2.5, 5 and 30 mL/s and then these solutions were heated at 80 ^oC for 1 h. The precipitates were separated and then washed with water three times. Finally, the white powders were dried at 100 ^oC for 1 h. The flow chart is illustrated in Figure 19.

3.1.2 Synthesis of Ag/ZnO

Ag/ZnO powders were prepared by a precipitation reaction in two methods:

Method 1, the required amounts of $AgNO_3$ were added into Zn^{2+} solution and stirred to obtain mole ratios of Ag^+: Zn^{2+} = 0.5, 1, 3, 5, 7, 9 and 13 mole %, respectively. Then, 0.1 M NaOH was added into the above solution at mixing rate of 30 mL/s. The mixture was then heated at 80 ^oC for 1 h. After that the brown precipitants were separated and then washed with water three times. Finally, the brown powders were dried at 100 ^oC for 1 h. The step for synthesizing Ag/ZnO by Method 1 is presented in Figure 20.

Method 2, 0.1 M NaOH was added into the Zn^{2+} solution with a mixing rate of 30 mL/s. The Ag^{+} solution was added drop-wise to the above solution and then heated at 80 ^{o}C for 1 h. These precipitants were separated and then washed with water for three times. Finally, the brown powders were dried at 100 ^{o}C for 1 h. Figure 21 shows the schematic represented to synthesize Ag/ZnO powders by Method 2.

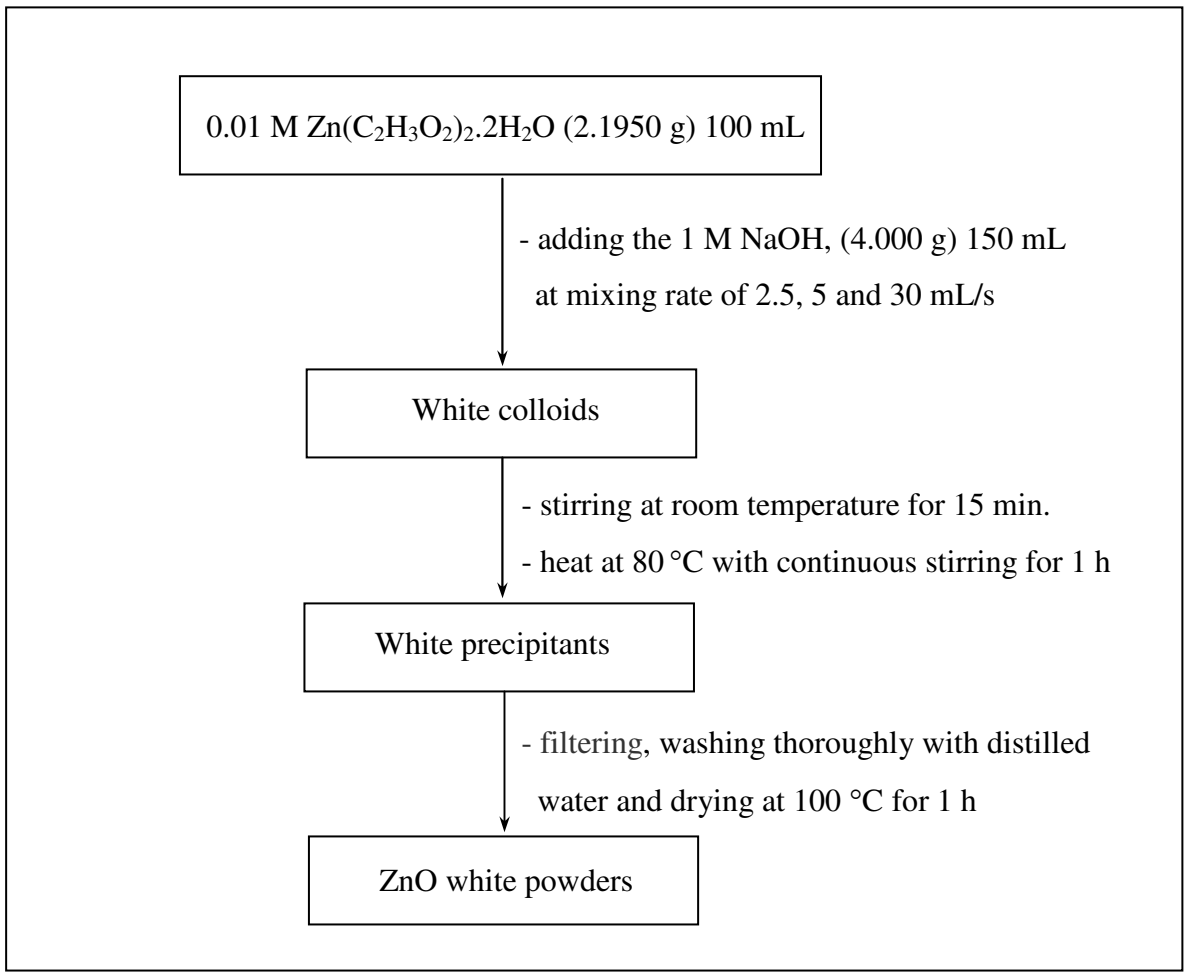

Figure 19. Flow chart of the preparation of pure ZnO powder by precipitation method

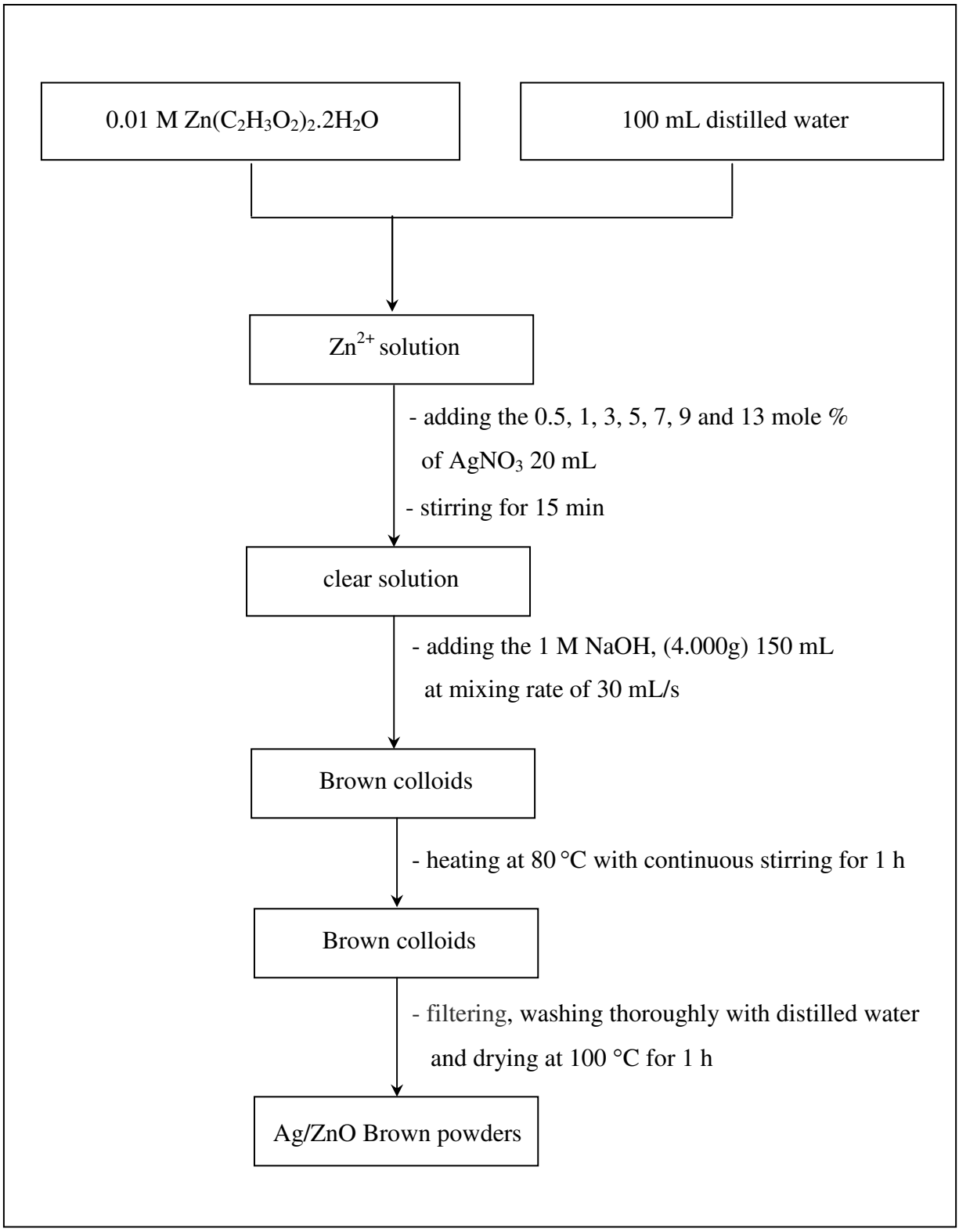

Figure 20. Flow chart of the preparation of Ag/ZnO powder by precipitation method by Method 1

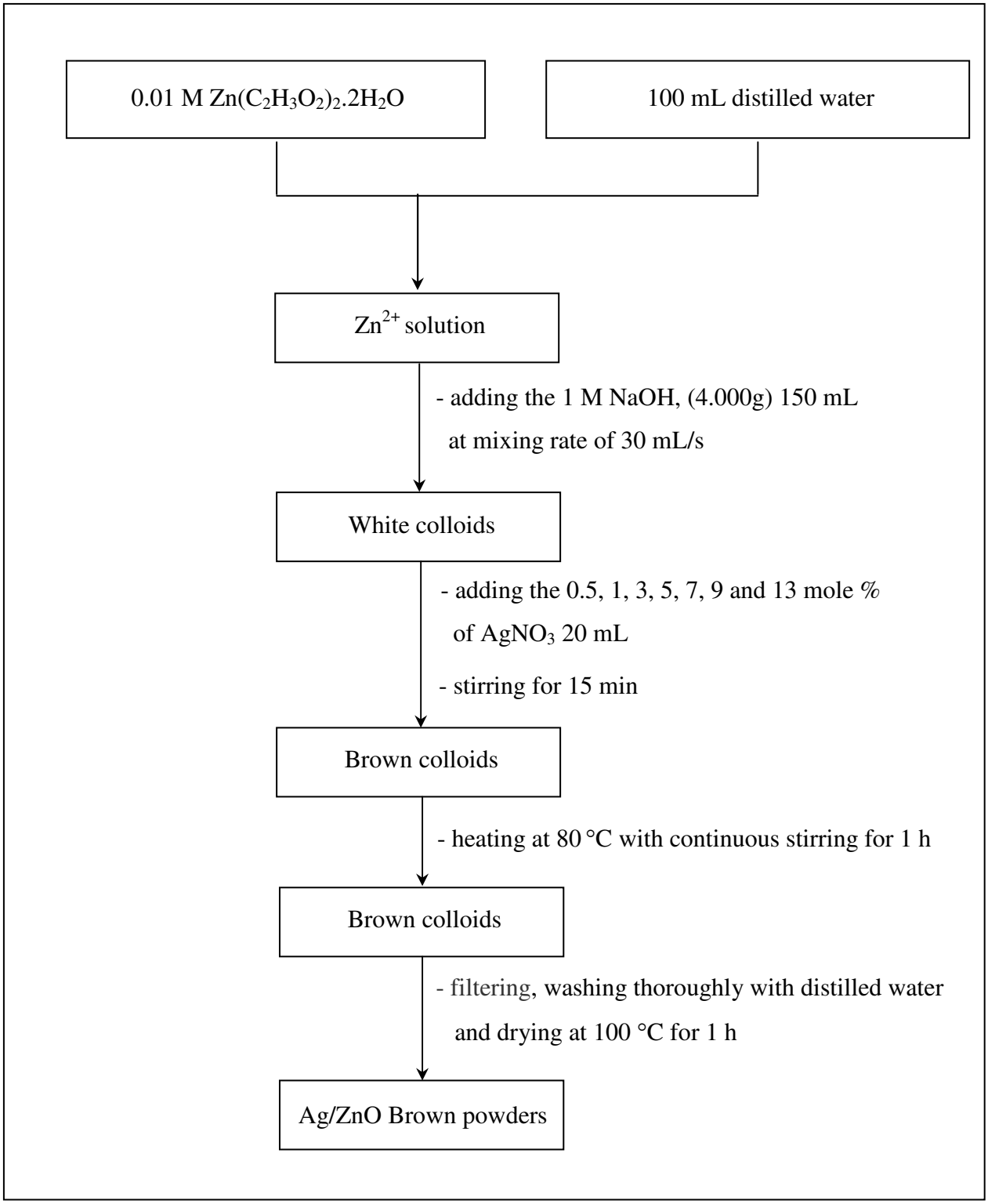

Figure 21. Flow chart of the preparation of Ag/ZnO powder by precipitation method by Method 2

3.2 Characterization techniques for undoped ZnO and Ag-doped ZnO powder

3.2.1 X-ray powder diffractometry (XRD)

X-ray diffraction (XRD) is a non-destructive technique primarily used for phase identification of a crystalline material and this technique also provides information on unit cell dimensions. When X-ray interacts with a crystalline phase, a diffraction pattern is generated as a result of the interaction between the incident X-ray beam and the atomic architecture of the crystalline solid.

X-ray is an electromanetic wave which have wavelengths in the Angstrom rang. It has sufficiently energetic to penetrate solid and is well suited to probe their internal structure. XRD is used to identify bulk phases, to monitor the kinetics of bulk transformations and to estimate particle sizes. The X-ray wavelength commonly employed is the characteristic K_α radiation, λ = 1.5418 Å, emitted by copper target. When crystal diffract X-ray, it is the atom or ions which act as secondary point sources and scatter the X-ray; in the optical grating, it is the lines scratched or ruled on the glass surface which cause scattering.

The diffraction phenomina can be simpify described by Bragg's law as presented in Eq. 3.1. The Bragg approach to diffraction is to regard crystals as built up in layers or planes such that each acts as a semi-transparent mirror. Some of the X-rays are reflected off a plane with the angle of reflection equal to the angle of incidence, but the rest are transmitted to be subsequently by succeeding planes.

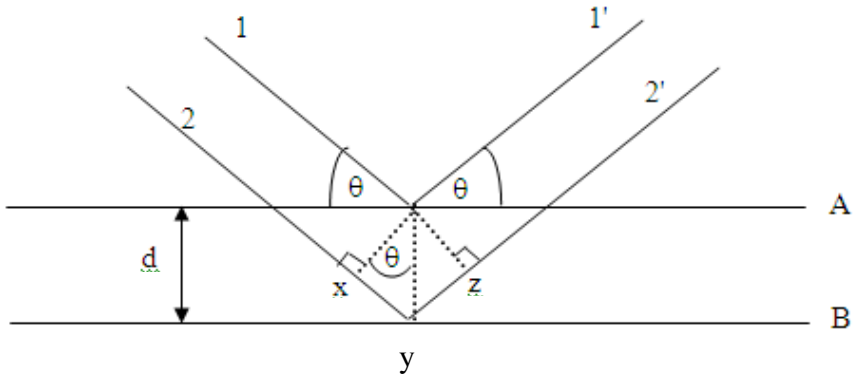

Figure 22. Derivation of Bragg's Law for X-ray diffraction

The derivation of Bragg's Law is show in Figure 22. Two X-ray beams, 1 and 2, are reflected from adjacent planes, A and B, within the crystal and would like to know what conditions the reflected beam 1′ and 2′ are in phase. Beam 22′ has to travel the extra distance *xyz* as compared to beam 11′, and for 1′ and 2′ to be in phase, distance *xyz* must equal a whole number of wavelengths. The perpendicular distance between pairs of adjacent planes, the *d-spacing, d,* and the angle of incidence, or *Bragg angle,* θ, are related to the distance *xy* by

$$xy = yz = d \sin\theta$$

thus

$$xyz = 2d \sin\theta$$

but

$$xyz = n\lambda$$

therefore

$$2d \sin \theta = n\lambda \qquad (n = 1, 2, 3, \ldots) \qquad 3.1$$

The XRD pattern of a powdered sample is measured with a stationary X-ray source and a movable detector, which scans the intensity of the diffracted radiation as a function of the angle 2θ between the incoming and the diffracted beams. When working with powdered samples, and image of diffraction lines occurs because a small fraction of the powder particles will be oriented such that by chance a certain

crystal plane is at the right angle θ with the incident beam for constructive interference, as shown in Figure 23. The angles of maximum intensity enble one to calculate the spacings between the lattice planes and allow for phase identification. Diffractograms are measured as a function of the angle 2θ. When the sample is a polycrystalline powder, the diffraction pattern is formed by a small fraction of the particle only. Rotation of the sample during measurement enhances the number of particles that contribute to diffraction.

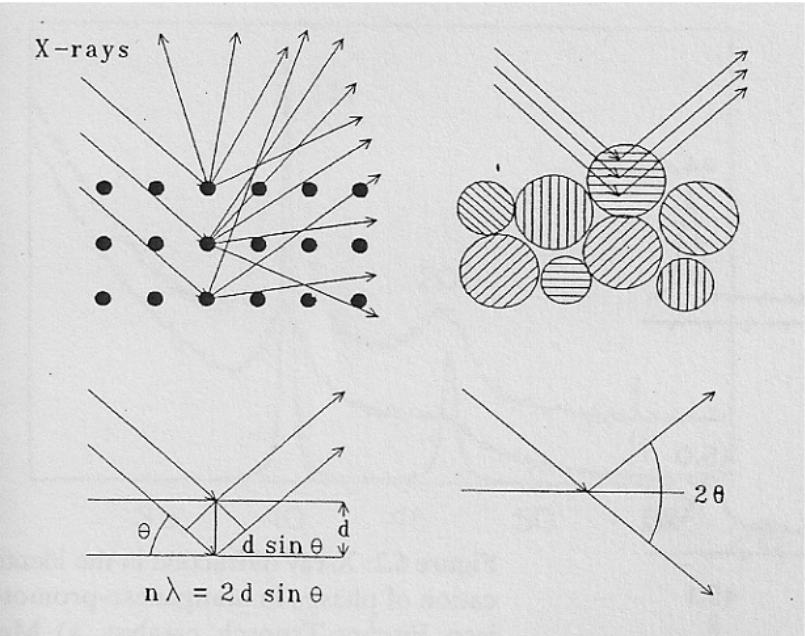

Figure 23. X-ray scattered by atom in an ordered lattice interfere constructively in directions given by Bragg's Law
Source: Niemantsverdriet (1993).

X-ray diffraction has an important limitation: clear diffraction peaks are only observed when the sample possesses sufficient long range order. The advanctage of this limitation is that the width of diffraction peaks carries information on the dimensions of the reflecting planes. Diffraction lines from perfect crystals are very narrow. For crystallite size below 100 nm, the linebroadening occurs due to incomplete destructive in scattering directions where the X-ray are out of phase. The crystallite size can be calculated by line width as well known as Scherrer's equation:

$$D = \frac{0.9\lambda}{\beta \cos\theta} \qquad 3.2$$

where D is the average crystallite size, λ is the wavelength of incident X-ray, θ is the Bragg angle of diffraction lines, β is the full-width half-maximum in radians. However, amorphous phases and small perticles give either broad and weak diffraction lines or no diffraction at all, with the consequence that if catalysts contain particles with a size distribution, XRD may only detect the larger ones.

Schematic of X-ray

X-ray diffractometers consist of three basic elements: an X-ray tube, a sample holder, and an X-ray detector. X-rays are generated in a cathode ray tube by heating a filament (cathode) to produce electrons, accelerating the electrons toward a target by applying a voltage (normally in order of 30 kV to 50 kV), and bombarding the target material (anode) with electrons (Figure 24). When electrons have sufficient energy to dislodge inner shell electrons of the target material, characteristic X-ray spectra are produced (Figure 25 (a)). These spectra consist of several components, the most common being K_α and K_β (Figure 25 (b)).

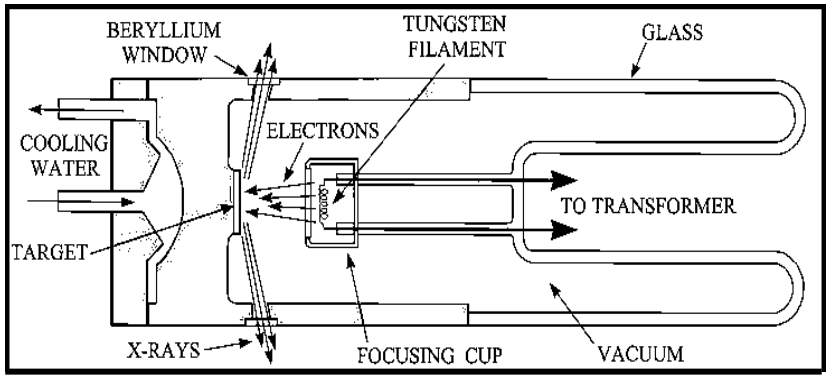

Figure 24. Schematic cross section of an X-ray tube

Source: http://pubs.usgs.gov/of/2001/of01-041/htmldocs/images/xrdtube.jpg

K_α consists, in part, of $K_{\alpha1}$ and $K_{\alpha2}$. $K_{\alpha1}$ has a slightly shorter wavelength and twice the intensity as $K_{\alpha2}$ (Figure 25(c)). Copper is the most common target material for single-crystal diffraction, with Cu K_α radiation = 1.5418 Å. Filtering, by foils or crystal monochrometers, is required to produce monochromatic X-rays needed for diffraction. $K_{\alpha1}$ and $K_{\alpha2}$ are sufficiently close in wavelength such that a weighted average of the two is used. After producing from X-ray tube, X-rays are collimated and directed onto the sample. As the sample and detector are rotated, the intensity of the reflected X-rays is recorded. When the geometry of the incident X-rays impinging the sample satisfies the Bragg equation, constructive interference occurs and a peak intensity occurs. A detector records and processes this X-ray signal and converts the signal to a count rate which is then output to a device such as a printer or computer monitor**.**

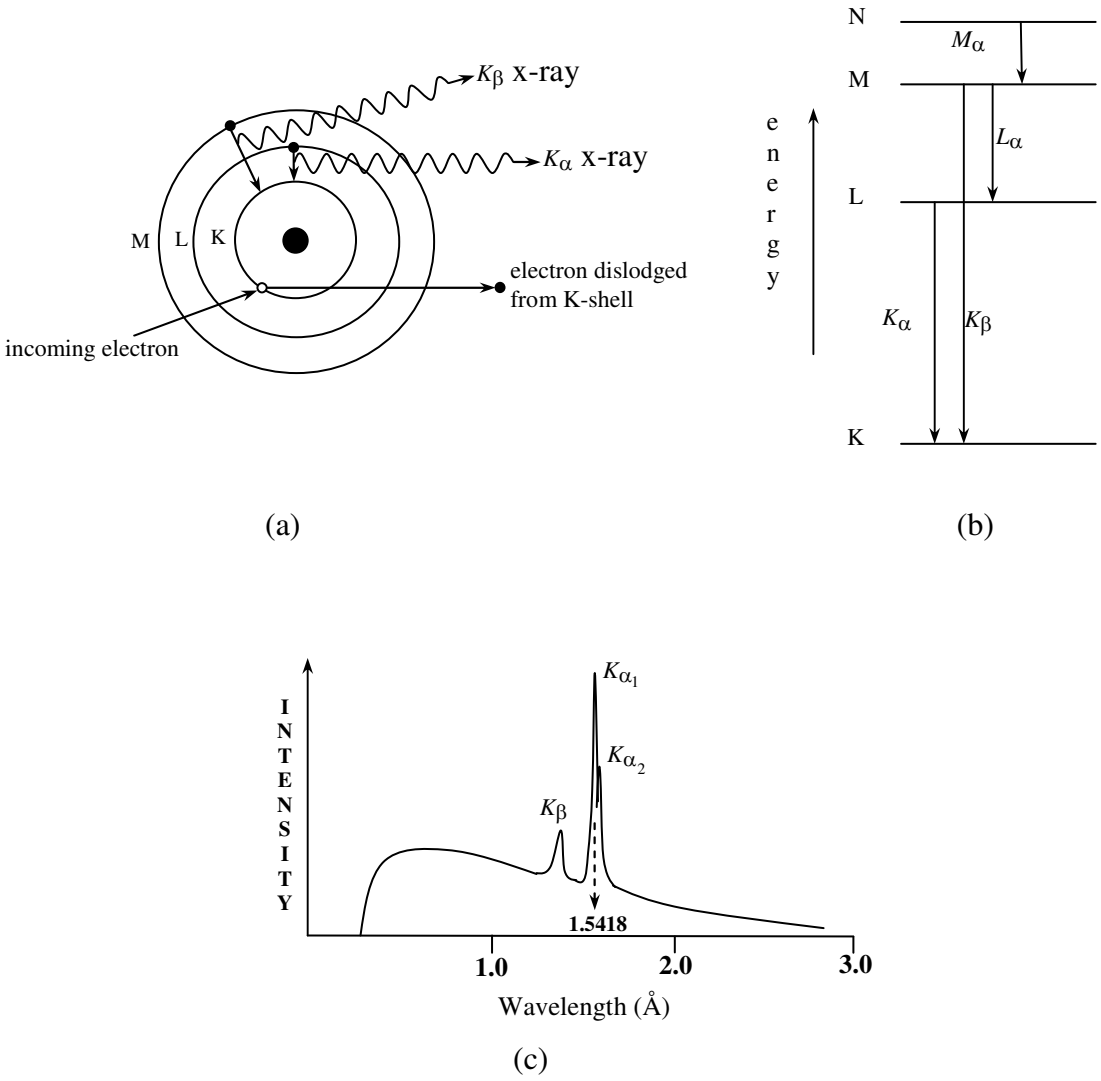

Figure 25. (a) shows schematically in the diagram. An incoming electron displaces a K-shell electron. If an L-shell electron moves to replace it, a K_α X-ray is produced. If an M-shell electron moves to replace it, a K_β X-ray is produced. (b) shows energy-level diagram for an atom illustrating the excitation of the K, L, M and N shells and the formation of K_α, K_β, L_α and M_α X-rays, and (c) shows that an X-ray spectrum consist of two different radiation continuous and characteristic radiation for copper.

The geometry of an X-ray diffractometer is such that the sample rotates in the path of the collimated X-ray beam at an angle θ while the X-ray detector is mounted on an arm to collect the diffracted X-rays and rotates at an angle of 2θ. The instrument used to maintain the angle and rotate the sample is termed a goniometer. This arrangement is called the Bragg-Brentano parafocusing geometry (Figure 26) and data is collected at 2θ.

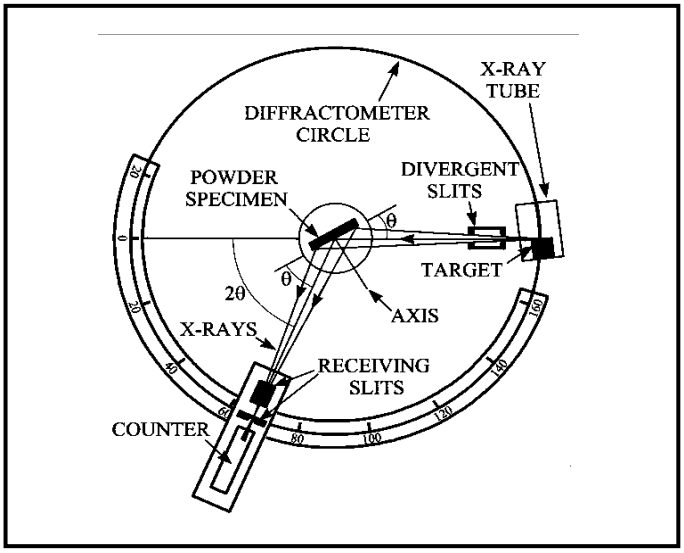

Figure 26. Geometric arrangement of the Bragg Brentano diffractometer
Source: http://pubs.usgs.gov/of/2001/of01-041/htmldocs/images/xrdschem.jpg

From the wurtzite structure, the interplanar distance of {*hkl*} plane is related to the lattice parameters *a* and *c* via the Miller indices *hkl*:

$$\left[\frac{1}{d_{hkl}}\right]^2 - \frac{4}{3}\left[\frac{h^2 + k^2 + hk}{a^2}\right] + \frac{l^2}{c^2} \qquad 3.3$$

It is well-known that the XRD technique provides the information on lattice parameter. If Miller indices can be assigned to the various reflections in the powder pattern, it becomes possible to determine the cell constant. These are directly related to 2θ and *h, k, l* through the relationships derived from the combination of Bragg's law and *d*-spacing expession and summarized in the Table 5.

Table 5. Expression for *d*-spacing in the different crystal systems

Crystal System	Expression for d_{hkl} terms of lattice parameters and Miller indices
Cubic	$\frac{1}{d^2} = \frac{h^2 + k^2 + l^2}{a^2}$
Tetragonal	$\frac{1}{d^2} = \frac{h^2 + k^2}{a^2} + \frac{l^2}{c^2}$
Orthorhombic	$\frac{1}{d^2} = \frac{h^2}{a^2} + \frac{k^2}{c^2} + \frac{l^2}{d^2}$
Hexagonal	$\frac{1}{d^2} = \frac{4}{3}\left[\frac{h^2 + k^2 + hk}{a^2}\right] + \frac{l^2}{c^2}$
Monoclinic	$\frac{1}{d^2} = \frac{1}{\sin^2\beta}\left[\frac{h^2}{a^2} + \frac{k^2 \sin^2\beta}{b^2} + \frac{l^2}{c^2} - \frac{2hl\cos\beta}{ac}\right]$

Source: Hammond (1990).

Sample preparation in XRD

XRD samples should be well-ground in a mortar and pestle or a ball mill. This creates a uniform particle size and ensures that all possible crystallite orientations are present in the sample. The well-fine sample is then mounted into the samples holder. Sample's requirement for powder XRD depends on the nature of the material. A typical sample holder makes of an aluminum plate with a circle hole in the center. Normally, the sample holder is a 20 mm of diameter and a 2 mm thick. It can be modified when the sample quantity is a problem. For materials that diffract strongly (many inorganic materials), a few milligrams of the sample is then spread on the tape and smoothed flat. The tape is primarily amorphous and so does not generally interfere with the pattern being collected.

3.2.2 Scanning Electron Microscope

SEM is a type of electron microscope that images the sample surface by scanning it with a high-energy beam of electron in a raster scan pattern. The electron interact with the atom that make up the sample producing signals that contain information about the sample's surface topography, composition and other properties such as electrical conductivity.

The types of signals produced by an SEM include secondary electron (SE), back scattered electron (BSE), characteristic x-rays, light (cathodoluminescence), specimen current and transmitted electrons. These types of signal all require specialized detectors for their detection that are not usually all present on a single machine. The signals result from interactions of the electron beam with atom at or near the surface of the sample. In the most common or standaed detection mode, secondary electron imaging or SEI, the SEM can produce very hight resolution images of a sample surface, revealing details about 1 to 5 nm in size. Due to the way these images are created, SEM micrographs have a very large depth of field yielding a characteristic three-dimensional appearance useful for underatanding the surface structure of a sample. A wide range of magnification is possible, from about x 25 (about equivalent to that of a powerful hand-lens) to about x 250,000, about 250 times the magnification limit of the best light microscopes (http://en.wikipedia.org/wiki/Scanning_ electron_microscope).

All samples must also be of an appropriate size to fit in the specimen chamber and are generally mounted rigidly on a specimen holder called a specimen stub. Several models of SEM can examine any part of a 6-inch (15 cm) semiconductor wafer, and some can tilt an object of that size to 45 degrees. For conventional imaging in the SEM, specimens must be electrically conductive, at least at the surface, and electrically grounded to prevent the accumulation of electrostatic charge at the surface. Metal objects require little special preparation for SEM except for cleaning and mounting on a specimen stub. Nonconductive specimens tend to charge when scanned by the electron beam, and especially in secondary electron imaging mode, this causes scanning faults and other image artifacts. They are therefore usually

coated with an ultrathin coating of electrically-conducting material, commonly gold, deposited on the sample either by low vacuum sputter coating or by high vacuum evaporation. Conductive materials in current use for specimen coating include gold, gold/palladium alloy, platinum, osmium, iridium, tungsten, chromium and graphite. Coating prevents the accumulation of static electric charge on the specimen during electron irradiation.

3.2.3. UV-Vis diffuse reflectance spectroscopy

Source: Wyszecki, G. and Stiles, W.S. (1982). Color Science : Concepts and Methods, Quantitative Data and Formulae (2 nd ed.). Canada, NJ : John Wiley & Sons.

The optical phenomenon known as diffuse reflectance is commonly used in the UV-visible, near-infrared (NIR), and mid-infrared regions to obtain molecular spectroscopic information. It is usually used to obtain spectra of powder by the collection and analysis of surface-reflected electromagnetic radiation as a function of frequency. There are two different type of reflection: regular or specular reflection usually associated with reflection from smooth, polished surface like mirrors, and diffuse reflection associated with reflection from so-called mat or dull surface texture like powders.

Originally published in the 1930s by Paul Kubelka and Franz Munk, the Kubelka-Munk equations described the reflectance and transmittance of the sample as a function of the absorption and scatter (*K* and *S*, respectively). In this Kubelka-Munk theory, the incident and scattered light flux are approximated by two fluxes *I* and *J*, which are perpendicular to the surface of the powdered sample, but in opposite direction as shown in Figure 27.

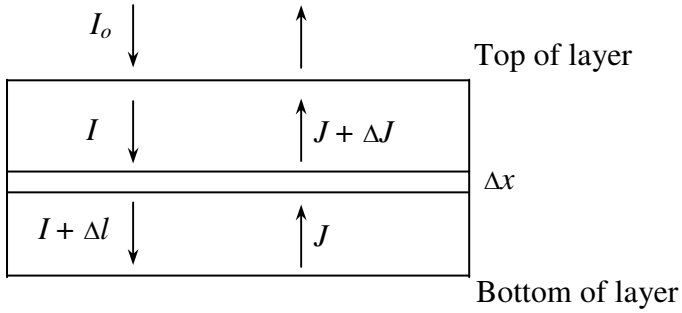

Figure 27. The Kubelka-Munk approximation: the incident and remitted light fluxes are approximated by two opposite fluxes, perpendicular to the surface of the infinitely thick sample layer.

Originally published in the 1930s by Paul Kubelka and Franz Munk, the Kubelka-Munk equations described the reflectance and transmittance of the sample as a function of the absorption and scatter (*K* and *S*, respectively). In this Kubelka-Munk theory, the incident and scattered light flux are approximated by two fluxes *I* and *J*, which are perpendicular to the surface of the powdered sample, but in opposite direction as shown in Figure.

In transmission spectroscopy, where a beam of light is passed through a sample, the transmittance is the ratio of intensities of transmitted to incident light:

$$T = I / I_o \qquad 3.4$$

where T is the transmittance, I is the intensity of transmitted light and I_o is the intensity of the incident beam. In an analogous fashion the remittance of a diffusely reflecting sample is the ratio of intensities of reflected to incident light:

$$R_\alpha = J / I_o \qquad 3.5$$

where R_α is the absolute remittance, J is the intensity of the reflected radiation, and I_o is again the intensity of the incident beam. (The α subscript denotes that the sample is infinitely thick; in other words, none of the light irradiating the sample penetrates to the bottom of the sample holder) This is usually the case when the sample thickness is

approximately 5 mm or more. A perfect diffusely reflecting substance, practically never attained, would have $R_\alpha = 1$. Since it is not practical to measure R_α, the absolute remittance, the measured quantity is usually the relative remittance, R_α':

$$R_\alpha' = R_\alpha \text{ sample} / R_\alpha \text{ standard} \qquad 3.6$$

Notice that if R_α standard = 1, then the absolute and relative remittances must be equal.

In transmittance spectroscopy, it is often convenient to present data in absorbance unit, A, where $A = \log(1/T)$. this is because Beer and Lambert's law says that absorbance is linearly related to the concentration of absorbing species. In an analogous fashion, it is possible to plot log $(1/R_\alpha')$ against wavelength or frequency. This is called apparent absorbance units. It is does not imply, however, that Beer and Lambert's law is valid for diffuse reflectance spectroscopy.

Ideally one would like a function, like Beer and Lambert's law in transmission spectroscopy, to linearly relate analyte concentration with the reflectance characteristics of a diffusely reflecting sample. The function must used is that derived by Kubelka-Munk:

$$F(R_\alpha) = (1-R_\alpha)^2/2R_\alpha = K/S = 2.303\varepsilon C/S \qquad 3.7$$

where K is the absorption coefficient (twice the Beer and Lambert's law absorption coefficient), S is twice the scattering coefficient of the sample, ε is the absorptivity, and C is the analyte concentration.

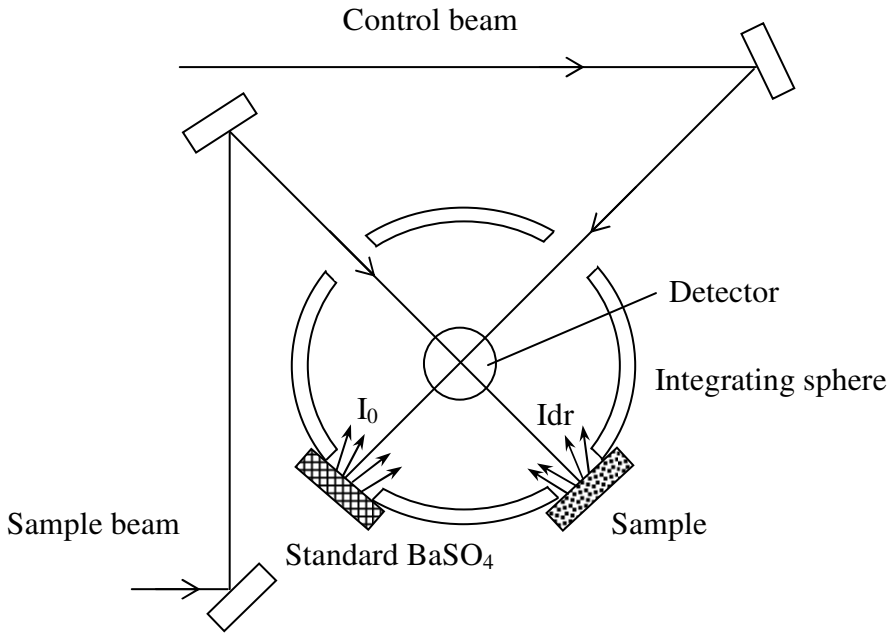

Figure 28. Solid sample measurement using the integrating sphere method
Source: Optional Accessories for Shimadzu UV-Vis spectrophotometers

The illumination of powdered samples by incident radiation leads to diffuse illumination of the materials. This incident light is then partially absorbed, partially scattered by particles. All UV-vis diffuse reflectance spectrophotometers are classical double beam spectrometers with fully automated acquisition, background subtraction and file storage as shown in Figure 28. The light sources are a D_2 lamp for UV irradiation and a Tungsten filament for the visible region, while the reflected light is detected with a photomultiplier in the UV-vis region. Integration sphere is a one of diffuse reflectance attachments. This collects all the light scattered from sample and from a reference standard and the detectors are placed on the top or bottom of the integration sphere. The classical set-up of a diffuse reflectance spectrometer is shown in Figure 28. Because the integration sphere must scatter the light and not absorb it, it is coated with a perfectly white material such as MgO, $BaSO_4$, etc. In this way, a negligibly small amount of specular reflection is included.

3.2.4. UV-Visible spectrophotometer

Source: Douglas A. S. and Donald M. W. (1996). Fundamentals of analytical chemistry (7 th ed.). New York, Thomson-Brooks / cole.

Ultraviolet-visible (UV-vis) spectroscopy is used to obtain the absorbance spectra of a molecule or compound in solution or as a solid. When the molecules absorb the suitable light energy or electromagnetic radiation, the electrons in ground state are excited to the excited state levels. The UV-vis region of energy for the electromagnetic spectrum covers 1.5 - 6.2 eV which relates to a wavelength range of 800 - 200 nm. The Beer-Lambert Law is the principle behind absorbance spectroscopy. There are three types of absorbance instruments used to collect UV-vis spectra: (1) single beam spectrometer, (2) double beam spectrometer and (3) simultaneous spectrometer. In this work, the absorption spectra of dyes solutions were recorded by double beam spectrometer which mainly has a light source (usually a deuterium or tungsten lamp), a sample holder and a detector. For the double beam instrument (Figure 29), it has a single source and a monochromator and then there is a splitter and a series of mirrors to get the beam to a reference sample and the sample to be analyzed, this allows for more accurate readings.

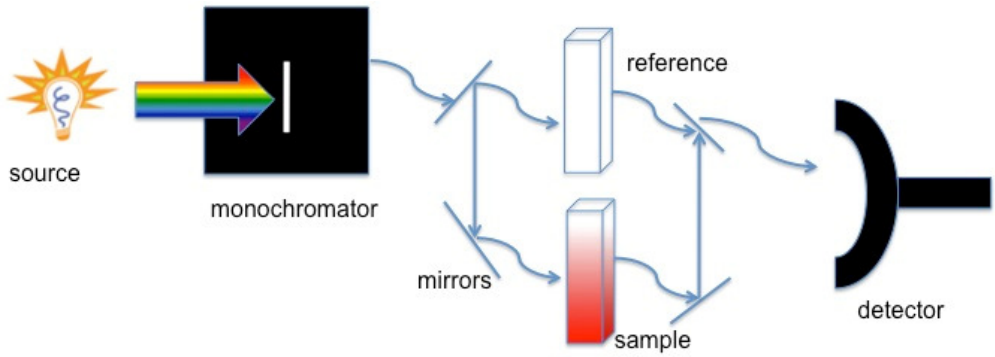

Figure 29. Illustration of a double beam UV-vis instrument
Source: http://cnx.org/content/m

The functional relationship between the quantity measured in an absorption method (A) and the quantity sought (the analyte concentration *c*) is known as Beer's law and can be written

$$A = \log (P_0 / P) = abc \qquad 3.8$$

where *a* is a proportionality constant called the absorptivity and *b* is the path length of the radiation through the absorbing medium. Since absorbance is a unitless quantity, the absorptivity has unit that render the right side of the equation dimensionless.

When concentration in Eq. 3.5. is expressed in moles per liter and *b* is in centimeters, the proportionality constant is called the molar absorptivity and is given the special symbol ε. Thus,

$$A = \varepsilon bc \qquad 3.9$$

where ε has the unit of $L.cm^{-1}.mol^{-1}$

CHAPTER 3

RESULTS AND DISCUSSION

All prepared ZnO powders in this work were synthesized by precipitation method. The mole ratio between Zn^{2+} and OH^- was kept at 1:10 through all experiments. The effect of mixing rate and Ag concentration on morphological control and photocatalytic activity of ZnO powders were presented. Firstly, the mechanism of ZnO formation at a mole ratio of OH^-:Zn^{2+} at 10 was also studied by investigation of phase and morphological change with reaction time.

3.1. ZnO

3.1.1 Mechanism of ZnO formation

The mechanism of ZnO formation was investigated by a time-resolved method. In this experiment, the $Zn(C_2H_3O_2)_2.2H_2O$ and NaOH solutions were mixed at a constant mixing rate of 30 mL/s. In this mixing rate, 150 mL of NaOH was added completely within 5 s. At the first step, when the NaOH solution was added into the Zn^{2+} solution at a high mixing rate (30 mL/s), the resulting solution produced a clear solution without any precipitant. It is possible that Zn^{2+} reacted with the OH^- to form a soluble species such as $Zn(OH)_4^{2-}$ obtaining a clear solution. After the clear solution was continuously stirred for about 3 min at room temperature, a white suspension (or primary precipitant) appeared and its XRD pattern, as shown in Figure 30 (a), matched well with the peaks of ε-$Zn(OH)_2$ crystallizing in a cubic structure (JCPDS card number 38-0385).

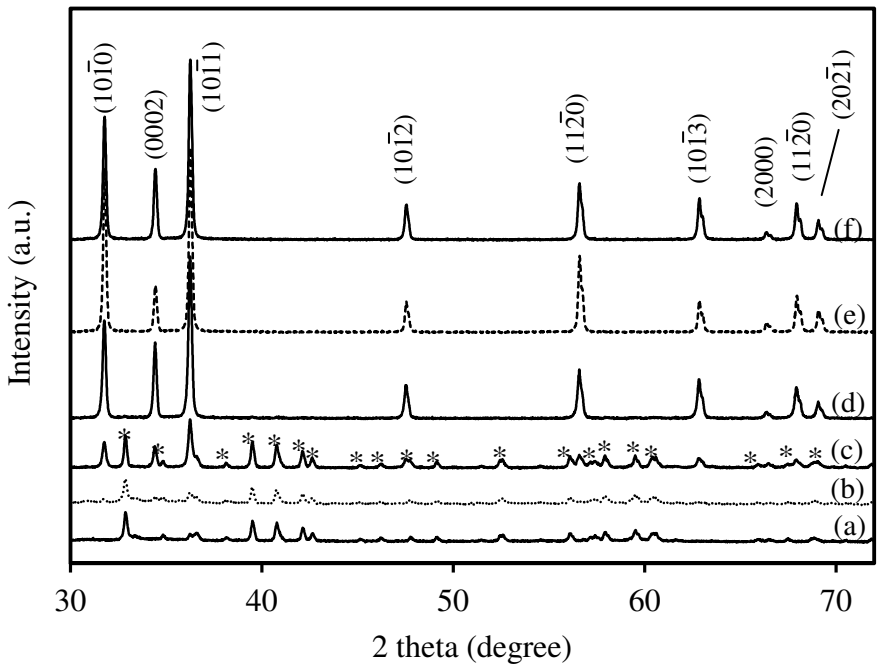

Figure 30. The time-resolved XRD patterns of white primary precipitants after heating at (a) 0, (b) 5, (c) 10, (d) 20, (e) 30 and (f) 40 min at a mixing rate of 30 mL/min. The indexed peaks correspond to the ZnO phase and the peaks marked with * can be assigned to ε-$Zn(OH)_2$ phase.

Therefore, it can be concluded that Zn^{2+} reacts with OH^- to form the $Zn(OH)_4^{2-}$ species at the first step and transform to the $Zn(OH)_2$ species later. This might be explained by the $K_{overall}$ of net reaction being less than 1 as described below:

$Zn^{2+}(aq) + 4OH^-(aq)$	$\longleftrightarrow$	$Zn(OH)_4^{2-}(aq)$	$K_f \sim 3.0\times10^{15}$
$Zn(OH)_2(s)$	$\longleftrightarrow$	$Zn^{2+}(aq) + 2OH^-(aq)$	$K_{sp} \sim 4.5\times10^{-17}$
$Zn(OH)_2(aq) + 2OH^-(aq)$	$\longleftrightarrow$	$Zn(OH)_4^{2-}(aq)$	$K_{overall} \sim 0.135$

After that, the mixture was then heated at 80 °C for the required heating times, the white precipitant products were again characterized by the XRD technique as shown in Figure 30. The amount of the ZnO phase that corresponded to the peak intensity clearly increased with an increase in the heating time. When the heating time was more than or equal to 20 min, the product is pure ZnO as clearly observed in XRD patterns (Figure 30 (d-f)). Then, the primary precipitant ε-$Zn(OH)_2$ can transform to ZnO by heating.

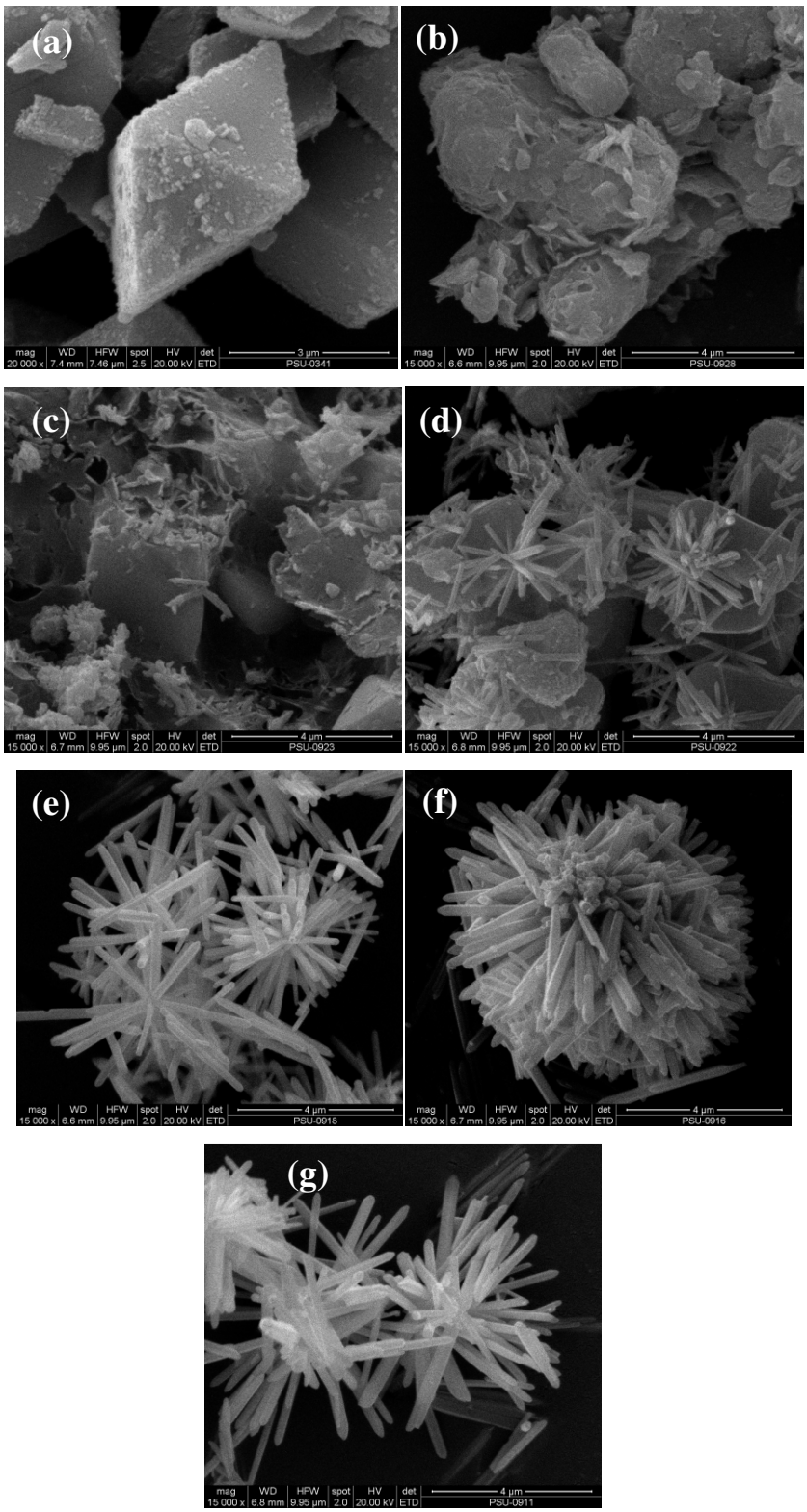

Figure 31. The time-resolved SEM images of white primary precipitants after heating at (a) 0, (b) 5, (c) 10, (d) 15, (e) 20, (f) 30 and (g) 40 min at a mixing rate of 30 mL/min.

Figure 31 shows the SEM images of the powders during different heating times. At first, the primary precipitant, ε-$Zn(OH)_2$ product, shows an octahedral prisms shape (Figure 31 (a)) as observing in the literature (Yu , *et al.,* (2008). After heating, the surface of ε-$Zn(OH)_2$ being corroded by OH^- (Figure 31(b)). When this suspension was continuously heated for 15 min, the urchin-like shape begins to grow from the surface of the octahedral prism of the ε-$Zn(OH)_2$ crystals (Figure 31(d)). Thus, it is possible to conclude that the urchin-like shape observed in the SEM image is ZnO because the population of urchin-like shape correlates with the intensity of the characteristic peaks of the ZnO structure as seen in Figure 30 and Figure 31.

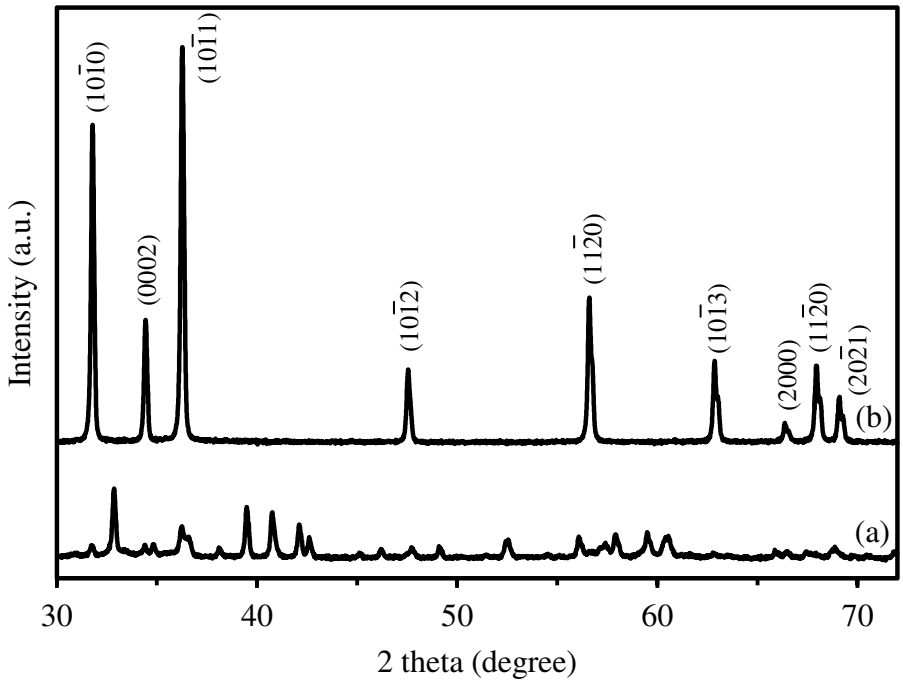

Figure 32. XRD patterns of primary precipitant after heating in (a) distillated water and (b) NaOH solution for 1 h. The indexed peaks correspond to the ZnO phase.

As ZnO grows from the $Zn(OH)_2$'s surface (from above results), it is possible that ZnO might arise from (1) the decomposition of ε-$Zn(OH)_2$ or (2) the recrystallization by the redissolution-precipitation mechanism through $Zn(OH)_4^{2-}$ species. To solve this problem, the primary precipitant, ε-$Zn(OH)_2$, that comes from the first step, was filtered and added into distilled water. This mixture was then heated

at 80 °C for 1 h and the final product was characterized by XRD technique. The resulting pattern showed the major phase of ε-$Zn(OH)_2$ with a small amount of ZnO (Figure 3(a)). In contrast, the ZnO without any impurity phase was observed in the XRD pattern when the primary precipitant was mixed in the NaOH solution and was then heated at 80 °C for 1 h (Figure 32(b)). This mean that the alkaline medium was an important factor to transform the ε-$Zn(OH)_2$ to ZnO and the possibility of ZnO formation in solution by decomposition of ε-$Zn(OH)_2$ can be eliminated.

From this result, it seems that the surface of ε-$Zn(OH)_2$ might react with OH^- to form $Zn(OH)_4^{2-}$ as a growth species followed by its decomposition to ZnO crystal on the surface of the ε-$Zn(OH)_2$ particle at a high temperature. When the heating is prolonged, the diameter of the urchin-like shape increased while the amount of ε-$Zn(OH)_2$ decreased. If the primary precipitant in the NaOH media was stirred for 1 h without heating, the XRD pattern showed a major phase of ε-$Zn(OH)_2$ with a small amount of the ZnO phase. Therefore, it can conclude that the mechanism of forming ZnO at a Zn^{2+}:OH^- = 1:10 might be as follows:

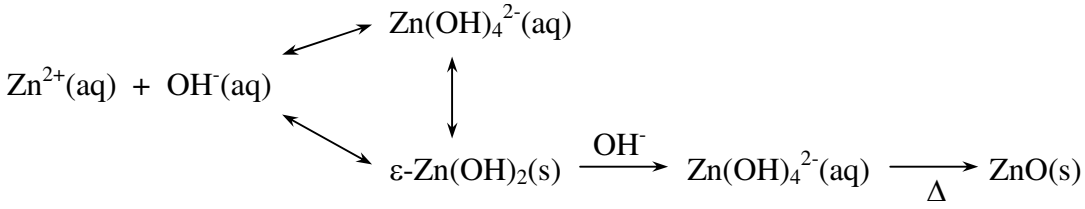

3.1.2 Effect of mixing rate

The effect of mixing rate on morphological change of ZnO was studied on three different mixing rates that is 30, 5 and 2.5 mL/s. Figure 33 shows the XRD patterns of all prepared powders at different mixing rates. The XRD analysis compared with the JCPDS card number 36-1451 revealed that all samples exhibited a single phase of ZnO crystallizing in hexagonal wurtzite structure. The lattice parameters of ZnO prepared at different mixing rates were calculated by following equation: Sumetha, *et al.,* (2007)

$$\frac{1}{d_{hkl}^2} = \frac{4}{3}\left[\frac{h^2 + kh + k^2}{a^2}\right] + \frac{l^2}{c^2} \qquad 4.1$$

where *d* is the interplanar spacing of the (*hkl*) plane, *a* and *c* are lattice parameters. The lattice parameters of all prepared ZnO powders were also presented in Table 6.

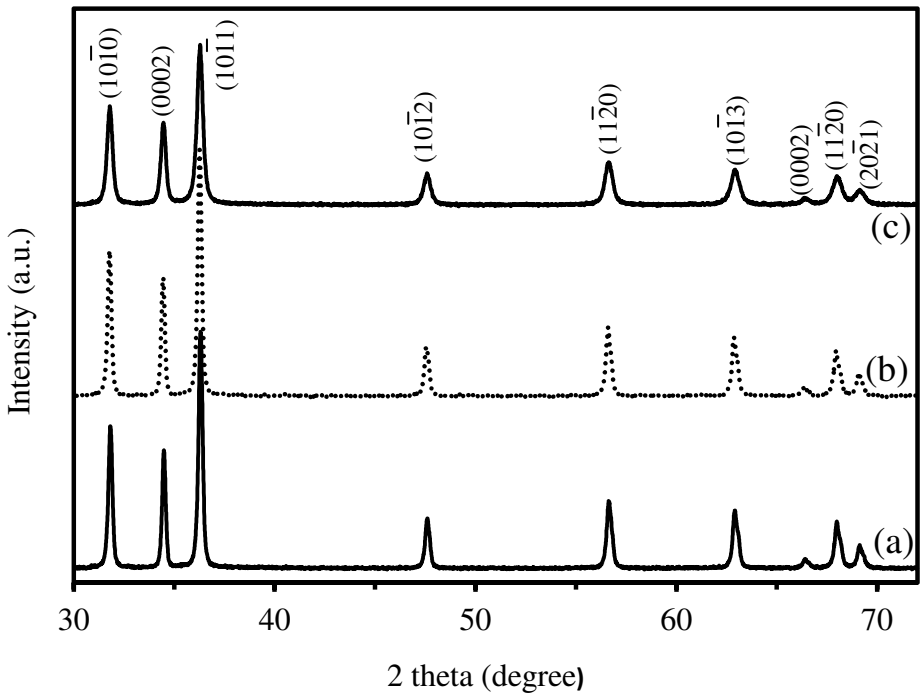

Figure 33. XRD patterns of ZnO prepared at different mixing rates (a) 30, (b) 5 and (c) 2.5 mL/s.

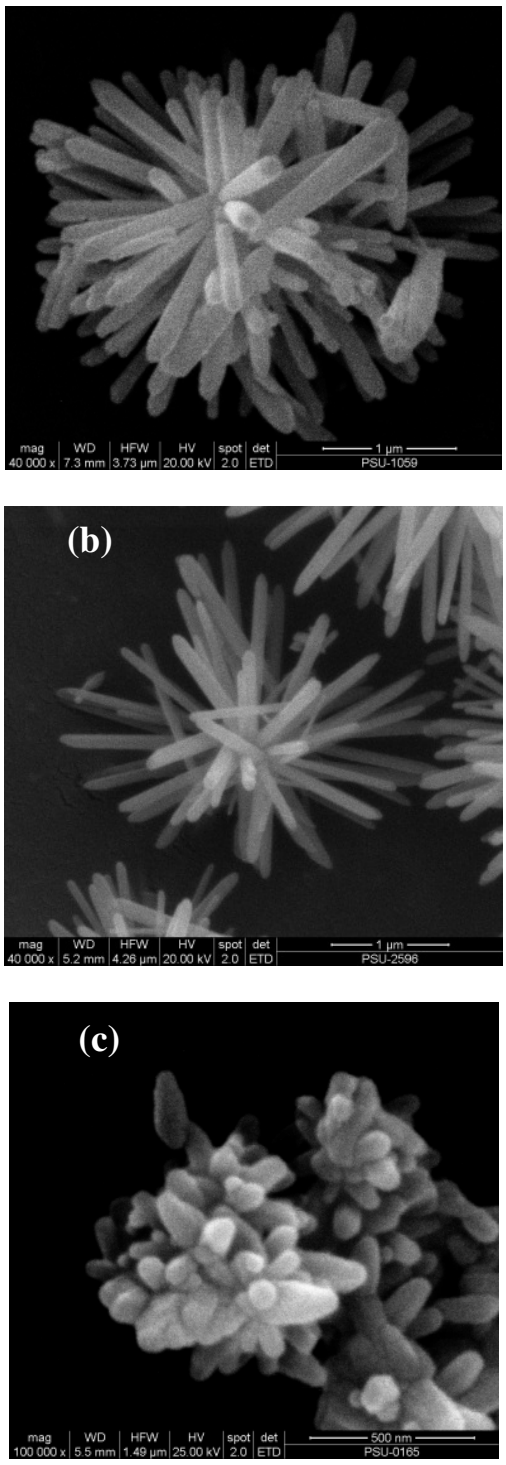

Figure 34. SEM images of ZnO prepared at different mixing rates (a) 30, (b) 5 and (c) 2.5 mL/s.

Table 6. Lattice parameters and crystallite sizes of ZnO prepared at different mixing rates.

mixing rate (mL/s)	lattice parameter (Å)		unit cell volume V (Å^3)	crystallite size (nm)
	a	c		
30	3.249	5.208	47.63	47.29
5	3.250	5.204	47.61	45.34
2.5	3.249	5.204	47.57	42.07

The crystallite sizes of all prepared ZnO powders, as shown in Table 6, were calculated by Scherrer equation: (Yu, *et al.,* (2008).

$$D = \frac{0.9\lambda}{\beta \cos\theta} \qquad 4.2$$

where D is the crystallite size (nm), λ is the wavelength of CuK_α (1.5406 Å), β is the full-width at half-maximun of the peak and θ is the Bragg angle corresponding to the peaks in the XRD patterns.

From Table 6, it is clearly seen that when the mixing rate decreased, the unit cell volume and crystallite size of ZnO powders decreased. This is in agreement with a decrease in particle sizes observed in SEM images as shown in Figure 34. From this figure, it was observed that the diameter of the urchin-like shape decreased with a decrease of the mixing rates. Furthermore, the diameter of the hexagonal facet's decreased as did the length of each urchin branch.

As mentioned above, Zn^{2+} reacts with OH^- to form $Zn(OH)_4^{2-}$ and this returns to $Zn(OH)_2$ again. The ZnO exiting on the surface of $Zn(OH)_2$ could be come from the decomposition of $Zn(OH)_4^{2-}$ species in alkaline media. In growth process, the $Zn(OH)_4^{2-}$ acted as the growth species was different to ZnO nucleus and this a forms the urchin-like structure. At high mixing rate, large amount of growth species were generated and this accelerates a supplying rate of the growth species to ZnO and gives a large or big urchin-like structure. On the other hand, the growth species are not

generated immediately as in case of high mixing rate. The growth rate is slow and a short urchin-like shape was formed.

3.1.3 Optical properties

The UV-Vis diffuse reflectance spectra of the ZnO powders prepared at different mixing rates are shown in Figure 35 (a). The absorption below 400 nm comes from the electron transitions from the valence band to the conduction band as this is the intrinsic absorption of ZnO. The estimated direct-band gap can be calculated by the equation: (Yu , *et al.,* (2008).

$$\alpha h\nu = A(h\nu - E_g)^n \qquad 4.3$$

where α is the absorption coefficient which defines as A/0.4, A is a constant, h is the Plank's constant, v is the photon frequency, E_g is the optical band gap energy and n is 1/2 for direct allowed transition. Extrapolation of the linear part until it intersected the $h\nu$-axis gives the E_g value. From Figure 35 (b), the estimated band gap energy remains almost unchanged (~ 3.218 eV) for all ZnO powders. The band gap did not increase as a particle size decreased because the sizes are not smaller than the bohr radius of ZnO (~ 3 nm). Therefore, the quantum confinement does not affect of E_g in the this study. As the ZnO shape prepared at different mixing rates did not change, many intrinsic defects in ZnO are not significant change and the defect did not affect the absorption spectra.

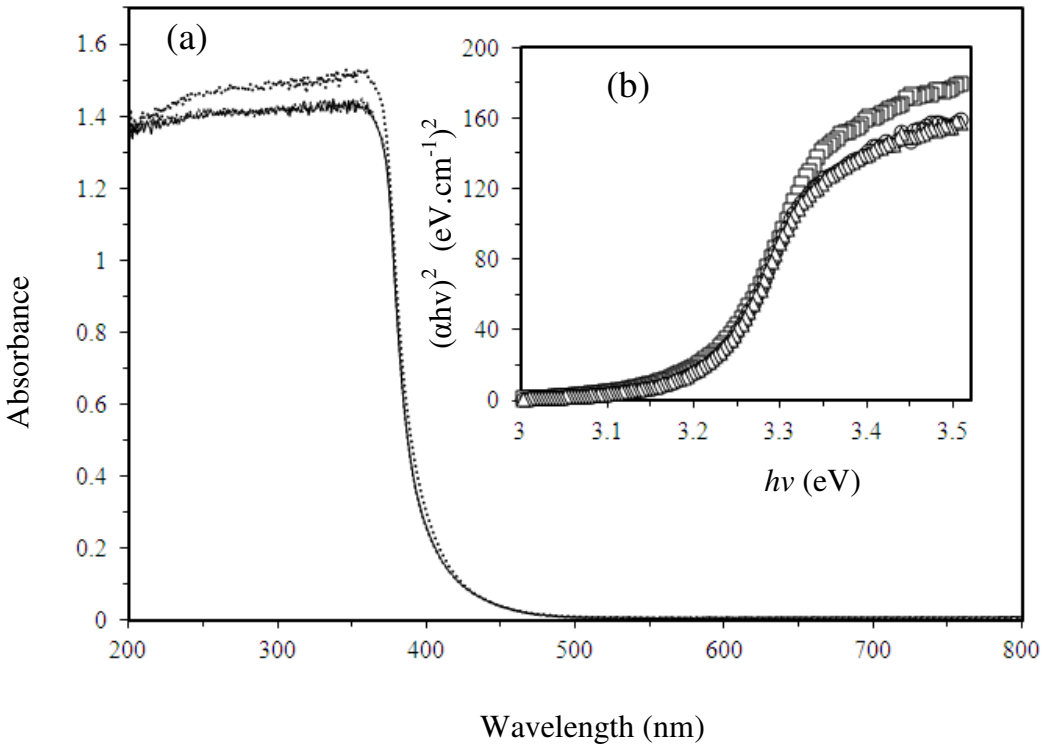

Figure 35. (a) Absorption spectra and (b) a plot between $(\alpha hv)^2$ *vs*. hv of ZnO powders prepared at different mixing rates of 30 (dot line or □), 5 (dash line or ○) and 2.5 (solid line or △) mL/s.

3.1.4 Photocatalytic properties

The photocatalytic activity of prepared ZnO powder was firstly investigated by decolorization of methylene blue solution. The decrease of absorbance of MB solution as a function of irradiation time confirms the photocatalytic activity of all prepared ZnO powders at different mixing rates as shown in Figure 36.

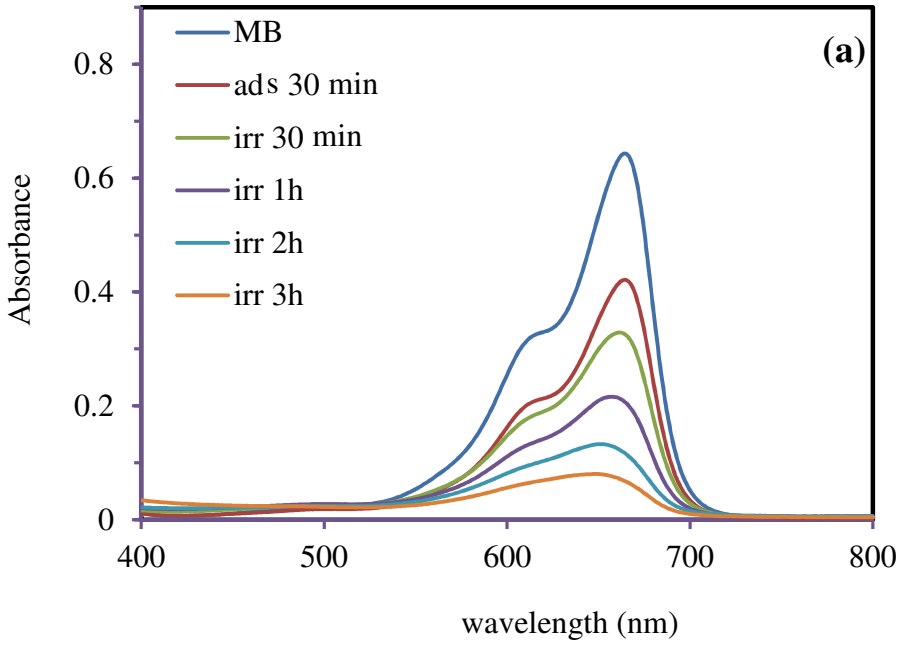

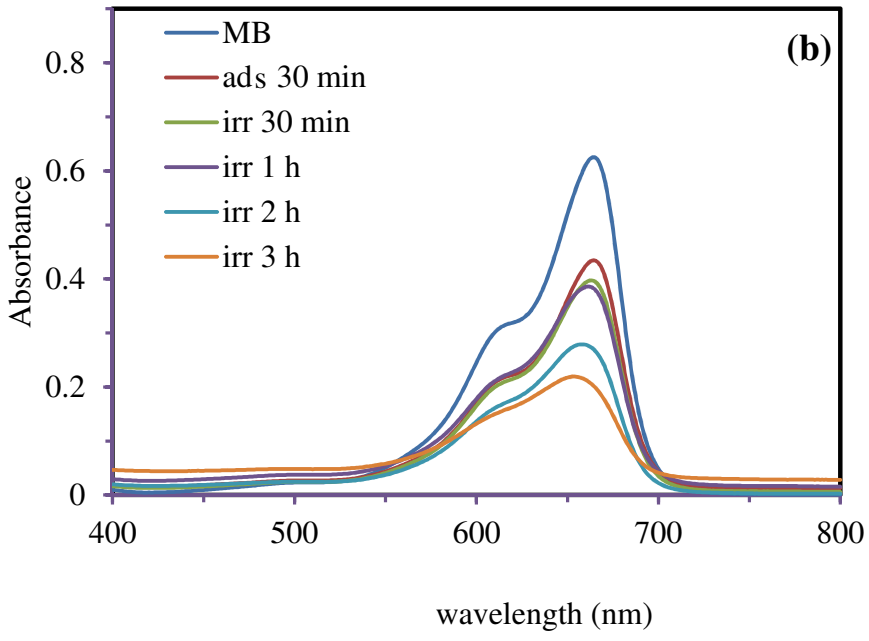

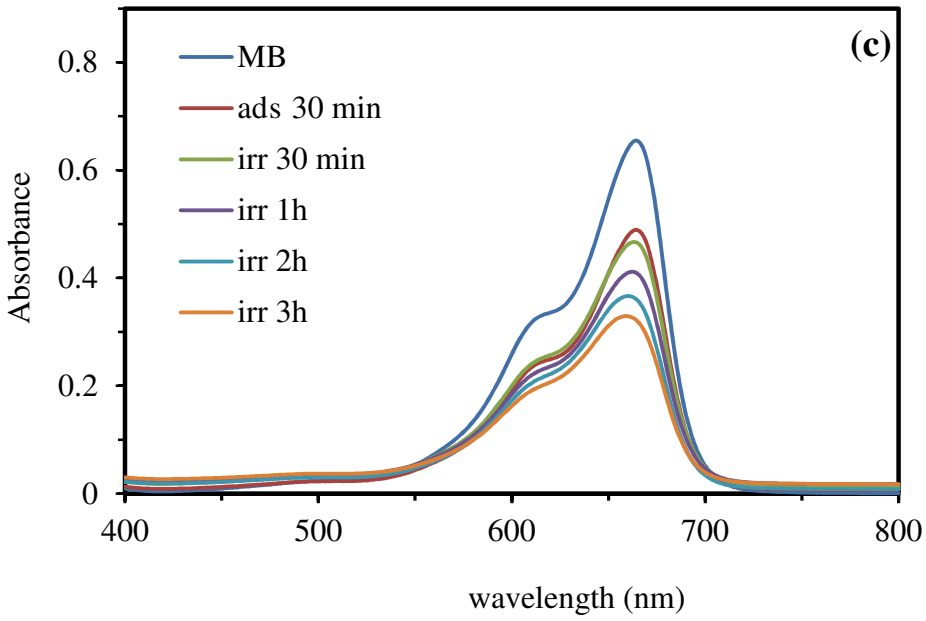

Figure 36. Absorption spectra of MB solution as a function of irradiation time under blacklight irradiation for ZnO powders prepared at different mixing rates of (a) 30, (b) 5 and (c) 2.5 mL/s.

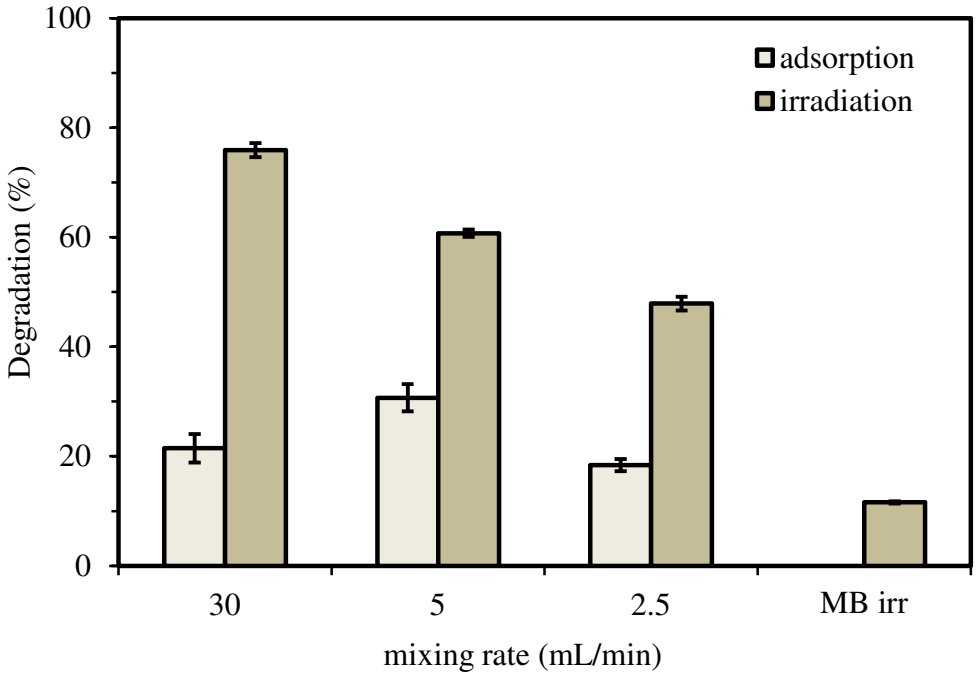

Figure 37. Effect of the mixing rate on the photocatalytic degradation of a methylene blue dye after being irradiated for 3 h. "MB irr" is the self-degradation of the methylene blue dye under blacklight illumination.

The decolorization efficiency (%) was calculated as follows: Lu, *et al.,* (2008)

$$\text{Degradation (\%)} = \frac{C_0 - C_t}{C_0} \times 100 = \frac{A_0 - A_t}{A_0} \times 100 \qquad 4.4$$

where C_0 is the initial concentration, C_t is the concentration at time t, A_0 is the initial absorbance, and A_t is the absorbance of dye at time t.

Figure 37. shows the efficiency of the photodegradation of a methylene blue (MB) solution under UV irradiation in the presence and absence of ZnO powders prepared at different mixing rates. To ensure that the efficiency does not arise from the self-degradation of the dye under UV light, the MB solution without ZnO powders was stirred under UV irradiation for 3 h. This had a low efficiency (Figure 37) and confirmed that the the MB can self-degrade and this effect can be neglected in comparison with the photocatalytic degradation by the ZnO powders. From this Figure, a decrease of the MB concentration in the dark comes from the adsorption of MB onto the surface of ZnO powders, however, this can be also neglected in comparison with the photocatalytic degradation by the ZnO powders. In fact, the photocatalytic activity depends on many factors but the surface area is the parameter of the most concern. The BET surface areas of the ZnO powders prepared at mixing rates of 30, 5 and 2.5 mL/s were 6.18, 6.24 and 7.17 m^2/g, respectively. The photocatalytic efficiency clearly did not relate to the surface area. Returning to an examination of Figure 34 and Figure 37, there is interesting that the photocatalytic efficiency increased if the diameter of the urchin-like shape or mixing rate increased. In general, a higher efficiency of photocatalytic degradation is usually obtained for ZnO with a smaller size however both size and morphology are important parameters (Gupa , *et al.,* (2007)., and also the preparation method (Wand , *et al.,* (2007). and so on. In this work, the morphology of the ZnO powder did not change to other shapes so this activity might depend on the length of the urchin's branch and/or the diameter of the hexagonal facet. Zeng et al (Zeng, *et al.,* (2009). reported that ZnO with a high population of its (0001) facet showed a better photocatalytic activity for degrading a rhodamine B solution because the OH^- species could preferentially adsorb onto this facet to produce the hydroxyl radical ($^{\bullet}OH$). Then the enhancement of the

photocatalytic activity in this work resulted from the population of the (0001) facet, more than the surface area.

In this work, we successfully synthesized the ZnO urchin-like shape by precipitation method from first part.The ZnO urchin-like shape occurred at a mixing rate of 30 mL/s showed the highest photocatalytic degradative activity on methylene blue. So the second part, to study the effect of Ag on modification of ZnO urchin-like shape prepared at a mixing rate of 30 mL/s and photocatalytic activity Ag was introduced into the system.

3.2. Ag/ZnO

From previous section (section 3.1), the ZnO urchin-like shape was synthesized by precipitation method at high alkaline media (mole ratio of OH^-/Zn^{2+} = 10). At a mixing rate of 30 mL/s, the prepared ZnO powders showed the highest photocatlytic activity compared to those of ZnO prepared from other mixing rates. Therefore, this mixing rate was selected to prepare Ag/ZnO. In this work, the order of added Ag^+ solution before and after NaOH addition was investigated and also studied their photocatalytic activities.Herein, “Method 1” referred to the addition of the $AgNO_3$ before addition NaOH, on the other hand, the NaOH was added before adding $AgNO_3$ called “Method 2”.

3.2.1. Structure and morphology of Ag/ZnO

The XRD patterns of all samples loading with different Ag contents prepared from method 1 and method 2 are shown in Figure 38 and Figure39, respectively.

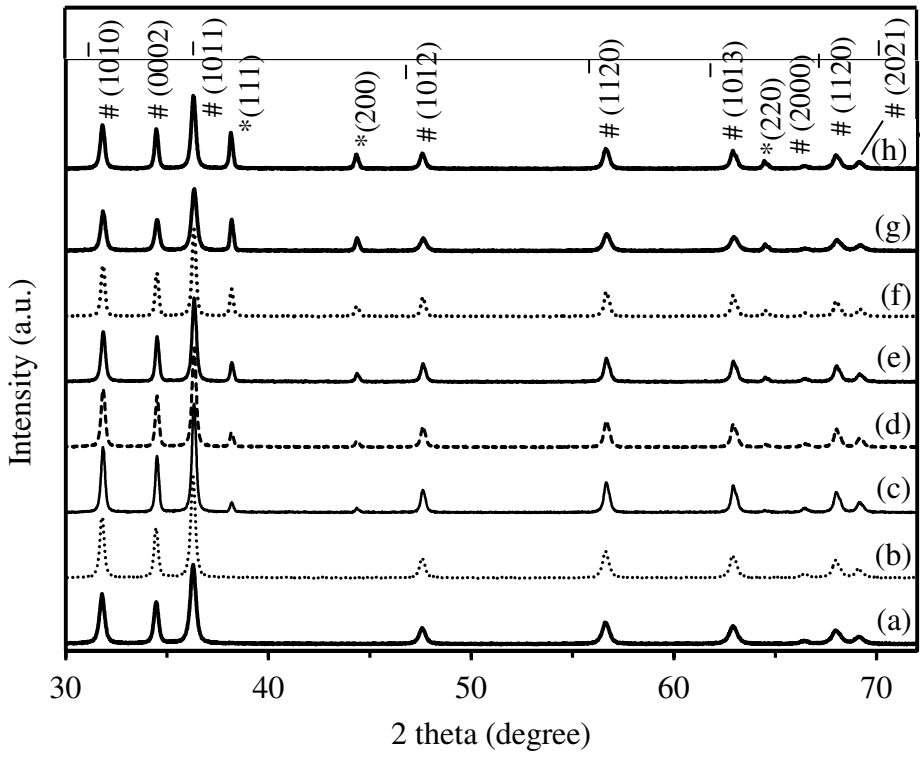

Figure 38. XRD patterns of Ag/ZnO powders prepared by Method 1 at different Ag contents of (a) 0.5, (b) 1.0, (c) 3.0, (d) 5.0, (e) 7.0, (f) 9.0, (g) 11.0 and (h) 13.0 % mol. The peak marked with # can be assigned to ZnO phase and the peak marked with * can be assigned to Ag phase.

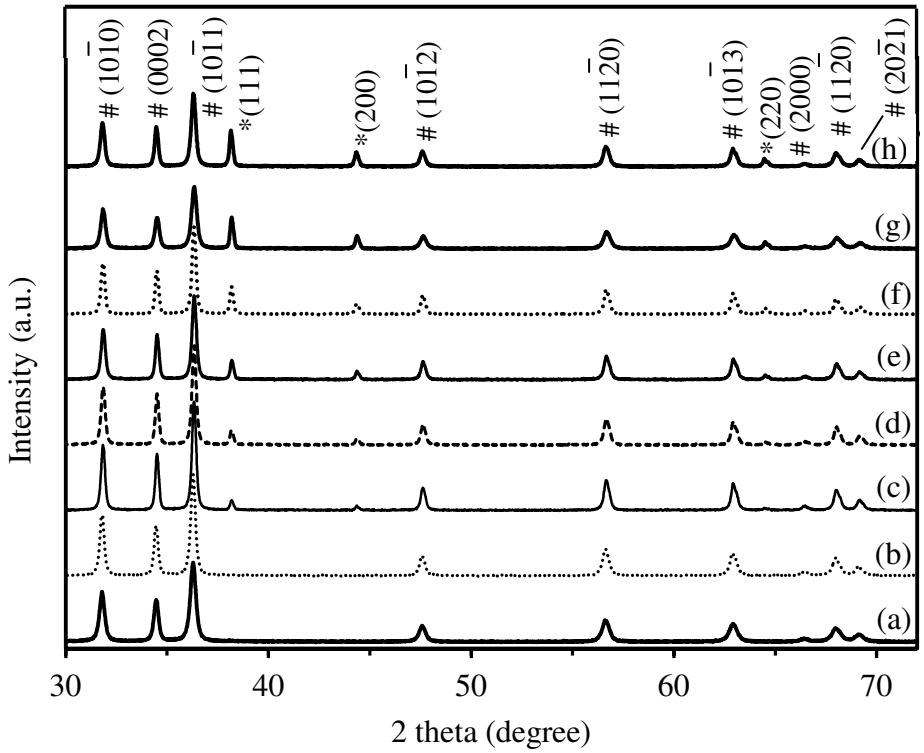

Figure 39. XRD patterns of Ag/ZnO powders prepared Method 2 at different Ag contents of (a) 0.5, (b) 1.0, (c) 3.0, (d) 5.0, (e) 7.0, (f) 9.0, (g) 11.0 and (h) 13.0 % mol. The peak marked with # can be assigned to ZnO phase and the peak marked with * can be assigned to Ag phase.

All diffraction patterns of Ag/ZnO powders prepared by both Method 1 and Method 2 can be readily indexed to two groups. Peaks marked with "#" are indexed to the hexagonal wurtzite structure (space group *P63mc*) of ZnO (JCPDS card number 36-1451). Meanwhile, peaks marked with "*" are well in agreement with face-centered cubic Ag (JCPDS card number 04-0783). No characteristic peak of impurities was observed, such as $Zn(OH)_2$ or Ag_2O. From Method 1, the metallic Ag phase was observed after the Ag content is greater than or equal to 3.0 mol% but this phase also observed in diffraction pattern of samples prepared in Method 2 when the Ag content is greater than or equal to 1.0 mol%. It might be come from the existing position of Ag phase. As Method 1 was used, the Ag^+ and Zn^{2+} were mixed together before addition NaOH then it is possible that some Ag is inside ZnO powder. As Method 2 was used, the Ag^+ was added into Zn^{2+} solution after adding NaOH then it

is possible that Ag adsorbed on the surface of ZnO prepared by Method 2 has more than those prepared by Method 1. The crystallite size calculated by the Scherrer equation (Eq. 4.2) for Ag/ZnO prepared with different methods are presented in Table 7.

Table 7. Crystallite sizes of Ag/ZnO loaded with various amounts of silver

% mol Ag	crystallite size (nm)	
	method 1	method 2
0	47.29	
0.5	46.40	45.16
1	45.45	43.78
3	44.03	40.15
5	41.23	45.77
7	44.09	45.34
9	44.05	45.48
11	40.16	45.74
13	35.17	42.51

The morphologies of Ag/ZnO powders at different Ag contents prepared from both Method 1 and Method 2 are presented in Figure 40 and Figure 41, respectively.

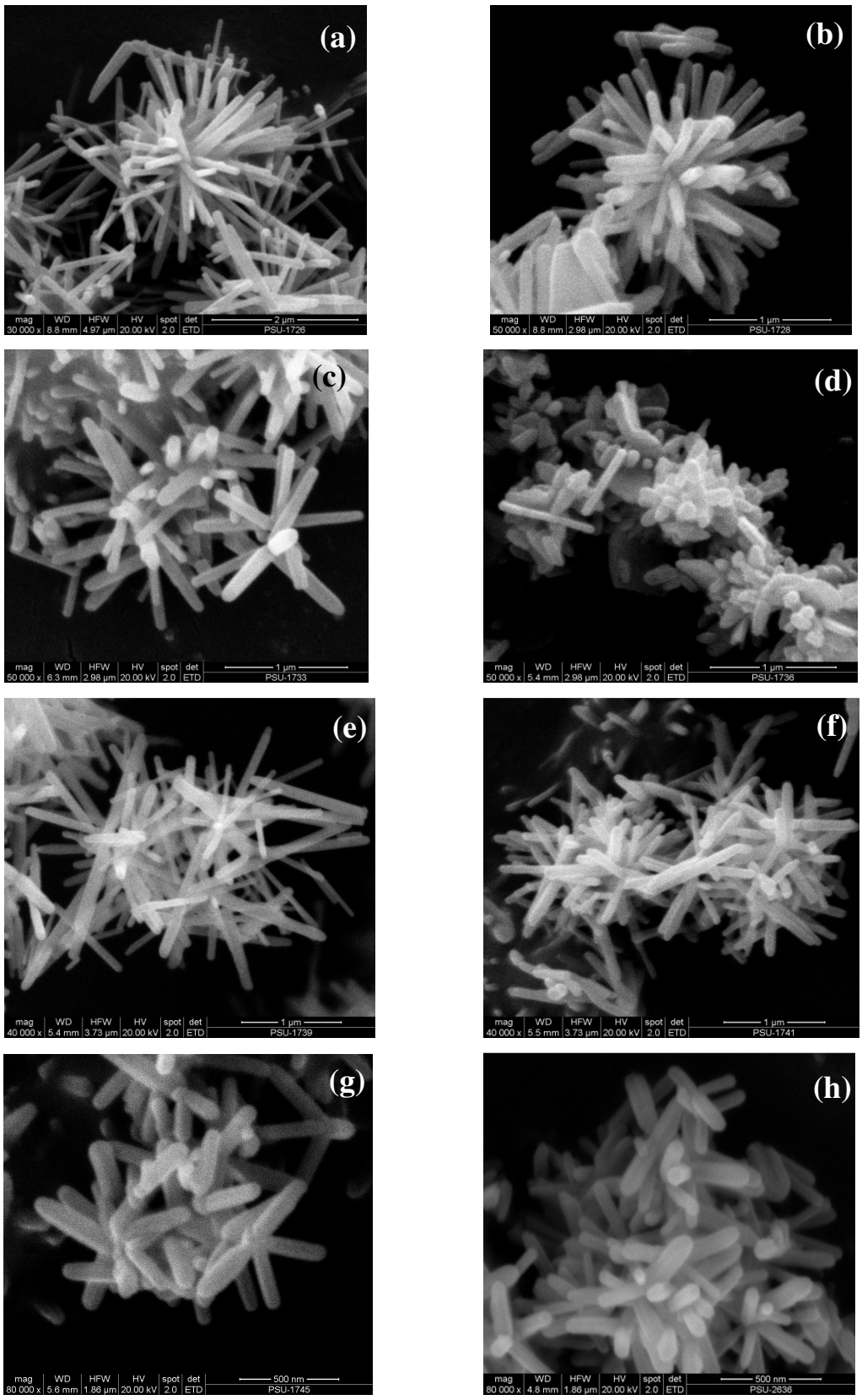

Figure 40. SEM images of Ag/ZnO powders prepared by Method 1 at different Ag contents; (a) 0.5, (b) 1.0, (c) 3.0, (d) 5.0, (e) 7.0, (f) 9.0, (g) 11.0 and (h) 13.0 % mol.

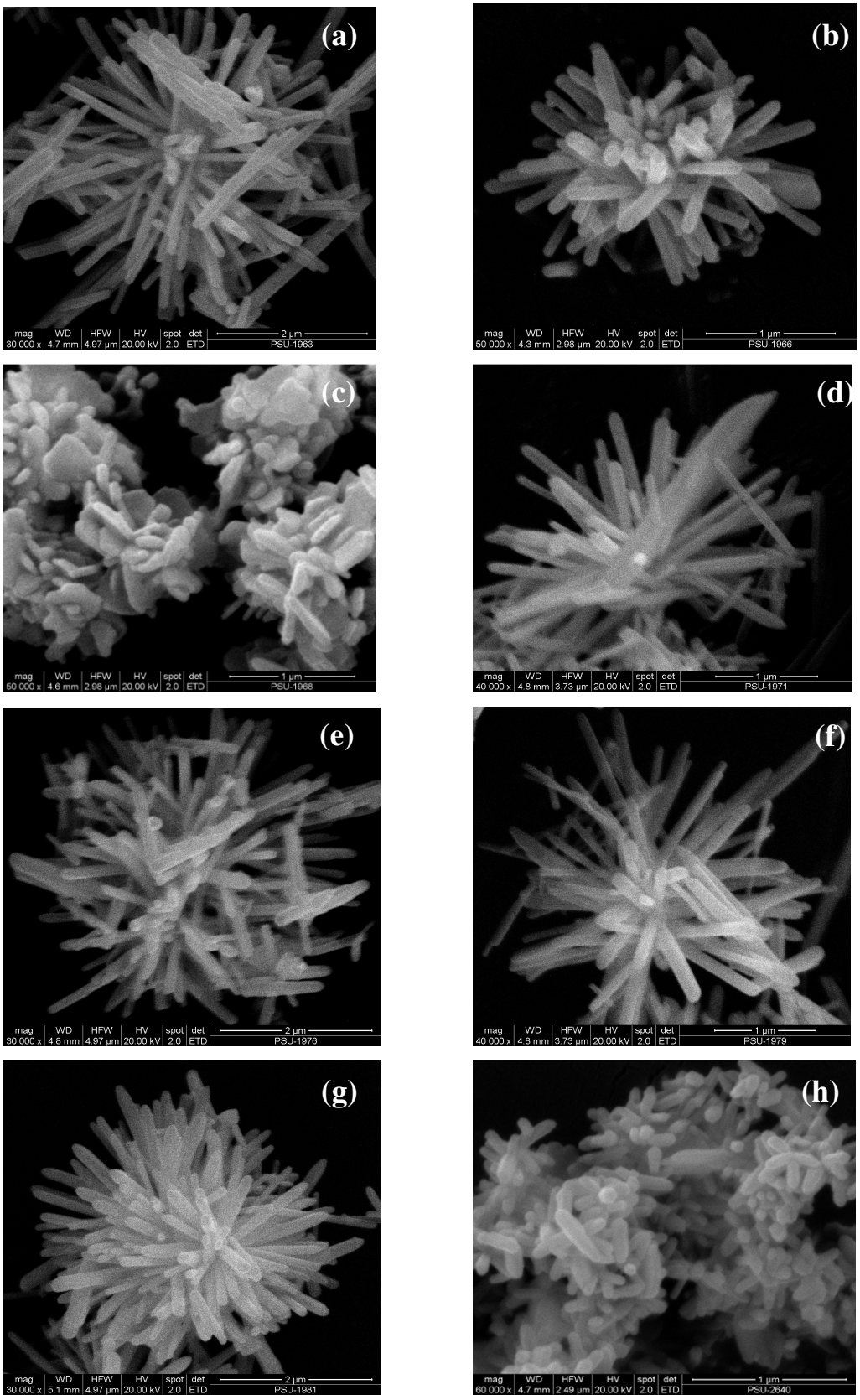

Figure 41. SEM images of Ag/ZnO powders prepared by Method 2 at different Ag contents of (a) 0.5, (b) 1.0, (c) 3.0, (d) 5.0, (e) 7.0, (f) 9.0, (g) 11.0 and (h) 13.0 % mol.

The particle sizes observed by SEM technique related to the crystallite size calculated from XRD patterns. The effect of a metal dopant on decreasing the grain size has been reported widely. This might arise from the Zener pining effect, the silver acts as an impurity, and works like an obstacle to inhibit grain growth. The limiting grain size, D, is generally given as a function of the mean radius of the pinning particles, R, and their volume fraction, f_v: (Yu , *et al.,* (2008).

$$D = (4\alpha R)/(3f_v) \quad 4.4$$

where α is a geometrical constant, The Zener drag, Z, is given by:

$$Z = (3f_v\gamma)/(2R) \quad 4.5$$

and where γ is the grain boundary energy so:

$$D = (2\alpha\gamma)/Z \quad 4.6$$

If R is constant, D is depends on $1/f_v$. According to Eq.(4.5), it is seen that the most effective pinning force results from a higher fraction of the obstacle. From Table 7, the interesting point is that the inhibiting gain growth is more efficient at low Ag^+ concentrations. In this work, Ag cluster acts as an obstacle to inhibit grain growth. At low Ag^+ concentration, the forming Ag clusters are well dispersed and the fraction of clusters increases with Ag^+ concentration and this also increases the f_v value. So, the crystallite size decreased as $AgNO_3$ concentration decrease. The smallest values observed at 5 mol% Ag for Method 1 and 3 mol% Ag for Method 2. Above these points (7 mol% Ag for Method 1 and 5 mol% Ag for Method 2), the Ag cluster tends to aggregate and reduce the f_v value therefore the crystallite size increased. When the Ag^+ concentration further increased, the inhibiting grain growth phenomena was observed, indicating by a decreas in crystallite size as shown in Table 7. Another interesting point is that the crystallite sizes or particle sizes of Ag/ZnO prepared from Method 1 are smaller than those prepared from Method 2. For Method 1, the Zn^{2+} and Ag^+ was mixed together before additing NaOH addition then Ag^+ acted as an

impurity in ZnO system, can inhibit particle growth since nucleation process. On the other hand, Ag^+ ions were added into the suspension that was obtained after NaOH addition, then the inhibition of particle growth occurs at a growth process.

3.2.2. Optical properties of Ag/ZnO

The diffuse solid absorption spectra of Ag/ZnO at various different Ag contents prepared from Method 1 and Method 2 are shown in Figure 42 (a) and Figure 43 (a), respectively. Comparing with pure ZnO as presented in Figure 35, Ag/ZnO prepared from both methods showed the wide broad band in visible region (500 – 700 nm) and this comes from the absorption of Ag on the ZnO particles.

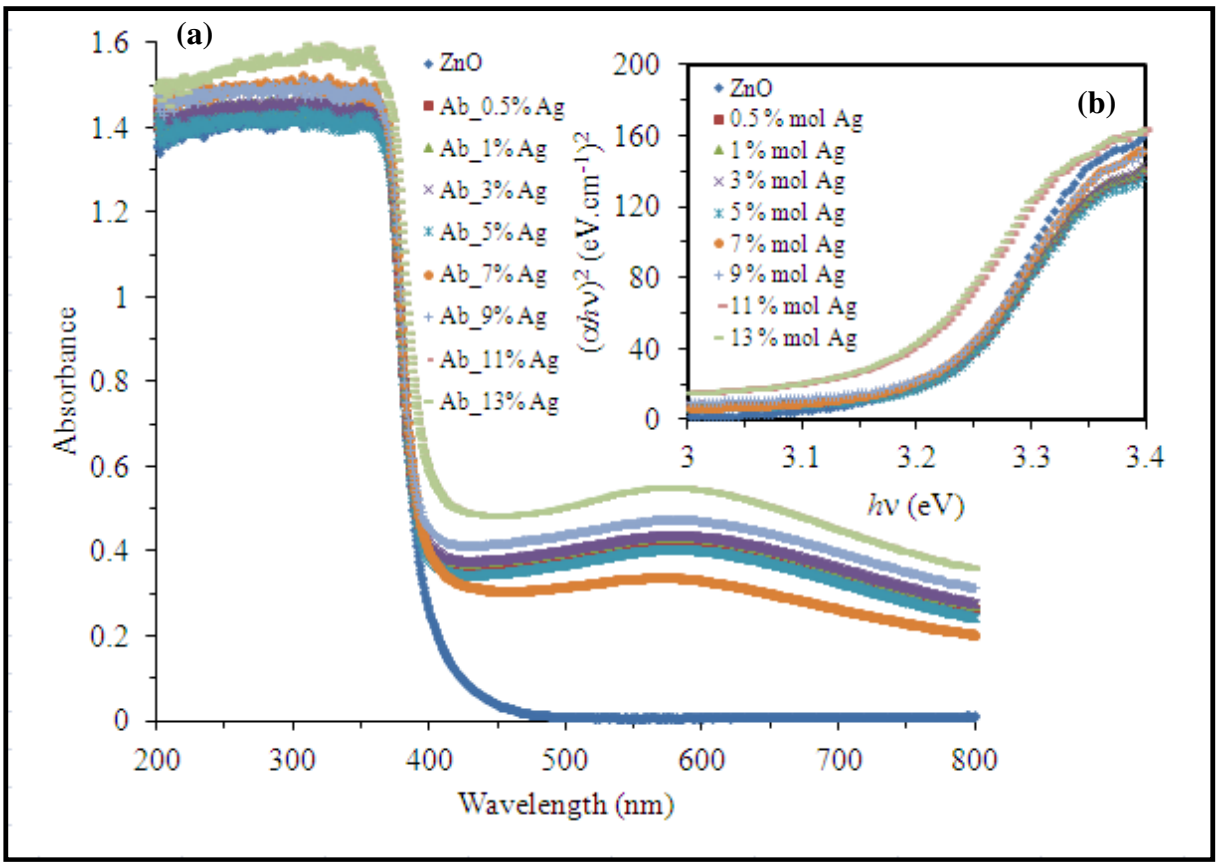

Figure 42. (a) Absorption spectra and (b) a plot between $(\alpha h\nu)^2$ *vs.* $h\nu$ of Ag/ZnO powders at various Ag contents prepared by Method 1.

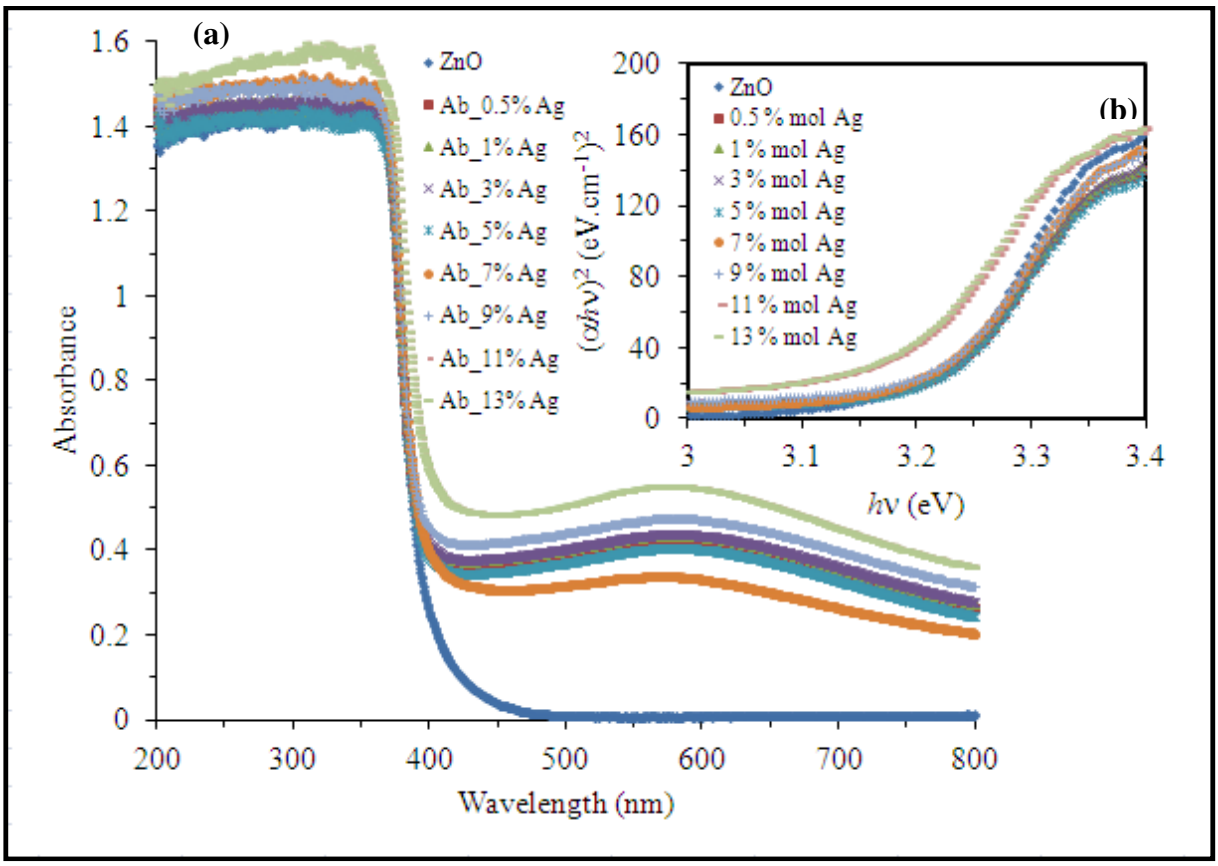

Figure 43. (a) Absorption spectra and (b) a plot between $(\alpha hv)^2$ *vs*. *hv* of Ag/ZnO powders at various Ag contents prepared by Method 2.

Figure 42 (b) and Figure 43 (b) show the plot of $(\alpha hv)^2$ *vs*. *hv* for all Ag/ZnO powders according to Eq. (4.3.) From these Figures, the estimated band gap for all Ag/ZnO at 0.5-9 mol% Ag prepared from both two methods almost unchanged (~ 3.21 eV) but the red-shifted in band gap energy (~ 3.17 eV) was found only Ag/ZnO at 11-13 mol% Ag prepared from both two methods.

3.2.3. Photocatalytic properties of Ag/ZnO

The photocatalytic activity of Ag/ZnO powders prepared from both two methods was firstly investigated by decolorization of methylene blue (MB) solution. The efficiency of the photodegradation of MB solution under UV irradiation in the presence of Ag/ZnO powders prepared at various Ag contents was shown in Figure 44. It is clearly to see that the photocatalytic efficiency can be divided into two ranges. The Ag/ZnO powders prepared by Method 1 showed a lower efficiency compared with those activities prepared by Method 2 when the Ag loadings are lower than or equal to 7 mol%. As $AgNO_3$ concentration was higher than 7 mol%, Ag/ZnO powders prepared by Method 1 showed the higher efficiency of photocatalytic degradation of MB solution than those photocatalysts prepared by Method 2.

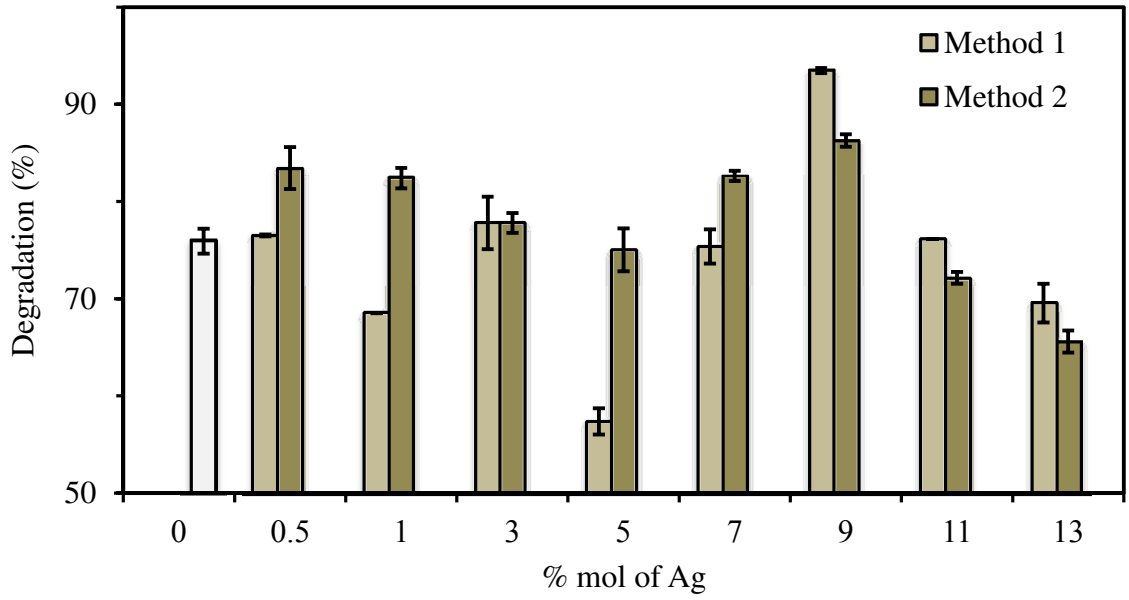

Figure 44. Comparison of photocatalytic degradation of MB solution after irradiatin 3 h using Ag/ZnO powders at various mol% of Ag prepared from Method 1 and Method 2.

The difference in photocatalytic activity of Ag/ZnO powder prepared by Method 1 and Method 2 could be probably explained by a position of metallic silver. For Method 1, it is possible that some Ag can be incorporated into ZnO because the staring solution was in a form of Zn^{2+} and Ag^{+} ions. So, the Ag contents on the surface of ZnO are probably lower than those Ag/ZnO prepared by Method 2. The Ag on the surface of ZnO plays an important role in enhance the photocatalytic activity as can be seen in Figure 45.

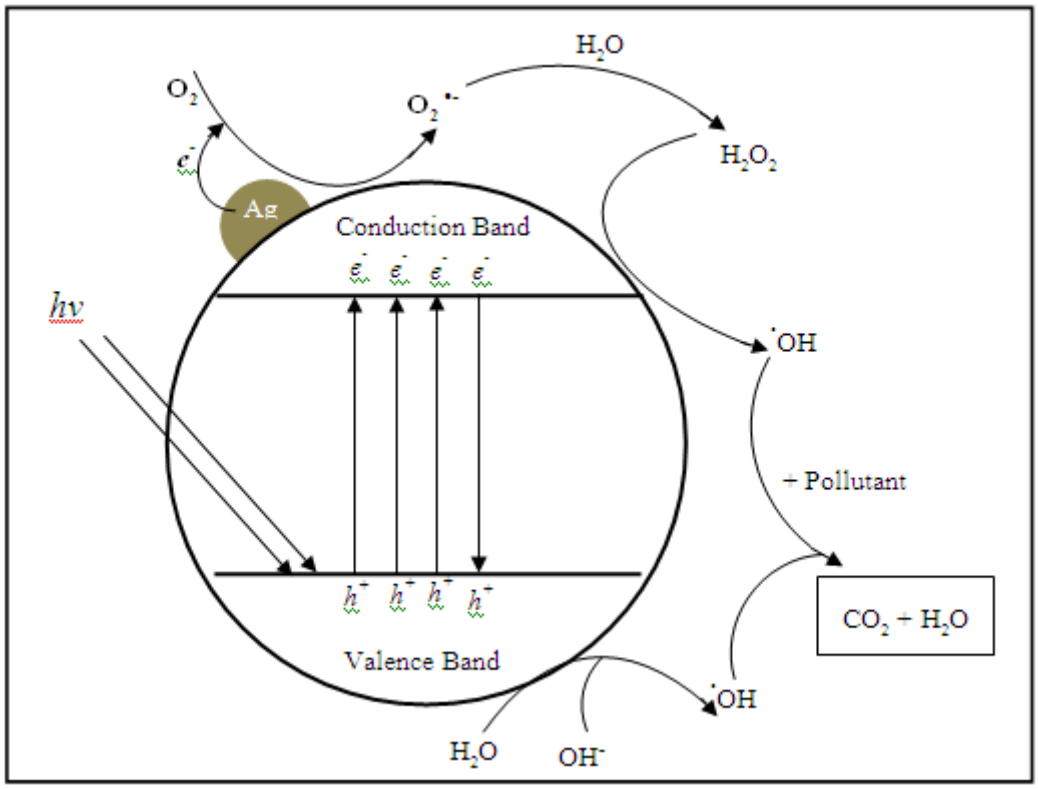

Figure 45. Mechanism of photocatalysis for Ag deposited on the surface of ZnO under UV irradiation.

Source: Behnajady, *et.al.,* (2008).

However, a large amount of silver coverage on surface of ZnO can reduce the absorbed light of ZnO and also reduce the photocatalytic efficiency. As silver concentration was than 9 mol%, it is possible that the coverage of Ag on the surface of ZnO could be high and the photocatalytic efficiency of Ag/ZnO prepared by Method 1 and 2 continuous decreased with increasing of Ag loading.

From Figure 44, ZnO leading with 9 mol% Ag showed the best efficiency, then this catalyst is also tested with another dyes i.e. rhodamin B (Rh-B) as a cationic dye and reactive orange 16 (RO-16) as a anionic dye. The Ag/ZnO powders prepared by Method 1 still showed the photocatalytic degradation more than those prepared by Method 2 for all three dyes as presented in Figure 46.

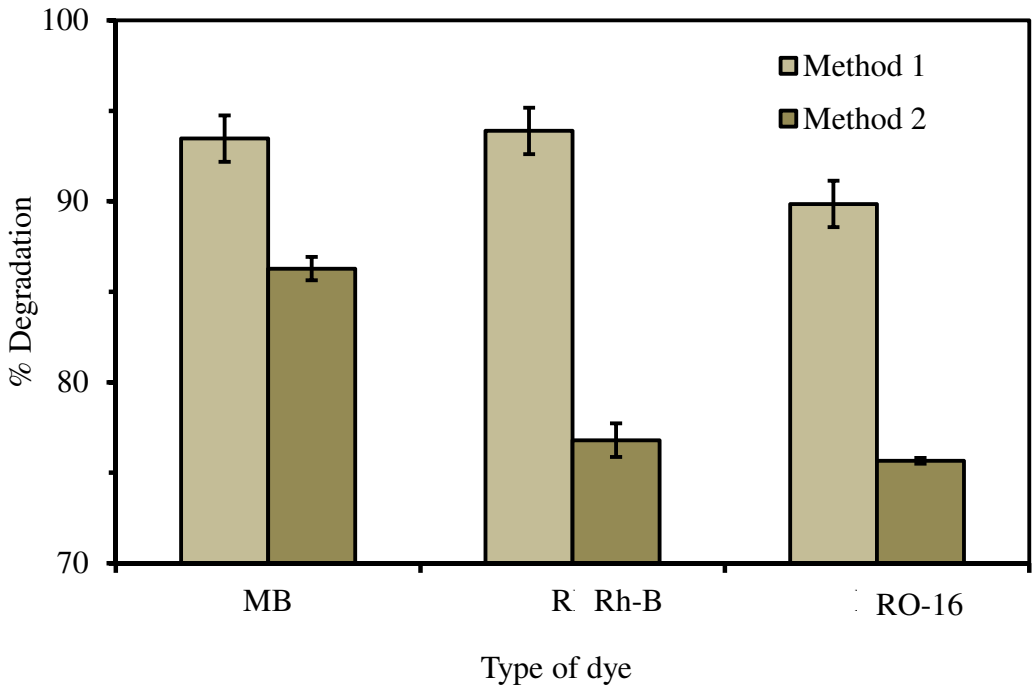

Figure 46. Photocatalytic degradation of methylene blue (MB), rhodamine B (Rh-B) and reactive orange (RO-16) for Ag/ZnO powders loading with 9 mol % of Ag prepared by different method under UV illumination for 3 h

3.2.3.1. Effect of initial pHs

The effect of pH on photocatalytic activity of prepared Ag/ZnO photocatalyst was evaluated by the degradation of methylene blue (MB), rhodamine B (Rh-B) and reactive orange 16, (RO-16) dyes at pH of 3, 7, 9 and 10. The selected catalyst in this experiment was Ag/ZnO loading with 9 mol% Ag prepared by Method 1. The degradation efficiencies for all three dyes after irradiating UV illumination for 3 h are presented in Figure 47.

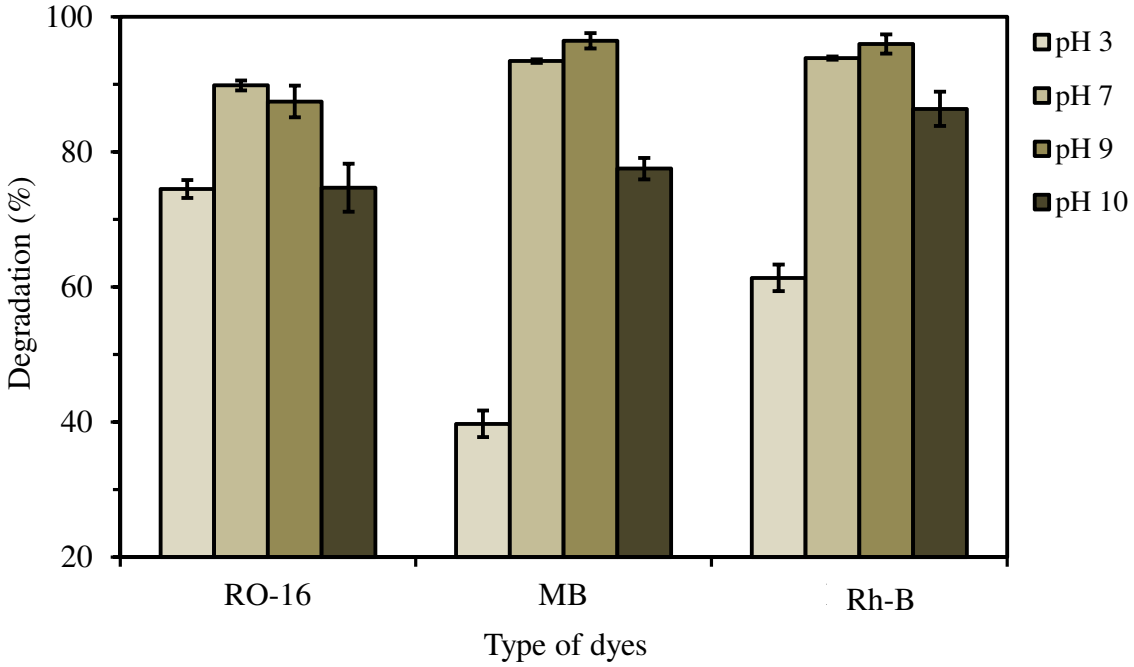

Figure 47. The photocatlytic degradation of dyes solution for Ag/ZnO loading with 9 mol% Ag prepared by Method 1 at pH 3, 7, 9 and 10 under UV irradiation for 3 h

From Figure 47, Ag/ZnO powders showed the highest photocatlytic efficiency at pH 7 for RO-16 and at pH 9 for Rh-B and MB. At high pH, surface of Ag/ZnO probable, has a negatively charge and this can adsorb the cationic dye following reacting with reactive radicals. On the other hand, the negatively charge of Ag/ZnO repulses the anionic dye and probably reduces the photocatalytic activity. The anionic dye was degraded easier than cationic dye at low pH values. From cationic dye, the best efficiency was found at pH 9 due to the solution has more OH^-. There species

also react with holes in valence band to produce the •OH. It means that the •OH formation can be easier to occur. At high pH, this activity however reduced because of the possibility of alkaline dissolution of ZnO. (Yang, *et al.,* 2010).

3.2.3.2. Effect of photocatalyst loading

The effect of amount of Ag/ZnO powders on photocatalytic degradation was also studied by a variation of photocatalyst in the range of 0.05 – 0.25 g in 150 mL of 1 x 10^{-5} M dyes solutions. The selected are methylene blue (MB), rhodamine B (Rh-B) and reactive orange 16, (RO-16). The degradation efficiency calculated from the absorbance after UV irradiated for 3 h are presented in Figure 48.

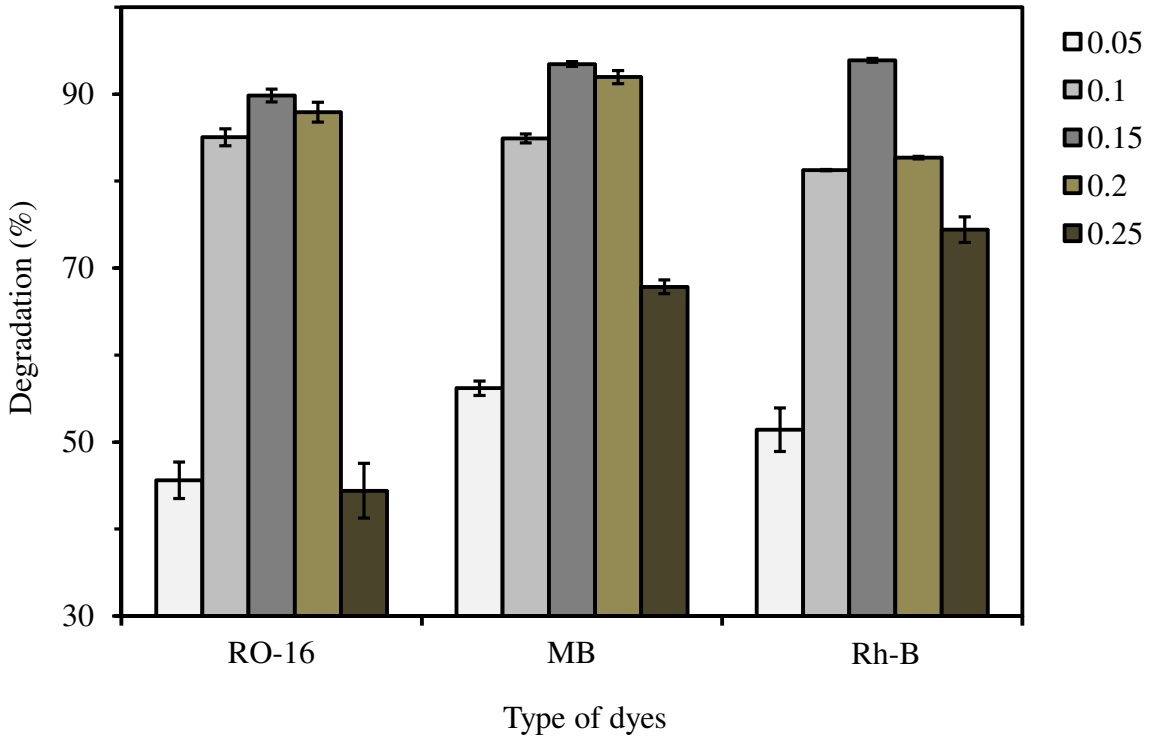

Figure 48. Effect of photocatalyst loading on the photocatalytic degradation of three dyes solution for Ag/ZnO under UV illumination for 3 h

From Figure 48, it was observed that the photocatlytic efficiency increasing with an increased of Ag/ZnO until the Ag/ZnO is 0.15. Above this point, the decolorization rate was decreased because some particles may be shielded by sticking together and this would reduce the photo flux per surface area and lead to reduce the photocatalytic efficiency. (Yang, *et al.,* 2010).

CHAPTER 4
CONLUSIONS

In this work, various sizes of the urchin-like shaped ZnO powder were synthesized by varying the mixing rate of the $Zn(CH_3COO)_2.2H_2O$ and NaOH starting solutions at 2.5, 5 and 30 mL/min. After the starting solutions were mixed at all mixing rates, the Zn^{2+} reacted with the OH^- to form $Zn(OH)_4^{2-}$ at the first stage and produced a clear solution, these species can then turn to $Zn(OH)_2$. When this suspension was continuously stirred in a heated NaOH solution, it transformed to a white ZnO precipitant. The size of the urchin-like shape depended on the mixing rate. A decrease of the diameter of the urchin-like shape influenced the diameter of hexagonal facet that is the reactive facet on which the $^{\bullet}OH$ radical is generated. Therefore, the performance of the photocatalytic activity decreased with decreasing of the size of the urchin-like shape.

In methylene blue solution, Ag/ZnO powder prepared by Method 1 showed a better photocatalytic efficiency than Ag/ZnO powder prepared by Method 2 because Ag contents on the surface of ZnO prepared from Method 1 is more than those prepared from Method 2. However, the best photocatalytic efficiency was found at Ag/ZnO loading with 9 mol% Ag prepared by Method 2. This photocatalyst can also degrade other dyes such as rhodamine B and reactive orange 16. For methylene blue and rhodamine B (cationic dyes), Ag/ZnO powders showed the best efficiency at pH 9 but pH 7 is the best condition for reactive orange 16 (anionic dye). This might be due to the nature of dye and surface's charge of Ag/ZnO at different pHs. The photocatalytic activity also depends on the catalyst loading and the best efficiency for all three dyes was found at same value of 0.15 mg in 150 mL of 1×10^{-5} M of dyes solutions.

REFERENCES

Ameen, S., Shaheer, M., Shin, H.S. (2012). Growth and characterization of nanospikes decorated ZnO sheets and their solar cell application. *J. Chem. Eng*. 195. 307–313.

Aneesh, P.M., Vanaja, K.A., Jayaraj, M.K. (2007). Synthesis of ZnO nanoparticles by hydrothermal method. *Nanophotonic Materials IV*. 6639, 66390J1-66390J8.

Bai, S., Shieh, J., Tseng, T. (1995). Characteristic analysis of ZnO varistors made with spherical precipitation powders. *Materials Chemistry and Physics.* 41, 104-109.

Behnajady, M., Modirshahla, N., Shokri, M., Rad, B. (2008). Enhancement of photocatalytic activity of TiO_2 nanoparticles by silver doping: Photodeposition versus liquid impregnation methods. *J. Global NEST.* 10, 1-7.

Caglar, M., Ilican, S., Caglar, Y. and Yakuphanoglu, F. (2009). Electrical conductivity and optical properties of ZnO nanostructured thin film. *Applied Surface Science.* 255, 4491–4496.

Chakrabarti, S. and Dutta, B. K. (2004). Photocatalytic degradation of model textile dyes in wastewater using ZnO as semiconductor catalyst. J. *of Hazardous Materials B.* 112, 269–278

Chen, J., Deng, H., Wei, M. (2009). Hydrothermal synthesis and optical properties of ZnO single-crystal hexagonal microtubes. *Materials Science and Engineering B.* 163, 157-160.

Coleman, V. A. and Jagadish, C. (2006). Basic Properties and Applications of ZnO. In Zinc Oxide Bulk, Thin Films and Nanostructures. Jagadish, C. and Pearton, S., Ed. Elsevier Limited.

Connolly, J. R. 2007. Introduction to X-Ray Powder Diffraction. (online) Available http://epswww.unm.edu/xrd/xrdclass/01-XRD-Intro.pdf (31 June 2009)

Ding, S., Guo, J., Yan, X., Lin, T., Xuan, K. (2005). Radial spherical ZnOstructures with nanorods grown on both sides of a hollow sphere-like core. *J Crystal Growth*. 284, 142–148.

Douglas A. S. and Donald M. W. (1996). Fundamentals of analytical chemistry (7 th ed.). New York, Thomson-Brooks / cole.

Fernández, J., Kiwi, J., Lizama, C., Freer, J., Baeza, J. and Mansilla, H. D. (2002). Factorial Experimental Design of Orange II Photacatalytic Discolouration. *J. Photochem. Photobiol. A: Chem*. 151, 213-219.

Fu, D., Hun, G., Chang, Y., Dong, J. (2011). The synthesis and properties of ZnO-graphene nano hybrid for photodegradation of organic pollutant in water. *Materials Chemistry and Physics.* 132, 673-681.

Gang, J., Kuan, P., Hua, L., Sun, Z. (2012). Preparation and photocatalytic performance of porous ZnO microrods loaded with Ag. *Trans. Nonferrous Met. Soc. China.* 22, 873-878.

Gapa, J., Barick, K.C. (2011). Defect mediated photocatalytic activity in shape-controlled ZnO nanostructure. *J. Alloys Compd.* 509, 6725–6730.

Gome da Silva, C. and Faria, J.L. (2003). Photochemical and Photocatalytic Degradation of An Azo Dye in Aqueous Solution by UV Irradiation. *J. Photochem. Photobiol. A: Chem*. 155, 133-143.

Gopal, M., Chan, W. J. M. and De Jonghe, L. C. (1997). Room Temperature Synthesis of Crystalline Metal Oxides. *J. Mater. Sci.* 32, 6001-6008.

Gomes de Moraes, S.; Sanches Freire, R. and Duran, N.(2000). Degradation and Toxicity Reduction of Textile Effluent by Combined Photocatalytic and Ozonation Processes. *Chemosphere*. 40, 369-373.

Hachem, C.; Bocquillon, F.; Zahraa, O. and Bouchy, M. (2001). Decolourization of Textile Industry Wastewater by the Photocatalytic Degradation Process. *Dyes and Pigments.* 49, 117-125.

Han, Y., Ding, Y., Yin, W., Ma, Z. (2006). Preparation of homogeneous ZnO nanoparticles via precipitation-pyrolysis with $Zn_5(CO_3)_2(OH)_6$ as precursor. *Transactions of Nonferrous Metals Society of China*. 16, 1205–1212.

Huang, W., Jia, J., Zhou, X., Lin, Y. (2010). Morphology controlled synthesis of ZnO crystal-pH-dependent growth. *Mater. Chem. Phys.* 123, 104–108.

Hung, S., Jung, C., Hsu, M. (2011). Improved photocatalytic performance of ZnO nanograss decorated pore-array films by surface texture modification and silver nanoparticle deposition. J. *Hazardous Materials.* 198, 307-316.

Jang, JM., Kim, SD., Chai, HM., Kim, JY., and Jang, WG. (2008). Morphology change of selfe assembled ZnO 3D nanostructures with different pH in the simple hydrothermal process. *Mat. Chem. Phys.* 202, 129-137.

Karunakaran, C., Rajeswari, V., Gomathisankar, P. (2011). Enhanced photocatalytic and antibacterial activities of sol-gel synthesized ZnO and Ag-ZnO. *Materials Science in Semiconductor Processing.* 14, 133-138.

Lai, Y., Meng, M., Yu, Y. (2010). One-step synthesis, characterizations and mechanistic study of nanosheets-constructed fluffy ZnO and Ag/ZnO spheres used for Rhodamine B photodegradation. *Applied Catalysis*. 100, 491–501.

Lange, A., Sharma, S., Ningthoujam, R., Pode, R. (2013). Low temperature dielectric studies of zinc oxide (ZnO) nanoparticles prepared by precipitation method. *Advanced Powder Technology*. 24, 331-335.

Li, P. Liu, H., Zhang, Y.-F. Wei, Y. and Wang, X.-K.(2007). Synthesis of flower-like ZnO microstructures via a simple solution route Mater. *Chem. And Phys.* 106: 63-69.

Liu, J., Huang, X. (2006). A low-temperature synthesis of ultraviolet-light-emitting ZnO nanotubes and tubular whiskers. *J. Solid State Chemistry.* 179, 843 – 848.

Li, X., Wang, Y. (2011). Structure and photoluminescence properties of Ag-coated ZnO nano-needles. J. *Alloys and Compounds.* 509, 5765-5768.

Li, W.-J., Shi, E.-W., Zhoug, W.-Z. and Yin, Z.-W. J. (1999). Growth mechanism and growth habit of oxide crystals. *Cryst. Growth.* 203, 186-196.

Lu, C.-H., Lai, Y.-C. and Kale, R. B. (2008). Influence of alkaline sources on the structural and morphological properties of hydrothermally derived zinc oxide powders. *J. of Alloys and Compounds*.324, 1430-1438.

Lu, W., Gao, S., Wang, J. (2008). One-pot Synthesis of Ag/ZnO Self-Assembled 3D Hollow Microspheres with Enhanced Photocatalytic Performance. *J. Phys. Chem. C*. 112, 16792-16800.

Medina, A., Bejar, L. (2012). Characterization of ZnO nanoparticles with short-bar shape produced by chemical precipitation. *Materials Letters*.71, 81-83.

Mekasuwandumrong, O., Pawinrat, P., Praserthdam, P., Panpranot, J. (2010). Effects of synthesis conditions and annealing post-treatment on the photocatalytic activities of ZnO nanoparticles in the degradation of methylene blue dye. *Chemical Engineering Journal*. 164, 77-84.

Paez, J.E., Villegas, A.C., Duran, C., Fernandez, J.F. (2001). Controlled precipitation methods: formation mechanism of ZnO nanoparticles. J. *European Ceramic Society.* 21, 925-930.

Raoufi, D. (2013). Synthesis and microstructural properties of ZnO nanoparticles prepared by precipitation method. *Renewable Energy*. 50, 932-937.

Ren, C., Yang, B., Wu, M., Xu, J., Fu, Z., Iv, Y., Guo, T., Zhao, Y., Zhu, C. (2010). Synthesis of Ag/ZnO nanorods array with enhanced photocatalytic performance. *J. Hazardous Materials.* 182, 123-129.

Sagar, P., Shishodia, P.K., Mehra, R.M.(2007). Influence of pH value on the quality of sol–gel derived ZnO films. *Applied Surface Science.* 253: 5419-5424.

Sahu, R., Ganguly, K., Mishra, T., Mishra, M., Ningthoujam, R.S., Roy, S.K., Pathak, L.C. (2010). StabiliZation of intrinsic defects at high temperatures in ZnO nanoparticles byAg modification. *J. Colloid and Interface Science.* 366, 8-15.

Saito, G., Hosokai, S., Akiyama, T. (2010). Synthesis of ZnO nanoflowers by solution plasma. *Materials Chemistry and Physics.* 130, 79-83.

Saleh, R., Djaja, N., Prakoso, S. (2013). The correlation between magnetic and structural properties of nanocrystalline transition metal-doped ZnO particles prepared by the co-precipitation method. *J. Alloys and Compounds*. 546, 48-56.

Scintag, Inc.1999. Chapter 7: Basics of X-ray Diffraction (online). Available http://epswww.unm.edu/xrd/xrdbasics.pdf (15 October 2008)

Song, C., Lin, Y., Wang, D., Hu, Z. (2010). Facile synthesis of Ag/ZnO microstructures with enhanced photocatalytic activity. *Materials Letters*. 64, 1595-1597.

Tan, T., Li, Y., Wang, B., Song, X., Li, E., Wang, H., Yan, H. (2008). Two-step preparation of Ag/tetrapod-like ZnO with photocatalytic activity by thermal evaporation and sputtering. *Materials Chemistry and Physics.* 111, 303-308.

Tian, Y., Bing, H., Liao, L., Li, J., Wu, Y., Fu, Q. (2008). Controlled growth surface morphology of ZnO hollow microspheres by growth temperature. *J. Physica E.* 41, 729-733.

Wand, H., Xie, C., Zhang, S., Cai, Z., Yang, Y. (2007). Comparison of dye degradation efficiency using ZnO powders with various size scales. *J. Hazard. Mater.* 141, 645–652.

Wang, J., Fan, X., Tian, K., Zhou, Z., Wang, Y. (2011). Largely improved photocatalytic properties of Ag/tetrapod-like ZnO nanocompounds prepared with different PEG contents. *Applied Surface Science.* 257, 7763-7770.

Wang, Y., Zhang, C., Bi, S., Luo, G. (2010). Preparation of ZnO nanoparticles using the direct precipitation method in a membrane dispersion micro-structured reactor. *Powder Technology.* 202, 130-136.

Wang, S.L., Jai, X., Jiang, P., Fang, H., Tang, W. (2010). Large-scale preparation of chestnut-like ZnO and Zn–ZnO hollow nanostructures by chemical vapor deposition. *J. Alloys and Compounds*. 502, 118-122.

Weller, M.T. 1996. Inorganic Material Chemistry. Oxford Chemistry Primer.Oxford Science Publication. Grate Britain. England.

Whang, T., Hsieh, M., Chen, H. (2011). Visible-light photocatalytic degradation of methylene blue with laser-induced Ag/ZnO nanoparticles. *Applied Suuface Science*. 258, 2796-2801.

Wikimedia Common. (2009). File: Bragg diffraction.png. (online) Available http://commons.wikimedia.org/wiki/File:Bragg_diffraction.png (31 June 2009)

Wikimedia Foundation, Inc. (2008). Zinc oxide (online). Avaliable http://en.wikipedia.org/wiki/zinc-oxide (15 October 2008)

Wikimedia Foundation, Inc. (2008). Scanning electron microscope (online) Available http://en.wikipedia.org/wiki/Scanning_electron_microscope10/11/2008 (15 Octorber 2008)

Wyszecki, G. and Stiles, W.S. (1982). Color Science : Concepts and Methods, Quantitative Data and Formulae (2 nd ed.). Canada, NJ : John Wiley & Sons.

Xie, J., Wu, Q. (2009). One-pot synthesis of ZnO/Ag nanospheres with enhanced photocatalytic activity. *Materials Letters.* 64, 389-392.

Xie, W., Sun, W., Huang, J., Xie, H., Zhao, X. (2010). Surface modification of ZnO with Ag improves its photocatalytic efficiency and photostability. *J. Photochemistry and Photobiology*. 216, 149-155.

Xu, J., Chang, Y., Zhang, Y., Ma, S., Qu, Y., Xu, C. (2008). Effect of silver ions on the structure of ZnO and photocatalytic performance of Ag/ZnO composites. *Applied Surface Science.* 255, 1996-1999.

Yang, Z., Zhang, P., Ding, Y., Jiang, Y., Long, Z., Dai, W. (2010). Facile synthesis of Ag/ZnO heterstructure assisted by UV irradiation:Highly photocatalytic property and enhanced photostability. *Materials Research Bulletin.* 46, 1625-1631.

Yang, L., Dong, S., Sun, J., Feng, J., Wu, Q., Sun, S. (2010). Microwave-assisted preparation, characterization and photocatalytic properties of a dumbbell-shaped ZnO photocatalyst. *J.Hazardous Materials.* 179, 438-443.

Yu, J., Li, C., Liu, S. (2008). Effect of PSS on morphology and optical properties of ZnO. *J.Colloids Interface Sci.* 326, 433–438.

Zeng, J.H., Jin, B.B., Wang, Y.F. (2009). Facet enhanced photocatalytic effect with uniform single-crystalline zinc oxide nanodisks. *Chem. Phys Lett.* 472, 90–95.

Zhang, D., Lui, X., Wang, X. (2011). Growth and photocatalytic activity of ZnO nanosheets stabilized by Ag nanoparticles. *J. Alloys and Compounds.* 509, 4972-4977.

Zhang, S., Li, X., (2003). Preparation of ZnO particles by precipitation transformation method and its inherent formation mechanisms. *Colloids and Surfaces*. 226, 35-44.